Characterization of the Structure and Dynamics of Biomimetic Peptides by Solid-State NMR

Helen E. Ferreira

A dissertation
submitted in partial fulfillment of the
requirements for the degree of

Doctor of Philosophy

University of Washington

2016

Reading Committee:

Gary P. Drobny, Chair

D. Michael Heinekey

Walter James Pfaendtner

Program Authorized to Offer Degree:
Department of Chemistry

University of Washington

Abstract

Characterization of the Structure and Dynamics
of Biomimetic Peptides by Solid-State NMR

Helen E. Ferreira

Chair of the Supervisory Committee:
Professor Gary P. Drobny
Department of Chemistry

Diatoms and sponges use proteins, long chain polyamines, and other biomolecules to assemble silica structures of controlled morphology. Investigated here are biosilicification peptides. Under mild conditions, these peptides produce silica nanoparticles from solutions of silicic acid, whereas harsh methods are currently employed to produce these nanoparticles commercially. Biomimetic precipitation studies have shown that LKα14 (Ac-LKKLLKLLKKLLKL-C), an amphiphilic lysine/leucine repeat peptide with an α-helical secondary structure at polar/apolar interfaces, co-precipitates with silica to form nanospheres. Previous work confirmed the α-helical secondary structure in both the neat and silica-complexed states of the peptide and suggested that the tetrameric bundles of peptide that are known to form in solution persisted in the silica-complexed form. To further investigate the peptide aggregation, deuterium solid-state nuclear magnetic resonance (^{2}H ssNMR) was used to establish how the site-specific leucine side-chain dynamics of LKα14 differ in the neat state, buffered state, and silica-precipitated form. Modeling the ^{2}H ssNMR line shapes using code developed in-house helped probe the mechanisms of peptide pre-aggregation and silica co-precipitation. For the silica samples, the model was verified by fitting three types of ^{2}H NMR data: static quadrupolar echo (QE), magic angle spinning (MAS), and T_1 inversion recovery (T_1IR) spectra. The resulting spectra demonstrate the presence of a tetrameric bundle in the neat state,

which is disrupted with the introduction of buffer and then by silica co-precipitation. This work describes the development of the simulation framework used to model these types of experimental data, strategies for fitting these types of data, and finally, the expansion of the model beyond leucine for use with isoleucine.

TABLE OF CONTENTS

LIST OF FIGURES

LIST OF TABLES

GLOSSARY

EFG: Electric Field Gradient

HETCOR: Heteronuclear Correlation

K: Lysine*, also abbreviated Lys*

L: Leucine*, also abbreviated Leu*

LKα14: Ac-LKKLLKLLKKLLKL-OH, an α-helical 14 residue Leucine/Lysine repeat peptide,

MAS: Magic Angle Spinning

NMR: Nuclear Magnetic Resonance

QCC: Quadrupolar Coupling Constant

R5: a subunit of the silica precipitating peptide, *sil1p* from *Cylindrotheca fusiformis*, with sequence: H-SSKKSGSYSGSKGSKRRIL-OH

REDOR: Rotational-Echo Double Resonance

SFG: Sum-frequency generation

SSNMR: Solid-State NMR

T_1IR: T_1 Inversion Recovery

ACKNOWLEDGMENTS

I would like to thank Professor Gary Drobny for the opportunity to work on so many different aspects of this research, and for his interest in my overall education and career goals, as well as my research projects. I would also like to thank all the members of the Drobny group–past and present–for their encouragement and guidance. I would especially like to thank Dr. Ariel Zane, Dr. Kari Pederson, Dr. Adrienne Roehrich, Dr. Prashant Emani, Erika Buckle, Dr. Steve Davidowski and Rachel Gebhart.

Within the UW Chemistry department, I have had the pleasure of interacting with many groups. I would like to thank the Inorganic Division for giving me my start in graduate school, with a special thanks to Prof. Michael Heinekey, Dr. Michael Coggins and everyone else who encouraged me to keep going when I realized synthetic inorganic chemistry was not for me. I would also like to thank the members of the Amphiphiliphiles for expanding my exposure to the field of biophysics as well as for welcoming me into their group and giving me their immeasurable support.

A huge thank-you to all my friends, near and far, for supporting me when things were hard and for celebrating with me when things were good! I am lucky to know all of you. Kayla Sapp, thank-you for being my Seattle family and my roommate for the last 5 years! Jonathan Litz, you are amazing and I cannot wait to see where life takes us. Even if we don't end up where we expect, I will enjoy the journey with you!

Thank-you Mom and Dad for encouraging my drive and curiosity from the very start. Thank-you to my parents for making me believe I am invincible, and my siblings for reminding me that I am not.

Chapter 1
INTRODUCTION

1.1 Biomineralization

Biomineralization is the formation of inorganic structures in living organisms. Throughout nature there are numerous examples of organisms that are able to generate inorganic structures of controlled shape and size, all at biological pH and temperatures.[1–4] For example, diatoms, a type of unicellular algae, form intricate nanoscale-structured silica shells called frustules.[3,5] The level of structural control exhibited by these organisms under mild conditions would be beneficial to achieve in a lab setting. These sorts of nanostructures have applications in the silica industry, which is worth $2 billion annually, and includes filtrants, desiccants, binding agents, catalysts, and potential drug delivery applications.[6]

One notable silica precipitating protein is *sil1p*, which is used by the diatom *Cylindrotheca fusiformis* to precipitate silica at neutral pH. This system was first studied by Kröger *et al.* who found that a segment of *sil1p* called the Silaffin-1A protein was able to induce silica precipitation.[7–9] A typical procedure for biomimetic silica precipitation is depicted in Figure 1.1. Further study showed another fragment of this protein, the R5 peptide, (H-SSKKSGSYSGSKGSKRRIL-OH), also precipitates silica at neutral pH.[1,3,10–13] Investigation by Lechner *et al.* found that the relative position of the RRIL moiety in R5-derived sequences altered the morphology of the silica precipitates.[14] However, these works leave many questions unanswered. In trying to mimic the biological production methods, it is necessary to gain an understanding of how peptides mediate the silica morphologies. What we want to understand is: how does a peptide's sequence affect its aggregation, and how does this ultimately lead to a particular shape and size of silica particle?

1.2 Synthetic Amphiphilic Peptides

To get a better understanding of the mechanism of peptide mediated silica precipitation, it is advantageous to start with a simple peptide of known secondary structure. Minimizing the size of the peptide limits the number of potential influencing interactions (i.e., sequence length, composition, secondary structure, charge and polarity of side chains) and permits evaluation of how specific interactions change the system. The LK peptides are a series of synthetic amphiphilic peptides, designed by DeGrado and Lear, that satisfy both of these constraints.[15,16] These peptides are composed of different arrangements of hydrophobic leucine (L) and hydrophilic lysine (K), which give a controllable secondary structure at polar/apolar interfaces.

The work presented here focuses on just one of these peptides, LKα14 so named because it is a 14-residue LK peptide (Ac-LKKLLKLLKKLLKL-OH) that has a well characterized α-helical structure. The hydrophilic lysine residues organize to interact with the polar material, while the leucine residues arrange themselves on the opposing surface of the helical peptide to interact with a non-polar region. In solution, this peptide has been shown to cluster to form a tetrameric bundle, with the leucine side chains pointed inwards to form a hydrophobic core, as shown in Figure 1.2.[15] Additional work has been done to characterize the structure and dynamics of LKα14 when adsorbed to surfaces of varying polarities. The interactions of the peptide with polystyrene, functionalized polystyrene, functionalized gold nanoparticles, and silica surfaces have been studied both through NMR methods[17–21] and sum frequency generation (SFG) methods.[22–24] In all of these environments, LKα14 was shown to maintain its α-helical configuration.

Previous work done by Zane *et al.* has shown that LKα14 is able to precipitate silica nanospheres upon addition of silicic acid to the peptide in phosphate buffered saline (PBS).[11,27] An overview of this procedure is shown in Figure 1.1. Analysis of the structural changes of the peptide in its neat versus silica co-precipitated forms was done using ^{13}C NMR techniques, which, together with the use of TALOS-N,[26] allowed for the determination of the

backbone torsion angles. This work confirmed the persistence of the α-helical secondary structure in silica, as shown in Figure 1.3. It was also observed that the residues along the peptide chain did not experience a uniform change in chemical shift. Most interestingly, the leucine side chains involved in the hydrophobic core of the tetrameric bundle (L1, L8, L4, L11 in Figure 1.2) were the residues least perturbed upon silica co-precipitation. This indicates that the tetrameric bundling may persist in silica. To further probe this system and understand the role that this aggregation might have in the overall observed morphology, investigation of the side-chain behavior is required. To that end, deuterium (^{2}H) solid-state NMR (ssNMR) techniques were used to elucidate the dynamics of the leucine side chains at different relative positions in the proposed hydrophobic core and is discussed further in Chapter 3.

1.3 Solid-State NMR

Solid-state ^{2}H NMR techniques have been used extensively as a probe of peptide dynamics in the solid state.[28–32] Deuterium is a non-perturbative probe, and selective deuterium labeling of individual amino acid residues allows for the determination of site-specific dynamics in peptides.[32] These techniques rely on the dominant interaction of the nuclear quadrupolar moment with the electric field gradient and yield line shapes that are sensitive to rates on the order of $10^3 - 10^7\ s^{-1}$; further information about faster rates on the order of $10^7 - 10^{12}\ s^{-1}$ can be obtained through relaxation studies.[32]

1.4 Specific Aims

- I wrote Python-based code for the simulation of ^{2}H QE, MAS, and T_1IR experiments, based on discrete motional models. NMR theory and the development of these programs are discussed in Chapter 2.

- In Chapter 3, ^{2}H ssNMR techniques are used in conjunction with theoretical modeling to probe the side-chain dynamics of specific leucine residues in LKα14, in the neat,

buffered and silica-precipitated forms. The variations in the side-chain mobility in different positions of the helix allows for predictions about the LKα14 aggregation mode in spherical silica nanoparticles.

- Expanding on the basis developed for leucine, in Chapter 4, isoleucine dynamics are quantified in the monomeric form, using 1D ^{2}H and 2D ^{2}H-^{13}C NMR techniques. Though a less symmetric–and therefore more complex–residue, isoleucine dynamics are modeled using a similar approach.

- Chapter 5 presents work done in collaboration with Roy Black and Sarah Keller of the Department of Chemistry at the University of Washington. ^{2}H NMR techniques, including static ^{2}H NMR and ^{13}C$\{^{2}$H$\}$ REDOR, were used to probe the interactions of amino acids with fatty acid vesicles, as part of a study on the origin-of-life.

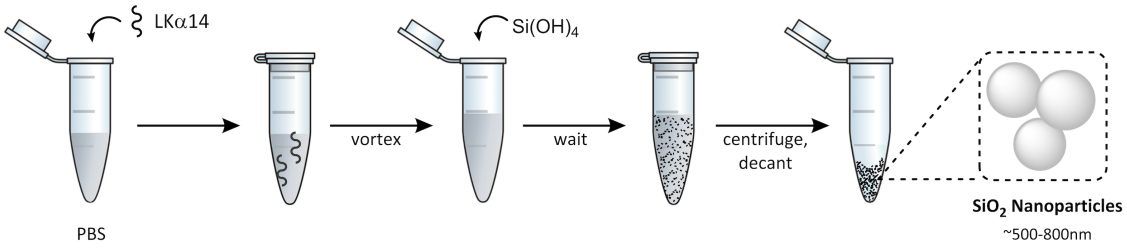

Figure 1.1: Overview of the procedure for silica precipitation mediated by LKα14. LKα14 is a silica-precipitating peptide, PBS is phosphate buffered saline, $Si(OH)_4$ is silicic acid, and SiO_2 is silica.

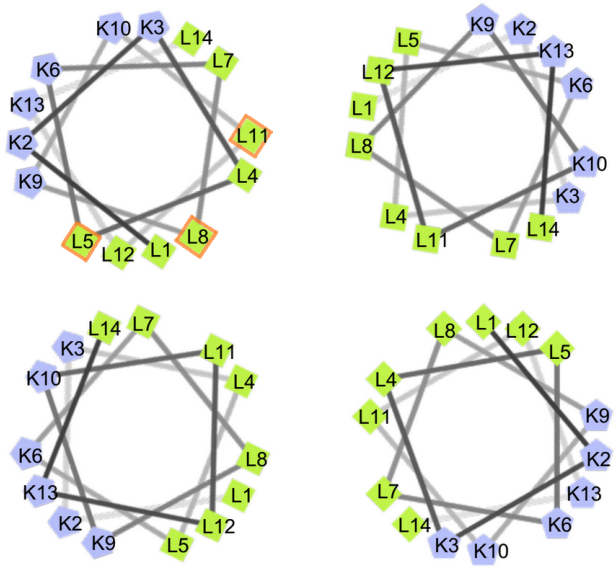

Figure 1.2: Helical wheel view of LKα14 arranged in a tetrameric bundle. Green Squares: Leucine residues facing inwards to form a hydrophobic core; Purple Pentagons: hydrophilic Lys residues exposed to interact with negatively charged SiO_2; Sites highlighted in Orange are the ones selected for further investigation in this work.

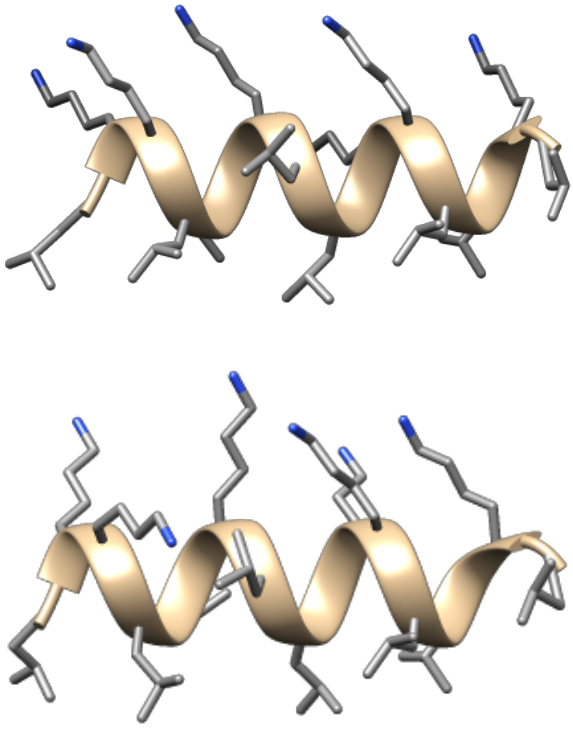

Figure 1.3: Chimera[25] generated structures of LKα14 in the neat [top] and silica precipitated [bottom] states, based on torsion angles obtained from TALOS-N.[11,26]

Chapter 2

NUCLEAR MAGNETIC RESONANCE THEORY

2.1 ^{2}H ssNMR Theory

The dominant interaction of the nuclear electric quadrupole moment with the electric field gradient means that ^{2}H ssNMR techniques are well suited for the characterization of dynamics.[28–32] Solid state deuterium nuclear magnetic resonance techniques have been used extensively as a non-perturbative, selective probe of peptide dynamics in the solid state in a wide variety of conditions.[28–32] Line shapes are sensitive to rates on the order of $10^3 - 10^7 s^{-1}$ while faster motions with rates on the order of $10^7 - 10^{12}\ s^{-1}$ govern T_1 relaxation.[32]

The full Hamiltonian operator describing the NMR spin system contains terms to quantify interactions with both the external magnetic fields and the local interactions, and is given by:[28–31]

$$H = \underbrace{H_z + H_{rf}}_{\text{external}} + \underbrace{H_{CSA} + H_D + H_J + H_Q}_{\text{internal}} \tag{2.1}$$

For deuterium, the magnitudes of the Zeeman (H_z) and quadrupolar (H_Q) interactions are 76 MHz (for an 11.74 T magnet) and 170 kHz (for an sp_3 hybridized C-^{2}H), respectively. These values dwarf the contributions from the chemical shift anisotropy (H_{CSA}), dipolar coupling (H_D) and J-coupling (H_J). The effect of a radio-frequency pulse is described by H_{rf}, this can be dropped from the Hamiltonian as well because one considers the state of the system after the application of any pulses. Therefore, the Hamiltonian can be rewritten simply as:

$$H \approx H_z + H_Q \tag{2.2}$$

The first term represents the Zeeman effect, which is the result of the interaction of the nuclear spin with the static magnetic field (B_0); in practical terms, this is the result of

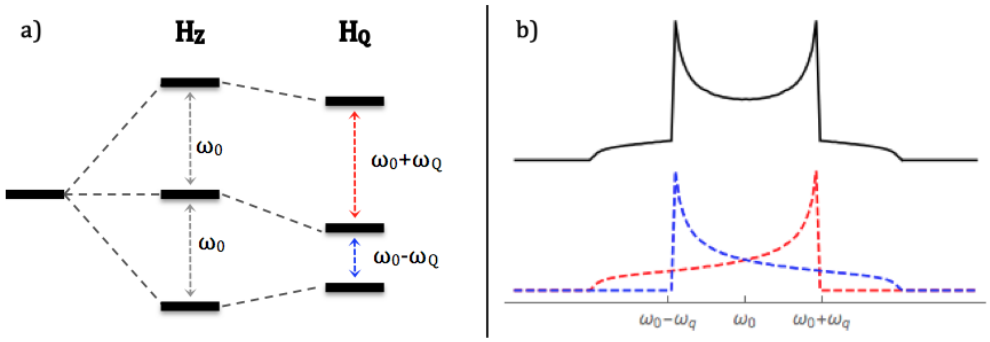

Figure 2.1: a) The splitting of the energy levels upon introduction into a static magnetic field, followed by additional perturbation due to the quadrupolar interaction. (Drawing not-to-scale). b) The static line shape, called the Pake doublet, where ω_Q marks the position of the "horns" corresponding to an EFG orientation of $\theta = \frac{\pi}{2}$.

simply placing a sample into the magnetic field. This interaction leads to the removal of the energetic degeneracy of the spin states; shown in Figure 2.1a. For deuterium this leads to three distinct spin states, corresponding to $I_z = 0, \pm 1$, (where I_z is the component of the spin angular momentum operator in the direction of the applied field, B_0). The Zeeman Hamiltonian, given in Equation 2.3, is dependent on the Larmor precession frequency, ω_0. This in turn depends on the strength of the field (B_0) and the gyromagnetic ratio (γ). The gyromagnetic ratio is a nucleus-dependent value, and is 6.536 MHz T^{-1} for ^{2}H. Hence the interaction has a magnitude of 76.77 MHz in an 11.74 T field. The energy of the splitting is proportional to this frequency, as depicted in Figure 2.1.

$$H_z = -\gamma I_z B_0 = -\omega_0 I_z \tag{2.3}$$

The quadrupolar Hamiltonian describes the interaction of the electric field gradient (EFG) with the nuclear quadrupole moment:

$$H_Q = \left(\frac{eQ}{2h}\right) \mathbf{I} \cdot \mathbf{V} \cdot \mathbf{I} \tag{2.4}$$

where eQ is electric quadrupole moment of the nucleus, I is the nuclear spin vector, and V is

the second rank EFG tensor (in Cartesian coordinates). This tensor can be defined in terms of its cartesian components: V_{xx}, V_{yy}, and V_{zz}. These values are more commonly reported as eq, the principal component of the EFG and η, the asymmetry parameter:

$$eq = V_{zz} \qquad \text{and} \qquad \eta = \frac{V_{xx} - V_{yy}}{V_{zz}} \tag{2.5}$$

The frequency of the perturbation by the quadrupolar interaction is dependent on the relative orientations of the magnetic field and the deuterium EFG tensor, and is therefore a function of both the magnitude and orientation of the quadrupole tensor relative to the magnetic field, which is represented with the Euler angles, $(0, \theta, \phi)$:

$$\omega_Q = \frac{3}{4}\underbrace{\left(\frac{e^2qQ}{\hbar}\right)}_{\text{QCC}}[3\cos^2\theta - 1 + \eta\sin^2\theta\cos 2\phi] \tag{2.6}$$

The simplest NMR line shape generated from this interaction is the axially symmetric ($\eta = 0$) line shape of a "frozen" sample, shown in Figure 2.1b. This line shape is called a Pake doublet, and represents the sum of the spectra resulting from the two possible I_z transitions, $1 \rightarrow 0$ and $0 \rightarrow -1$, shown separately in the bottom panel of Figure 2.1b. The frequencies are derived from the expression for ω_Q, and the intensities are weighted by $\sin\theta$, as a result of the integration over all possible crystallite orientations in a disordered sample, referred to as powder averaging. The interaction is therefore at a maximum when $\theta = \frac{\pi}{2}$, which gives rise to the "horns" of the Pake doublet. The splitting of these horns is proportional to the quadrupolar coupling constant (QCC or C_Q), indicated in Equation 2.6. Note that there is some variation in the literature of the definition of the QCC. Here we follow the convention of QCC = $\frac{e^2qQ}{h}$, and this is the number input into the program. (The factors of $\frac{3}{4}$ and 2π are explicitly applied within the code)

2.2 Overview of ^{2}H ssNMR Experiments

2.2.1 Quadrupolar Echo

Due to the short relaxation time of deuterium in solid samples, it is inadequate to use a single excitation pulse prior to acquisition of the deuterium line shape, as probe ringing

and dead time would interfere with the signal. Instead, a quadrupolar echo pulse sequence, $\left(\frac{\pi}{2}\right)_x - \tau_1 - \left(\frac{\pi}{2}\right)_y - \tau_2 - acqu$, is used, with phase cycling to suppress unwanted coherence pathways.[30,31] The first pulse is an excitation pulse, followed by a refocusing pulse at time τ_1. In principle, this should regenerate the original FID after a second delay of the same length. In practice, τ_2 is shorter to account for the effects of the finite pulse length and the FID must be left-shifted prior to Fourier transformation so that the signal starts at the echo maximum.

2.2.2 Magic Angle Spinning

Magic angle spinning is a technique for improving the signal-to-noise ratio in the deuterium line shape experiments. By spinning the sample rotor at an angle of 54.74° relative to the static magnetic field, the spectrum is split into a set of sharp, evenly spaced sidebands.[33] This is because spinning at the so-called "magic angle" leads to a reduction of the first-order quadrupolar line broadening, due to the angular dependence of this interaction: $\propto (3\cos^2\theta - 1)$. This experiment has the added benefit of increasing the relaxation time, and so does not require a pulse-echo sequence.

2.2.3 T_1 Inversion Recovery

To probe the faster motions in the system, a inversion recovery quadrupolar echo sequence, $\pi - \tau_R - \left(\frac{\pi}{2}\right)_x - \tau_1 - \left(\frac{\pi}{2}\right)_y - \tau_2 - acqu$, is used to determine the longitudinal relaxation time. The time for the spin to relax after the inversion pulse depends on fluctuations in the local magnetic field in the vicinity of the nucleus and therefore is dependent on the molecular motions. By varying the length of the delay after the inversion pulse, this value can be determined experimentally.

2.3 ^{2}H NMR Simulations

In starting to model my data, I was originally using EXPRESS, a publicly available MATLAB program,[34] to simulate the ^{2}H NMR line shape resulting from exchange between discrete

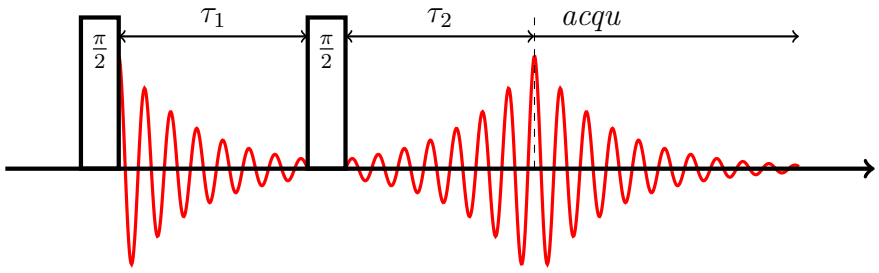

Figure 2.2: Quadrupolar Echo Pulse Program

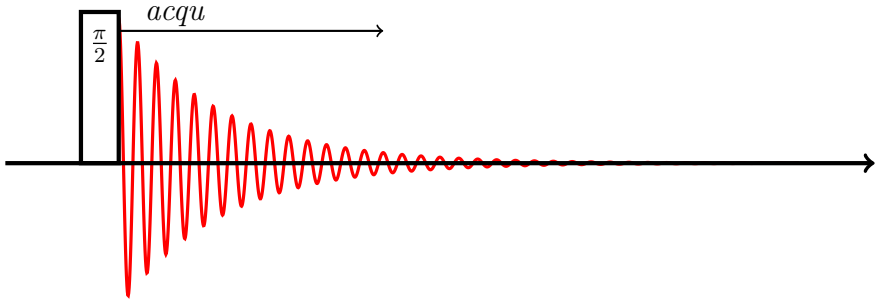

Figure 2.3: Magic Angle Spinning Pulse Program

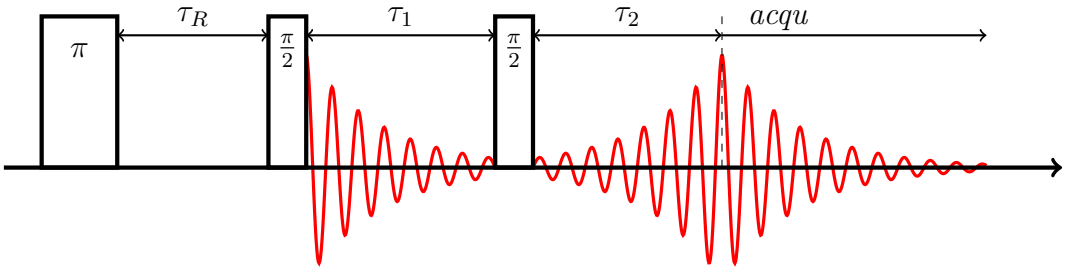

Figure 2.4: T_1IR Pulse Program

conformations. This can be used in conjunction with additional MATLAB scripts to add to its functionality. However, since the initial release of the program, MATLAB had been updated and was slowly deprecating many features used in the GUI for the program. At the same time, I was delving into the theory of the line shape simulations to better understand how to approach my data fitting, and I ultimately decided to write my own code for the simulations in Python. The formalism governing the simulation of dynamics-based line shapes is well reported in the literature;[29,31,35] so will be presented here only in brief. As with EXPRESS, for a model with N discrete sites, the calculation of the spin system's response was done by integration of the Liouville equation.

But why reinvent the wheel?

In terms of the theory implemented, my Python methods do not differ heavily from EXPRESS for the simulation of the quadrupolar echo and T_1IR data. However, it varies dramatically for the MAS simulations, where I implement the numerical integration method published by Duer and Levitt (discussed below).[36] Performance was also dramatically improved allowing for significantly faster calculations (benchmarks below). In addition to being a phenomenal learning exercise for me personally, there are several reasons Python is a preferable platform for this code when compared to MATLAB. (Note: This list is based on my own experiences and is corroborated by a plethora of others.[37,38])

- **Python is free.** Unlike MATLAB, which requires a paid license and additional fees if you require the functionality of additional packages.

- **Python is open-source.** Whereas MATLAB is proprietary and behaves as a black box, Python packages have easily viewable (and editable) source code.

- **Python is open.** "There is a vigorous, healthy public debate on virtually all aspects of Python, with input from any developer or user who wants to participate."[37] This level of interest and involvement also means there is active support for the user.

- **Python is modular.** Not only can you download preexisting modules, Python allows you to define multiple functions in a separate file and import them to your main file. To do that in MATLAB, each function would have to go in your main file, or in it's own individual file, which means similar helper functions cannot be neatly grouped and the number of files needed is large.

- **Python is more readable than MATLAB code.** For example, Python indicates blocks of code–for loops, if-then statements–by the indentation, making it easy to scan through code and follow the logic. On the other hand, MATLAB blocks are finished by an explicit "end" statement. This sort of closure means that the code is lengthier, harder to debug and more daunting to parse through. Ease of comprehension when looking at code – be it your own or a past student's – is crucial for productivity.

- For the transferability of skills, Python is closer to the standard. Like C/C++, Java, Perl, and most other programming languages other than MATLAB, Python conforms to certain de facto standards, including zero-based indexing and the use of square brackets rather than parentheses for indexing. This is an advantage for programmers who must implement published signal processing algorithms, convert code from one language to another, or work across many languages.

2.4 Quadrupolar Echo

As mentioned above, for a model with N discrete sites, the calculation of the spin system's response was done by integration of the Liouville equation:

$$\frac{dm_{\pm}}{dt} = A_{\pm}m_{\pm}(t) = (i\omega_{\pm} + \pi)m_{\pm}(t) \tag{2.7}$$

where $m_{\pm}(t)$ is the transverse magnetization corresponding to the m=-1 to m=0 and the m=0 to m= +1 transitions, $\omega_{\pm}$ is the diagonal matrix with elements $\omega_{\pm,i}$ corresponding to the orientation-dependent frequencies at site i, and π is the NxN exchange matrix that describes the jumps between the sites. Since $\omega_{+,i} = -\omega_{-,i}$, it holds that $m_{+} = m_{-}^{*}$. This

means that the two transitions generate signals in the frequency domain that are mirror images of each other, and therefore only one of these responses is calculated, in this case m_+. Equation 2.7 can be formally integrated to get:

$$m_+(t) = \mathrm{e}^{A_+ t} m_+(0) = L(t) m_+(0) \tag{2.8}$$

For the quadrupolar echo experiment, after the first pulse, during τ_1, the response evolves according to this equation, until the second $\frac{\pi}{2}$ pulse. This second pulse is a refocusing pulse that interchanges m_+ and m_-, resulting in magnetization which is represented as:

$$m_+(\tau_1) = \mathrm{e}^{A^* \tau_1} m_+(0) \tag{2.9}$$

The magnetization after the second delay, τ_2, is then represented as:

$$m_+(\tau_1, \tau_2) = \mathrm{e}^{A\tau_2} \mathrm{e}^{A^* \tau_1} \cdot m(0) \tag{2.10}$$

Finally, the expression for $m_+(t, \tau_1, \tau_2)$ representing the signal evolution after the τ_2 delay, is obtained by combining Equations 2.8 and 2.10:

$$m_+(t, \tau_1, \tau_2) = \mathrm{e}^{A(t+\tau_2)} \mathrm{e}^{A^* \tau_1} \cdot m(0) \tag{2.11}$$

In practice, the matrix exponential is computationally expensive to compute. Note that, in the past, it has been necessary to compute the matrix exponentials in Equation 2.11 by diagonalizing A. However both MATLAB and Python's `scipy` package include a function that eliminate this step, and instead make use of the Padé approximation to permit the direct input of matrix exponential. Additionally, to decrease the number of times this function is called, instead of calculating the matrix exponential for each time point, t, an incremental propagator is calculated and the signal response is calculated iteratively, as follows:[36]

$$m_+(n\Delta t) = \mathrm{e}^{A(\Delta t)} m_+((n-1)\Delta t, \tau_1, \tau_2) \tag{2.12}$$

with

$$m_+(0, \tau_1, \tau_2) = \mathrm{e}^{A\tau_2} \mathrm{e}^{A^* \tau_1} m_+(0) \tag{2.13}$$

To further expedite the speed of calculation, the $e^{A\tau_2}$ term is also dropped from the calculation, as it is computationally more efficient to generate these points with the incremental propagator in Equation 2.12, and then left shift the calculated FID by $\tau_2/\Delta t$ points prior to Fourier transform. The signal at time t is the sum of all the contributions, that is:

$$s_+(t,\tau_1,\tau_2) = \mathbf{1}\cdot m_+(t,\tau_1,\tau_2) = \mathbf{1}\cdot e^{A(t+\tau_2)}e^{A^*\tau_1}\cdot m(0) \tag{2.14}$$

2.4.1 Orientational Dependence

Powder averaging

The solid samples used for static deuterium NMR are, in most cases, powders with crystallites of all possible orientations. The calculated signal in Equation 2.14 is dependent on the orientation of the sample in the magnetic field, that is, the relative orientation of the crystal frame (C) and the lab frame (L), is defined by an angle, Ω_{CL}. The ^{2}H NMR line shape is obtained by integrating the Fourier transform of the time dependent signal, $s(t)$, over all possible sample orientations, $\Omega_{CL} = (0, \theta_{CL}, \phi_{CL})$:

$$I(\omega) = \int_0^{2\pi} \mathrm{d}\phi_{CL} \int_0^{\pi} \mathrm{d}\theta_{CL} \sin\theta_{CL} \quad \mathrm{Re}\left\{ \int_{-\infty}^{\infty} \mathrm{d}t\ s_+(t) e^{-i\omega t} \right\} \tag{2.15}$$

In practice, it is not possible to implement a continuous integral over $s_+(t)$, as in Equation 2.15; instead the signal is simulated as the sum over a set of crystal orientations and recorded at discrete time points. Using the tiling method suggested by Vold *et al.* in the EXPRESS documentation, ZCW (Zaremba-Conroy-Cheng) tiling is employed.[34] See Appendix B.3 for information of the generation of these angles. While executing the sum over these orientations as a loop is less memory intensive, it is faster to construct higher dimensional matrices and parallelize the sum using numpy's `einsum` function (or more recently, the `matmul` function) on stacks of matrices/vectors. See Appendix B.1.1 for implementation in the simulation code.

Calculation of ω_i: Motional frames

Motions are defined as jumps between discrete sites, where for a given site, i, $\Omega_{PC,i}$ is the set of Euler angles that transform the principal component axis system for the EFG tensor, P, into a crystal-fixed axis system, C. (If additional motional frames are desired, intermediate frames (I) are inserted between the principal frame and the crystal-fixed frame. For example, for a model with two motions, Ω_{PI} and Ω_{IC} are defined. These intermediate frames are collapsed into a single set of Euler angles prior to calculating the signal.) Euler angles here follow the Rose or zyz convention, that is for an angle set $\Omega_{PC} = (\alpha, \beta, \gamma)$,

1. Rotate xyz in the principle axis frame counterclockwise around the z axis by α to give $x'y'z'$.

2. Rotate the intermediate $x'y'z'$ counterclockwise around its y' axis by β to give $x''y''z''$.

3. Rotate $x''y''z''$ counterclockwise around its z'' axis by γ to give the final xyz in the crystal frame.

Mathematically, the one frame equivalent sites are generated by the following matrix formalization (see Appendix B.2.2 for implementation):

$$\begin{aligned} R(\alpha,\beta,\gamma) &= \mathrm{e}^{-i\alpha I_z}\mathrm{e}^{-i\beta I_y}\mathrm{e}^{-i\gamma I_z} \\ &= \begin{pmatrix} \cos\alpha & -\sin\alpha & 0 \\ \sin\alpha & \cos\alpha & 0 \\ 0 & 0 & 1 \end{pmatrix} \begin{pmatrix} \cos\beta & 0 & \sin\beta \\ 0 & 1 & 0 \\ -\sin\beta & 0 & \cos\beta \end{pmatrix} \begin{pmatrix} \cos\gamma & -\sin\gamma & 0 \\ \sin\gamma & \cos\gamma & 0 \\ 0 & 0 & 1 \end{pmatrix} \end{aligned} \tag{2.16}$$

As mentioned above in equation 2.7, $A_\pm = \pm i\omega + \pi$ and describes a model with N sites, where ω is a diagonal NxN matrix of the orientation dependent frequencies, ω_i:

$$\omega_i = \frac{3}{4}\frac{e^2qQ}{\hbar}\sum_{a=-2}^{2}\left(D^{(2)}_{0,a}(\Omega_{PC,i}) + \frac{\eta}{\sqrt{6}}\left(D^{(2)}_{2,a}(\Omega_{PC,i}) + D^{(2)}_{-2,a}(\Omega_{PC,i})\right)\right)D^{(2)}_{a,0}(\Omega_{CL}) \tag{2.17}$$

where $D^{(2)}_{m',m}(\alpha,\beta,\gamma)$ are terms of the rank-two Wigner rotation matrices, defined as:

$$D^{(2)}_{m',m}(\alpha,\beta,\gamma) = e^{-im'\alpha}d^{(2)}_{m',m}(\beta)\,e^{-im\gamma} \tag{2.18}$$

where $d^{(2)}_{m',m}(\beta)$ are the elements of Wigner's small d-matrices, listed in Table 2.1.

Assuming that the C-H asymmetry parameter, η, is 0, Equation 2.17 simplifies to:

$$\omega_i = \frac{3}{4}\frac{e^2qQ}{\hbar}\sum_{a=-2}^{2} D^{(2)}_{0,a}(\Omega_{PC,i})D^{(2)}_{a,0}(\Omega_{CL}) \tag{2.19}$$

The elimination of the η term is a limit on the versatility of this program, however the simplification does mean fewer calculations, and therefore faster simulation times. Examples for the definition of these frames are included in Appendix A.2, and the method for calculating these terms is included in Appendix B.2.3.

2.4.2 Calculation of π: Site populations and exchange

The second part of the propagator, π, is a symmetric NxN matrix of the exchange rates between the sites. It is constructed with off diagonal terms, π_{ij}, satisfying microscopic reversibility, i.e. $k_{ij}p_j = k_{ji}p_i$, where k_{ij} is the rate of jumps from site j to site i and p_i is the population of site i. The diagonal terms, π_{ii}, corresponding to the rate of depletion of site i. If it is not the case that all the sites are occupied equally, the matrix A is symmetrized as $A' = P^{-1}AP$, where P is the diagonal matrix such that $P_{ii} = (p_i)^{1/2}$. This can be accomplished by manipulating just the π term of A, since the frequencies lie along the diagonal and remain unchanged. Then the new jump matrix π' is:

$$\pi'_{jk} = \pi'_{kj} = k_{jk}\,(p_k/p_j)^{1/2} = k_{kj}\,(p_j/p_k)^{1/2} \tag{2.20}$$

Note that for simplicity, the user is not asked to construct a full rate matrix where all k_{ij} satisfy microscopic reversibility. Like EXPRESS, to minimize error, the user is asked for a single rate value for each frame of motion, k, such that $k = (k_{kj} + k_{jk})/2$. The jump matrix is then calculated as:

$$\pi'_{jk} = \pi'_{kj} = \frac{2k(p_jp_k)^{1/2}}{p_j + p_k} \tag{2.21}$$

Since P is invertible, the following equivalency holds $e^{A'} = e^{P^{-1}AP} = P^{-1}e^AP$. From this it follows that $e^A = P \cdot P^{-1}e^AP \cdot P^{-1} = Pe^{A'}P^{-1}$. Substituting this into Equation 2.14, where

$\mathbf{m}'=$ \ $\mathbf{m}=$	2	1	0	-1	-2
2	$\left(\frac{1+\cos\beta}{2}\right)^2$	$-\frac{\sin\beta}{2}(1+\cos\beta)$	$\sqrt{\frac{3}{8}}\sin^2\beta$	$-\frac{1}{2}\sin\beta(1-\cos\beta)$	$\left(\frac{1-\cos\beta}{2}\right)^2$
1	$\frac{\sin\beta}{2}(1+\cos\beta)$	$\frac{1}{2}\left(2\cos^2\beta+\cos\beta-1\right)$	$-\sqrt{\frac{3}{8}}\sin 2\beta$	$\frac{1}{2}\left(-2\cos^2\beta+\cos\beta+1\right)$	$-\frac{\sin\beta}{2}(1-\cos\beta)$
0	$\sqrt{\frac{3}{8}}\sin^2\beta$	$\sqrt{\frac{3}{8}}\sin 2\beta$	$\frac{1}{2}\left(3\cos^2\beta-1\right)$	$-\sqrt{\frac{3}{8}}\sin 2\beta$	$\sqrt{\frac{3}{8}}\sin^2\beta$
-1	$\frac{\sin\beta}{2}(1-\cos\beta)$	$\frac{1}{2}\left(-2\cos^2\beta+\cos\beta+1\right)$	$\sqrt{\frac{3}{8}}\sin 2\beta$	$\frac{1}{2}\left(2\cos^2\beta+\cos\beta-1\right)$	$-\frac{\sin\beta}{2}(1+\cos\beta)$
-2	$\left(\frac{1-\cos\beta}{2}\right)^2$	$\frac{\sin\beta}{2}(1-\cos\beta)$	$\sqrt{\frac{3}{8}}\sin^2\beta$	$\frac{\sin\beta}{2}(1+\cos\beta)$	$\left(\frac{1+\cos\beta}{2}\right)^2$

Table 2.1: Elements of Rank-2 Wigner small d-matrices

$m_+(0)$ is the site populations, p_i gives the equation for the signal:

$$s_+(t) = m_+(0)^{1/2} \cdot \mathrm{e}^{A'(t+\tau_2)}\mathrm{e}^{A'^*\tau_1} \cdot m_+(0)^{1/2} \tag{2.22}$$

2.5 MAS Simulations

For MAS spectra, the solution to 2.7 is not so simple as that for the static spectra, given in Equation 2.12. The manual rotation of the sample in the rotor means that it is not simply the case that $L(t) = exp\{i\omega + \pi\}$ because the orientation is now changing with time and so $L(t)$ now depends on $\omega(t)$.[39–42]

2.5.1 Numerical Integration

Following in the footsteps of Duer and Levitt,[36] the method employed here is to numerically integrate, and solve for L(t) over the course of a single rotor period, that is, to generate it on the range $0 < t < \tau_r$. The rotor period, τ_r is divided into n steps, that are sufficiently small so it can be assumed that the orientation is approximately constant over the interval and such that $\Delta t = \frac{\tau_r}{n} = \frac{1}{\nu_r n}$, where ν_r is the rotation frequency. Then, the center of each Δt step is defined as $t_m = (m - \frac{1}{2})\Delta t$ for $m = 0, 1, 2, ...n$. Then L during the rotor period can be calculated as:

$$\begin{aligned} L(m\Delta t) &= \mathrm{e}^{(i\omega(t_m)+\pi)\Delta t} \cdot L((m-1)\Delta t) \\ L(0) &= \mathbf{1} \end{aligned} \tag{2.23}$$

Generally, n = 64 is close to a fair approximation and can be used for preliminary testing of a given model. Full convergence can require smaller steps, with n=128 or 256, consistent with the values reported by Kun Li.[43] Note that while powers of two are not technically required for this method, the further propagation of the signal is coded to be most efficient when the number of fractions and the number of FID points calculated are both powers of two; see Appendix B.1.2 for more information. Once this is calculated for the first rotor period, the rest of the L(t) values are calculated as:

$$L(t + M\tau_r) = L(\tau_r)^M L(t) \tag{2.24}$$

This straightforward method is not the only one used; see below for discussion of the method used in EXPRESS.

Calculation of $\omega_i(t)$ and tiling

While the static spectra only require two-angle tiling for the integration, the transformation from the MAS frame to the laboratory frame requires a full three-angle tiling set be used. This is more easily seen looking at the calculation of the orientation dependent site frequencies:

$$\omega_i(t) = \frac{3}{4}\frac{e^2qQ}{\hbar}\sum_{a,b=-2}^{2} D^{(2)}_{0,a}(\Omega_{PC,i})D^{(2)}_{a,b}(\Omega_{CL})D^{(2)}_{b,0}(\Omega_{LM}(t)) \tag{2.25}$$

where $\Omega_{LM}(t) = \Omega_{LM}(m\Delta t) = (\frac{2\pi}{n}m\Delta t, \theta_{magic}, 0)$. The tiles used here are the optimized ZCW3 sets, and are not calculated like the two-angle sets used for the quadrupolar echo experiments.[44–46] They are stored for a few fixed values and imported as needed.[47] See Appendix B.3 for more information.

2.5.2 Floquet Theory Comparison

Another method commonly used for simulating these line shapes exploits the periodicity of these orientations to construct a new time-independent operator, using a Floquet expansion.[34,36] This can then be used as in Equation 2.12. In EXPRESS, the user is asked the "number of sideband pairs" they want to simulate in their spectrum, a somewhat misleading label, as the documentation recommends that the user select a number 2-3 times the number desired. Looking into the algorithm used to construct this operator, one finds that the simulation generates a square matrix with a length of $(2 \times n_{side} + 1) \times n_{sites}$, compared to the propagator for the static simulations which is a square matrix with dimensions of $n_{sites} \times n_{sites}$. In the documentation for EXPRESS, it is noted that the majority of their computational time is spent, not on the matrix exponential, but on the recursive FID propagation by matrix multiplication, and they use this to, in part, justify their method. I would

like to note that the numerical integration method presented above uses smaller matrices and therefore dramatically decreases the amount of time required for the calculations.

2.6 T_1IR Simulations

The addition of the π pulse at a variable delay, τ_r, before the quadrupolar echo sequence allows for the determination of the spin lattice relaxation rate, T_1. For a given crystal orientation, the signal can be calculated as in Equation 2.22, with just the addition of a constant factor reflecting the extent of relaxation at time τ_r. Most simply this is given as:

$$m(\tau_r) = m(0) \cdot \left(1 - 2e^{-\tau_r/T_1}\right) \tag{2.26}$$

The relaxation time, T_1, depends on the strength of the magnetic field, ω_0 and the crystal orientation. It can be calculated from the spectral densities, J_m, as follows:[28,34,35]

$$\frac{1}{T_1} = \frac{3}{16}\left(\frac{e^2qQ}{\hbar}\right)\left(J_1(\omega_0, \Omega_{CL}) + 4J_2(\omega_0, \Omega_{CL})\right) \tag{2.27}$$

The form of the spectral densities has been derived previously in the literature (most useful to this author was the presentation by Wittebort, *et al.*[35]). Note that the version here differs in the ordering of the Wigner rotations, for example, the rotation Ω_{PC} is used in place of Ω_{CP}, as this accounts for the flipped order of the subscripts of the Wigner-D rotation matrices. Additionally, the sum is given in terms of the full Wigner-D rotation matrix, whereas Wittebort simplifies it include only the Wigner small-d elements and a cosine term.

$$\begin{aligned} J_m(\omega, \Omega_{CL}) = -2 &\sum_{a,a'=-2}^{2} D^{(2)*}_{am}(\Omega_{CL}) D^{(2)}_{a'm}(\Omega_{CL}) \\ &\times \sum_{n,l,j=1}^{N} X^{(0)}_l X^{(n)}_l X^{(0)}_j X^{(n)}_j D^{(2)*}_{0a}(\Omega_{PC,l}) D^{(2)}_{0a'}(\Omega_{PC,j}) \frac{\lambda_n}{\lambda_n^2 + m^2\omega_0^2} \end{aligned} \tag{2.28}$$

The $X^{(n)}$ and λ_n terms refer to the corresponding eigenvectors and eigenvalues of the jump matrix, π, calculated as in Equation 2.21. Note that $X^{(0)}$ is taken to be the initial magnetization vector with terms equal to $p_i^{1/2}$.

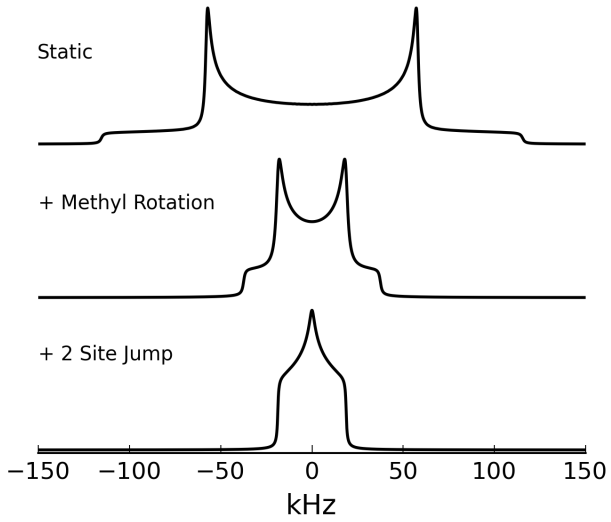

Figure 2.5: QE Examples: Sample simulated line shapes for basic motions.

2.7 Benchmarking

2.7.1 Static QE

In Figure 2.5, some sample quadrupolar echo line shapes are shown for basic models of motion. Note the three-fold narrowing of the line shape with the addition of the methyl rotation. Addition of a two-site jump, where the two sites are related by tetrahedral geometry, results in the effective asymmetry parameter as shown in the bottom spectrum. Comparing the speeds of the simulation between the MATLAB-based EXPRESS and the Python program used here, a number of sizes of simulations were considered, as was done in the original documentation.[34] Table 2.2 lists these simulation parameters as well as the simulation times in both programs. The Python program is universally faster, though it is close for large numbers of FID points and sites. However, small numbers of sites and high numbers of tiles take half the time, which is important for convergence of the line shape. Vold *et al.*[34] note that the quadrupolar echo line shape simulations may only require a small number of FID points to converge (i.e. 256), but can require integration over a large number of tiles.

Sites[a]	Points	Tiles	Time[b]	Time[c]
3×4	512	233	1.1	0.36
3×7	512	233	1.5	0.57
3×7	512	1597	9.2	4.0
10×3	256	987	5.7	3.4
20×3	256	987	13.8	11.6
20×3	1024	987	20	19.3
2×2	256	46368	96	46

[a]Numbers refer to the number of sites in each motional frame, therefore the total number of sites is the product of these numbers.

[b]Time in EXPRESS, using a 2.5 GHz MacBook Pro running MATLAB release r2015b under Mac OS X 10.11.1.

[c]Time in Python, using a 2.5 GHz MacBook Pro running Python 3.4.3 under Mac OS X 10.11.1 (See Appendix A.1.2 for full package version information)

Table 2.2: Benchmarking Times for QE simulations

2.7.2 MAS

As noted above, the Floquet method requires a propagator matrix of size $(2n_{side}+1)n_{sites} \times (2n_{side}+1)n_{sites}$, while the numerical integration method requires a set of $n_{rotfrac}$ propagators with size $n_{sites} \times n_{sites}$. Take as an example a 6-site model, with a moderate spinning speed that results in 10 side band pairs. The Floquet method would require 2-3 times that number of sideband pairs to simulate it fully: say 25 sideband pairs, then the matrix has size: $((2n_{side}+1)n_{sites})^2 = ((2(25)+1)(6))^2 = 306 \times 306$. Assuming the numerical integration method converges with $n_{rotfrac} = 256$, then the method requires $n_{rotfrac} \times n_{site}^2 = 256 \times (6 \times 6)$. Note that while this does mean that the numerical integration method requires 256 times as many matrix exponentials to be performed, the size of those matrices is dramatically smaller. Additionally, after the calculation for the first rotor period, the propagation of the signal using the dot product requires only the set of 6×6 matrices generated, whereas the Floquet method requires multiplication by a matrix over 50 times as large.

2.7.3 T_1IR

As demonstrated in Table 2.3, the Python-based program runs much faster than the MATLAB version. Most notably, the Python version makes better use of array broadcasting techniques and eliminates the extensive use of for-loops in the calculation of the relaxation time. The for-loop method is more immediately understandable to a reader, and corresponds more clearly to the summation notation used by Wittebort *et al.*, however it is far less computationally efficient. To show that the method does not alter the accuracy of the algorithm, Figure 2.6 was generated using the sample parameters as presented by Vold *et al.*, and is presented for comparison with their results, see reference.[34]

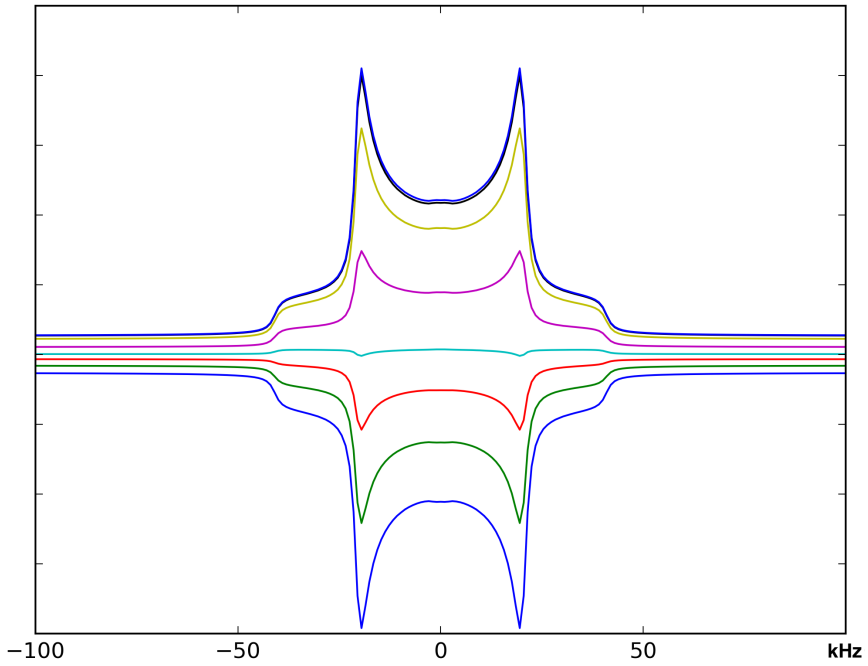

Figure 2.6: T_1IR Example: For comparison with the figure in the Express documentation. Modeling dimethylsulfone using the parameters given therein,[34] also see sample input file in AppendixA.2.3. τ = 1, 10, 20, 30, 50, 100, 200, 400ms.

Sites[a]	Points	Tiles	Delays	Time[b]	Time[c]
3×4	512	233	8τ's	5.79	1.86

[a]Numbers refer to the number of sites in each motional frame, therefore the total number of sites is the product of these numbers.

[b]Time in EXPRESS, using a 2.5 GHz MacBook Pro running MATLAB release r2015b under Mac OS X 10.11.1.

[c]Time in Python, using a 2.5 GHz MacBook Pro running Python 3.4.3 under Mac OS X 10.11.1 (See Appendix A.1.2 for full package version information)

Table 2.3: Benchmarking Times for a T_1IR Simulation.

Chapter 3

BIOSILICIFICATION AND THE LKα14 PEPTIDE: MODELING LEUCINE SIDE CHAIN DYNAMICS

As discussed in Chapter 2, ^{2}H NMR can be used to determine information about dynamics. Here this method is applied to evaluate the packing of LKα14 in silica, as well as in the neat and buffered states for comparison. The peptide is thought to form a tetrameric bundle (see Figure 1.2).

3.1 Qualitative Analysis of Leucine Dynamics

Leucine methyl group dynamics are very sensitive to the their environment. In a protein hydrophobic core, motion is limited because the non-polar side chains are tightly packed and more shielded from changes in the outside environment. Closer to the polar interface, motion is increased because the steric hindrance is decreased. Smith *et al.* has used this type of analysis to determine relative mobility of leucine residues along a peptide to probe the relative packing orientations of helical peptides.[48–50] Similarly, Long *et al.* applied this analysis to determine the orientation of KL_4, a lung surfactant peptide, in a phospholipid bilayer.[51]

In the absence of motion, the spectrum will be the axially symmetric line shape of a "frozen" sample, called the Pake doublet, shown in Figure 2.5a. ^{2}H line shapes can be interpreted qualitatively in terms of their deviation from this Pake doublet, which is indicative of molecular motions with a correlation time of $10^{-3} - 10^{-7}$ seconds. Rapid, axially symmetric motions, such as methyl group rotation, result in the narrowing of the spectrum, and therefore decreased splitting between the horns and can be treated as effective decrease in the QCC for modeling purposes, as shown in Figure 2.5b. Asymmetric motions, such as

rotameric exchange or diffusion of the methyl group along an arc, will result in an increased central intensity and a corresponding decrease of the intensity of the horns, as shown in Figure 2.5c.

3.2 Quantitative Motional Models for ^{2}H NMR Simulations

The most important part, and sometimes the most difficult part, of fitting the spectral data is choosing a physical model to parametrize. As discussed in Chapter 2, these models are based on jump motions between defined sites. Complexity is added to these phenomenological models by adding additional frames of motion. This system of model development complicates comparing systems, but it gives a model with a physical meaning that is more intuitively comprehended. The lack of an analogous conceptualization is why a "model-free" method such as the microscopic-order-macroscopic-disorder (MOMD) approach developed by Meirovitch *et al.* are avoided in this work.[52,53]

3.2.1 Methyl Rotation

As mentioned in the qualitative analysis section, the rapid rotation of the methyl CD_3 around the C_γ-C_δ bond results in an overall narrowing of the line shape. For the purposes of QE and MAS simulations, this motion means the methyl group deuterons can be approximated as a single effective axially symmetric quadrupolar tensor along the C_γ-C_δ bond, with a decreased QCC, which decreases the number of sites needed to model the spectra (and therefore the computational time needed). For T_1IR simulations, this simplification is not valid since T_1 depends on faster rates, and the correlation time of these rapid motions must explicitly be incorporated. This can be explicitly modeled as a three site jump around a C_{3v} axis defined by the C_γ-C_δ bond.

3.2.2 Rotameric Jumps

The leucine side chain is able to take on 9 different rotameric conformations, which are the result of three possible torsion angles around each the C_α−C_β (χ_1) and C_β−C_γ (χ_2)

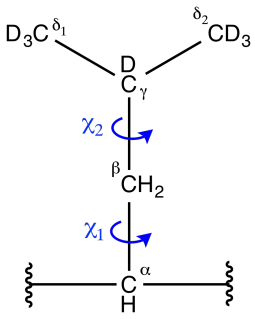

Figure 3.1: Linearized structure of thed_7 leucine side chain. Torsion angles and carbon numbering are indicated for reference.

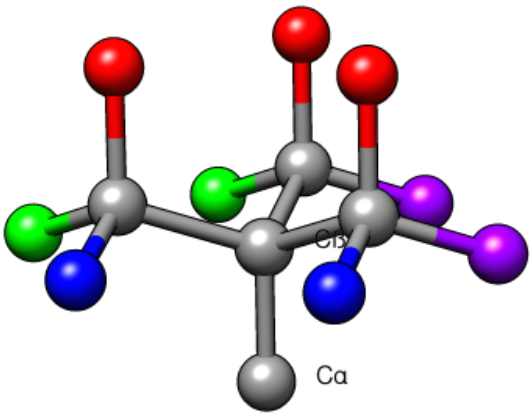

Figure 3.2: Leucine Rotameric Orientations. All possible methyl group orientations relative to the $C_\alpha - C_\beta$ bond for rotameric jumps; colored to indicate magnetic equivalence.

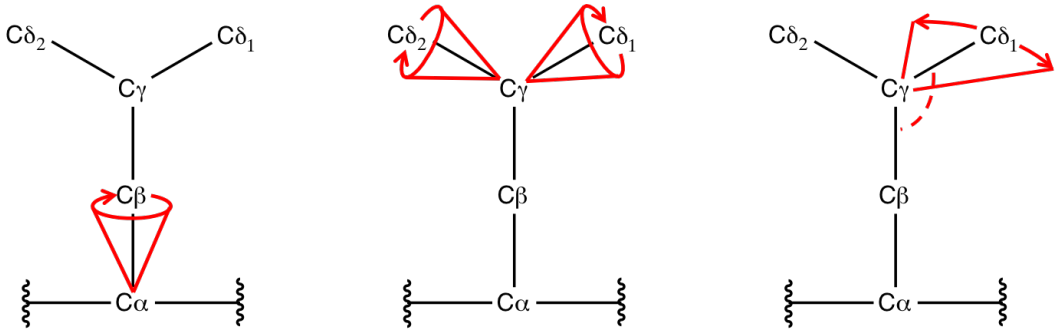

Figure 3.3: Examples of models of librational motions from the literature: (from left to right) Cone motion around the $C_\alpha - C_\beta$, adapted from Breen *et al.*;[18] Cone motion around the $C_\gamma - C_\delta$, adapted from Breen *et al.*;[19,21] Methyl group motion along a variable arc length, with a fixed $C_\beta - C_\gamma - C_\delta$ angle of 70.5°, adapted from Vugmeyster *et al.*[56–61]

bonds, as shown in Figure 3.1. These possible torsion angles are labelled *gauche*(-), *trans* and *gauche*(+) and corresponding to 60°, 180°, and 300°, respectively. Assuming ideal bond angles, these nine rotamers can be reduced to four magnetically distinct sites, corresponding to the vertices of a tetrahedron, as shown in Figure 3.2. It is also assumed that the two methyl groups behave in an equivalent matter, and so it is sufficient to model the motions of just one of these groups. Early work by Batchelder *et al.* characterizing dynamics in collagen, models the leucine side chain through a simple rotameric jump between the two dominant conformations, *gauche*(+)*trans* and *trans gauche*(-).[54,55] To model phospholamban dynamics in lipid bilayers, Lorigan *et al.*, chose to model leucine dynamics by tilting the methyl groups at 75° and jumping between two sites separated by 109.5°. Work by Vugmeyster *et al.* includes a rotameric jump, which is modeled by 4 sites, corresponding to the magnetically non-equivalent positions, with unequal populations w:1:1:1.[56–61]

3.2.3 Librational Modes

Other models include not only the rotameric jumps, but also an additional perturbation due to bond librations or backbone movement.[62–65] For example, in work by Vugmeyster *et al.* in addition to the rotameric jump the $C_\gamma - C_\delta$ bond is assumed to move along a variable-length arc, shown in the right panel of Figure 3.3.[56–61] Previous work characterizing LKα14 dynamics, by Breen *et al.*, employed a two-site rotameric jump with additional librational motion modeled as nearest neighbor jumps of a bond along a cone–around either the $C_\alpha - C_\beta$[18] or $C_\gamma - C_\delta$ bond,[19,21] as depicted in Figure 3.3.

3.3 Automation of Fitting

Defining the motional model with multiple sites and jump rates leads to a daunting number of parameters to optimize. There are several approaches that can be taken. In studying the chicken villin headpiece, Vugmeyster *et al.* generated libraries of spectra with varied parameters, an approach made possible by the simplification of the problem to just 2-4 adjustable parameters. The line shapes were fit checking the quality of the fit for every spectrum in the library.

With an increased number of variables, this is not a viable option, since the number of possible parameter sets scales exponentially. Instead it is desirable to introduce an automated search algorithm into the fitting program for global optimization of the paramters. Aliev and Harris[66] implemented simulated annealing to fit the QE spectra of thiourea-d_4. A similar approach has been used by Li *et al.* to fit ^{2}H MAS line shapes and model the dynamics of the phenylalanine side chain.[67] There a simulated annealing algorithm was implemented to minimize the difference in the intensities of the spinning sidebands in the spectra. I tried using the simple downhill search, simulated annealing and threshold acceptance algorithms. I prefer the threshold acceptance algorithm, but have included an overview of each of these methods.

3.3.1 Simple Algorithm

The most straightforward random search method is to simply take random steps and accept these steps if they improve the fit. The user defines a set of starting parameters, a step size, and a goodness of fit metric. Based on the step size, a random new set of parameters is generated. If this set of new parameters results in a spectrum that is a "better fit," this parameter set is saved as the new best fit, otherwise the best fit is unchanged. This process continues iteratively until an end condition is reached, generally either a total number of steps taken, or a number of steps without improvement, which implies that the state is optimized. This method invariably leads to a local minimum, but not necessarily a global minimum.

3.3.2 Simulated Annealing

To overcome situations where the step size is too small to escape a local minimum, a simulated annealing method was employed by Aliev and Harris.[66] This method is similar to the simple method described above, however it does not reject all steps that do not improve the fit. If a parameter set is found to be the best fit seen, it is stored as the best fit. However, in addition to accepting steps that improve the fit, the algorithm uses to Metropolis-Hastings method and explores the parameter space by accepting steps that do not make the fit significantly worse with some small probability $e^{\Delta - E/T}$, where ΔE is the change in the energy or goodness-of-fit parameter compared to the previous parameter set evaluated and T is a temperature parameter.[68,69] The temperature parameter, T, is set by the user and is decreased over the course of the optimization according to a defined "cooling schedule", hence the term "annealing". This means that the algorithm is more likely to accept steps that do not improve the fit early in the optimization to better explore the parameter space, and less so as the simulation is closer to converging.

3.3.3 Threshold Acceptance

The algorithm employed in this work is the threshold accepting algorithm.[70,71] This method is very similar to the simulated annealing method, but instead of only accepting worse fits with a small probability, every fit that is only a little bit worse (under a certain threshold) is accepted. The elimination of the random acceptance criterion guarantees a more thorough traversal of the parameter space, and has been found to be a superior method. Analogous to the "cooling schedule" employed in the simulated annealing method, the threshold value is decreased if the quality of the fit has not been improved after some number of iterations. It is also possible to decrease the step size to allow for a more localized search as the optimization nears convergence.

3.3.4 Setting up an Optimization

Goodness-of-Fit

The most common goodness of fit method is a simple residual:

$$R^2 = \frac{1}{N}\sum_{i=1}^{N}\left(I_i^{exp} - I_i^{sim}\right)^2 \tag{3.1}$$

While often used, there are complications. Special concerns with automating the fitting of these spectra include the non-discrete nature of these spectra. For the fitting of the MAS spectra discussed previously the spectra were treated as a set of discrete intensities corresponding to each sideband height. This simplified the fitting function by removing the complications presented by the hard-to-fit sideband widths.

With static line shapes, one is faced with the complicating factors of the mild asymmetry present in the experimental data and the complication of residual water contributing an isotropic peak, which should not be fit by the model, but leads to a significant distortion when using a fitting metric based solely on spectral intensity. Vugmeyster *et al.* used alternative indicators of goodness-of-fit: possibilities include horn splitting, width of the line shape at half height, and width of the spectrum at the shoulders.[56,57]

In work presented here the goodness of fit metric used was a modified R^2. It was modified to include a sub-optimization (performed using a built in scipy routine) to account for several factors, referred to here as x. Firstly, offsets in the height or scaling were accounted for by optimizing a vertical offset, x[1], and scaling factor, x[0], rather than attempting to perfectly optimize the baseline and normalize based on peak height alone. Second, the spectra include contributions from the H^{γ} in addition to the methyl groups. This contribution is not necessarily stoichiometric due to attenuation because of the longer relaxation time. Rather than including this as a parameter in the search, the contribution was determined after the fact, by scaling the contribution to the spectrum of H^{γ} by a factor, x[2]. Finally, the water peak was modeled as a Lorentzian line shape ($y = \frac{1}{1+x^2}$) with variable width (x[4] = 1-4 Hz) and variable contribution scaled by x[3], to account for the central distortions. Overall this lead to a final spectrum as follows:

$$S = x[0]\,(S_{methyl} + x[2] * S_{\gamma}) + x[1] + x[3] * S_{water} \tag{3.2}$$

Threshold, Step Size, and Starting Point

These parameters require some testing to optimize. The threshold needs to be large enough that the optimization adequately explores the parameter space, but large enough to prevent all steps from being accepted. One back-up measure to prevent a search from just endlessly climbing up hill is to set a maximum energy value that the state can have. However, it is usually better to adjust the threshold and step size relative to each other.

Step size should similarly be big enough to adequately explore the space, without being so large that it is too random. An even bigger concern is unbalanced step size, that is, one parameter exploring the space insufficiently compared to the rest of the set. This leads to the local minima one wants to avoid. The easiest example is allowing the QCC to change a lot compared to the jump rate(s) and population(s). The search algorithm can get stuck in a local minimum where the QCC was adjusted to fit the spectral width (especially since the steep slope has a big effect on the R^2) but doesn't fit the overall line shape well, when a

larger QCC and increased motion may be better.

Other parameters than can be changed are the number of steps to take without improvement before decreasing the threshold (and step size) and how much to decrease them by. More steps and slower decrease of step size and threshold, guarantees a better exploration of the parameter space, but takes longer. In cases with a large number of parameters it is beneficial to try a variety of settings for all of these parameters discussed. Lastly, it is important to start with a model that is somewhat close to fitting the data. While this is not necessary, it does help significantly.

Multiple Spectral Types

Finally, the absolute fit of any one type of data is not the best indicator of the accuracy of a model. The use of different, overlapping methods constrains the model. The best fit of the QE data will not necessarily be the best fit of the MAS and T_1IR data because each method is sensitive to slightly different rates. This is demonstrated later.

3.4 Methods

3.4.1 LK Synthesis

Labelled leucine was singly incorporated into peptide samples, i.e., L8 indicates L-leucine-(*isopropyl*-d_7) was incorporated at position 8. One of the peptides, L11, was synthesized by a previous group member, Dr. Nicholas Breen, on a Rainin PS3 instrument, as previously reported.[18] Additional L11 sample was required and synthesized using a CEM Liberty Blue Automated Microwave Peptide Synthesizer using standard FMOC chemistry, followed by acetylation of the N terminus. After cleavage, the purity was determined by mass spectrometry. No further purification was required.

In addition to peptides that were synthesized in-house, two peptides were purchased from Anaspec (Fremont, CA) with d_7-^{2}H labels at the L5 and L8 sites, respectively.

3.4.2 Silica Precipitation

As previously reported,[11] silica samples for NMR studies were prepared by first dissolving peptide (∼25mg) in 1 x PBS (5 mL) to give a 3 mM solution. While the peptide dissolved, 1M $Si(OH)_4$ (silicic acid) was prepared by dissolving 0.15 mL TMOS (tetramethyl orthosilicate) in 0.85 mL 1 mM HCl. 1M $Si(OH)_4$ (0.5 mL) was added to the buffered peptide solution; the mixture was vortexed and allowed to incubate for five minutes at room temperature. After silica precipitation, the sample was centrifuged, washed (3 x 5 mL DI water), and dried en vacuo.

3.4.3 NMR Sample Preparation

The neat peptide was lyophilized from a solution of 3 mM LKα14 in deionized water. For hydrated samples, this sample was then hydrated to ∼40% by mass, to reinstate native dynamics.[59,72] This was achieved by diffusion of deuterium-depleted water into the sample rotor. The PBS-peptide samples were prepared analogously to the neat samples, but from PBS buffer instead of water. Silica-peptide co-precipitate was prepared as described above, and analyzed without further treatment.

3.5 NMR Experimental Methods

3.5.1 ^2H Quadrupolar Echo Lineshapes

All static quadrupolar echo experiments were performed at 11.74T field (76.77 MHz deuterium Larmor frequency) using a home-built, single-channel, static deuterium probe with a Bruker Avance III spectrometer and a $\frac{\pi}{2}$ pulse time of 2.9 μs. Quadrupolar echo experiments used eight-step phase cycling, with an echo delay of 40 μs, and a recycle delay of 0.4s. Line shapes were processed by left-shifting to the echo maximum prior to Fourier transform, followed by 1 kHz line broadening and phase correction.

3.5.2 ^2H T_1 Inversion Recovery

T_{1Z} measurements were also acquired at 11.74T, using an inversion recovery pulse sequence with quadrupolar echo detection. Six variable delays were used [500ms, 100ms, 50ms, 25ms, 10ms, 1ms], and 160k scans were acquired for each time point, and processing was performed as for the line shapes.

3.5.3 ^2H Magic Angle Spinning

MAS line shapes were acquired with the same magnetic field, but with a Bruker TriGamma probe. These experiments employed a single ^{2}H $\frac{\pi}{2}$ pulse width of 3.4 μs and were performed with spinning speeds of 4 kHz. 60k-200k scans were collected, depending on the spectrum, with a 1s relaxation delay between scans. After left-shifting to the peak of the first echo, FIDs were Fourier transformed and phase-corrected without further processing.

3.6 Results

3.6.1 Qualitative ^2H Line Shape Analysis

As shown in Figure 3.4, line shapes for L5, L8 and L11 were collected in the neat, buffered and silica-precipitated states, with hydration introduced to show the change in dynamics based on water interactions. As expected, for the neat and buffered samples, the degree of mobility of the leucine side chains is related to the degree of interaction with the hydrophobic core of the tetrameric bundle (shown in Figure 1.2). Hydration exaggerates these differences, but even unhydrated, it is evident that L8 exhibits the spectrum most typical of a rigid side chain. The L11 side chain is also fairly static, indicating a degree of interaction with the hydrophobic core. However, upon hydration, the motions appear to increase more so than L8, in keeping with the proposed degree of interaction. Most striking of all, the L5 residue appears to be highly mobile in all the environments, with a dramatic isotropic peak in the hydrated peptide. The introduction of buffer appears to order the system more; L5 displays horns when unhydrated and L11 retains the Pake doublet horns even upon hydration.

However, the most curious result seems to be for the peptide in silica. While the rest of the spectra are consistent with similar research on model peptide helix packing,[48–50] these more closely resemble line shapes resulting from a hydrophobic core environment. There is an increase of the central spectral intensity relative to the otherwise overly static line shapes obtained for L8, which indicates an increased in motion for L8. The spectra for all three sites are near identical, indicating similar dynamic processes are occurring. The silica samples were further probed with MAS, as well as through T_{1Z} measurements (48.2±2.1 ms, 47.4±2.1 ms, 47.1±2.2 ms, for L5, L8 and L11, respectively) and yielded remarkably similar results for all three sites.

In silica, it is not simply the case that all of the side chains are tightly packed, as the L8 spectrum represents an increased mobility over the neat spectrum. The lack of apparent deviation in the sites would seem to indicate that the differentiating structure of the hydrophobic core is no longer present. However, the chemical shift data previously reported by Zane *et al.* indicates that the average structural position of the L8 side chain is minimally perturbed in silica, indicating that it remains in a hydrophobic environment. This new dynamics data shows a deviation in the side chain motion of L8, which points to a rearrangement of the tetrameric bundle. Potential explanations are a repacking of all the leucine side chains so they are more shielded from the polar silica, or perhaps aggregation to pentameric bundles, instead of tetramers. These models can be probed by getting a quantitative model of the potential motions that could lead to the observed spectra.

3.6.2 Quantitative ^2H Line Shape Analysis

As mentioned, the first step in fitting the data is choosing a model. This is not always a straightforward process, and to illustrate this, a comparison of the final fit with two alternate fits of the silica data is presented later in this chapter. The model that was chosen to fit the data that used by Vugmeyster *et al.*.[56–61] Rotameric exchange was modeled using 4 sites, corresponding to the magnetically non-equivalent positions, with unequal populations w:1:1:1. In addition to the simplified rotameric model, librational motion was incorporated

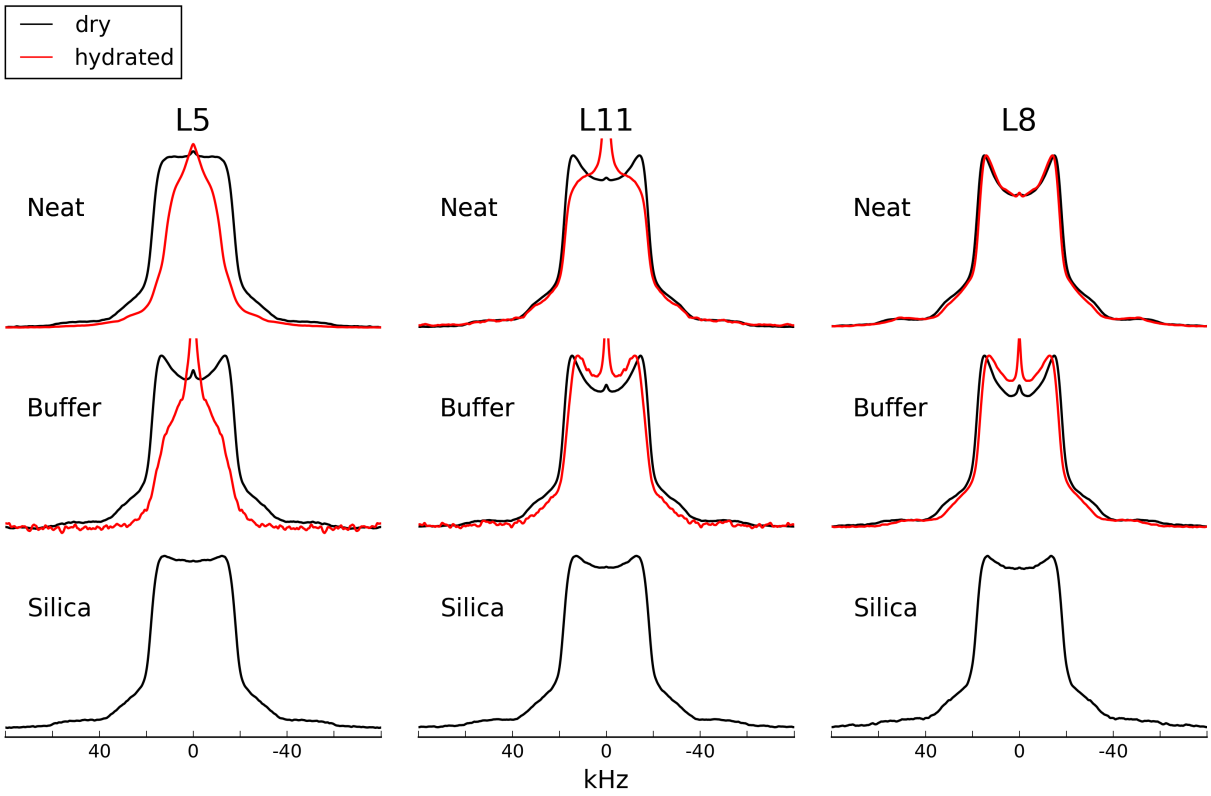

Figure 3.4: Static quadrupolar echo spectra were collected for L5, L8 and L11 under a series of conditions: lyophilized from water, then hydrated; lyophilized from PBS, then hydrated; and co-precipitated with silica. Also included are the MAS spectra obtained for the peptide co-precipitated with silica.

as diffusion of the $C_\gamma - C_\delta$ bond along a restricted arc. The arc is modeled with sites separated by 5° with jumps between nearest neighbor sites only. Also in agreement with their findings, the population distribution along the arc was best modeled with a flat potential (i.e. equal probability of being at any given site along the arc).

The QCC was set to 51.5 kHz, and the parameters that were allowed to vary were: the diffusion rate (k_{arc}), the rotameric exchange rate (k_{rot}), the population ratio (w:1:1:1) and the arc length. Preliminary fits were established by eye, and then automated optimization was

Sample		Site	k_{arc} ($/10^7 s^{-1}$)	k_{rot} ($/10^4 s^{-1}$)	Arc Length	Populations w:1:1:1
Neat	Dry	L5	7.5	6.5	55°	10.6
		L11	1.0	6.1	50°	12.3
		L8	0.8	5.7	50°	18.0
	Hydrated	L5	40.4	100.0	25°	1.6
		L11	10.1	10.2	50°	14.2
		L8	1.0	3.8	60°	8.5
Buffer	Dry	L5	1.0	6.2	55°	11.4
		L11	0.7	8.0	50°	18.0
		L8	0.6	6.5	50°	18.0
	Hydrated	L5	15.3	66.5	55°	4.1
		L11	1.1	8.1	70°	9.3
		L8	1.3	4.6	65°	7.9
Silica		L5	1.3	26.2	35°	12.1
		L11	1.4	26.8	35°	14.3
		L8	1.5	29.8	30°	14.8

Table 3.1: Fit Parameters for LKα14. The line shapes were modeled with an effective QCC of 51.5 kHz, four idealized rotamers interchanging with rate k_{rot} and populations w:1:1:1. Librational motions were added as movement along an arc with steps of 5°, and jumps between consecutive sites at rate k_{arc}. The resulting spectra are shown in Figure 3.5.

performed using a threshold accepting algorithm as described in Section 3.3. The simulated spectra are shown in Figure 3.5, and the final parameters are listed in Table 3.1.

The parameters for fitting the spectra in the dry, neat state follow the expected trend based on the degree of involvement in the hydrophobic core. The rates and arc length decrease with involvement, while the fraction of the major rotameric conformation increases. The parameters for fitting the spectra obtained for the sample when lyophilized out of buffer follow a similar pattern. Compared to the neat state, the arc lengths are unchanged, but the speed of the diffusion along the arc is decreased. The preference for the major rotamer increase, while the rates varied. This highlights a confusion in the meaning of these parameters. It is in fact, better to instead consider the lifetime of the major rotameric state. Given that:

$$k_{rot} = \frac{k_{major->minor} + k_{minor->major}}{2} \tag{3.3}$$

and

$$p_{major} k_{major->minor} = p_{minor} k_{minor->major} \tag{3.4}$$

Since the populations are modeled as w:1:1:1, $wk_{major->minor} = k_{minor->major}$. Substituting this result into Equation 3.3 and rearranging:

$$k_{major->minor} = \frac{2k_{rot}}{1+w} \tag{3.5}$$

Because there are three minor conformations, the total rate of the major rotamer exchanging to a minor conformation, is three times that value, meaning the lifetime of the site is therefore:

$$\tau_{major} = \frac{1+w}{6k_{rot}} \tag{3.6}$$

Referring to the τ_{major} values given in Table 3.2, the expected trends in the mobility of this site are observed. L5 is the most mobile, then L11, and L8 is the most restricted. Moving from the dry states to the hydrated states, the mobility of all sites is increased. Comparing the neat and buffered states, it is interesting to note that the lifetime of L5 and L11 increases, while that of L8 decreases, consistent with phosphate buffer interacting with the exterior of

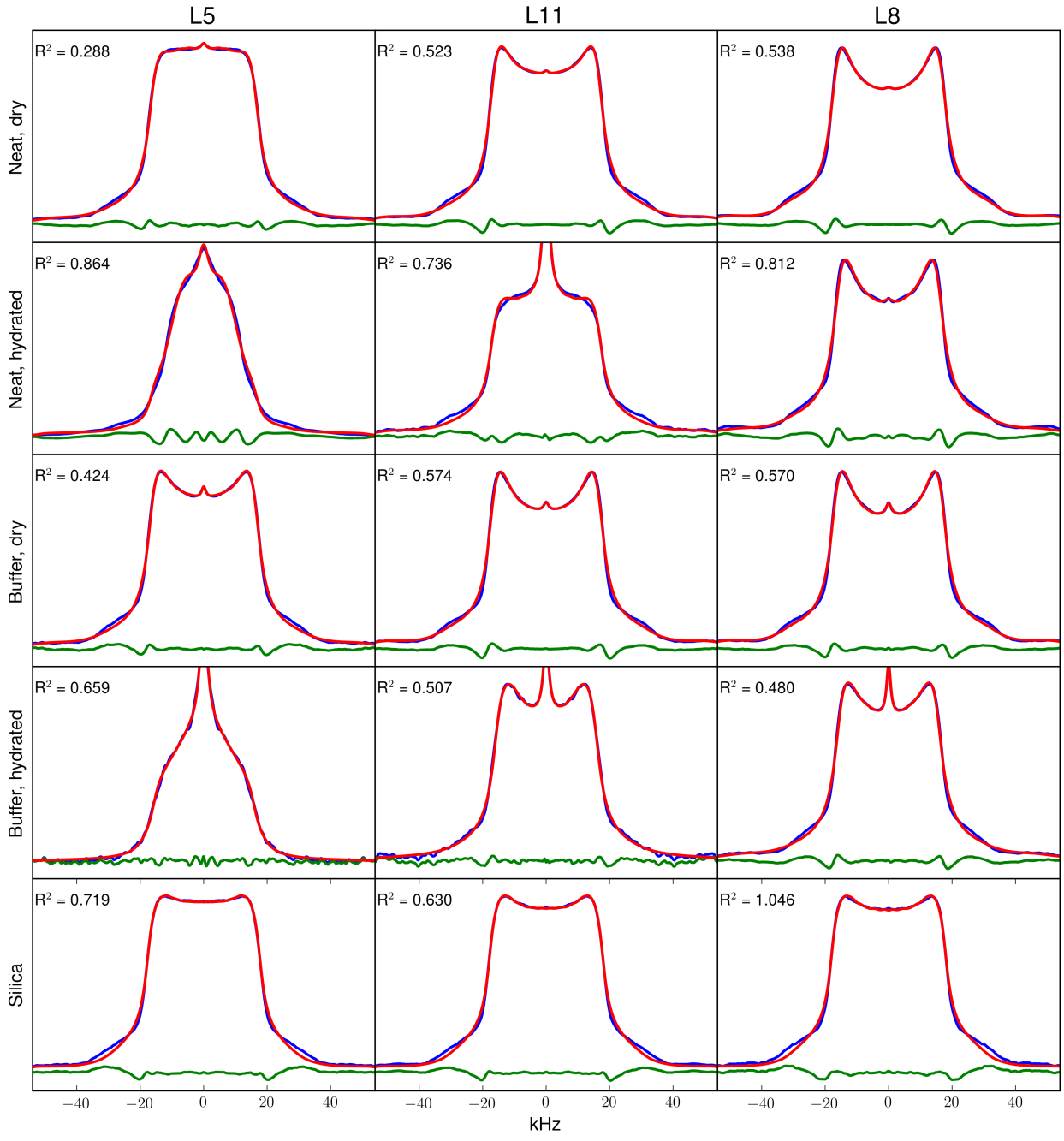

Figure 3.5: Fitted LKα14 QE Line Shapes: Experimental line shapes in blue, overlaid with fits in red, with the difference shown in green. The R^2 is calculated for the points between ±80kHz. Parameters for the fit are given in Table 3.1.

	Neat		Buffer		Silica
	Dry	Hydrated	Dry	Hydrated	
L5	29.7µs	0.4µs	33.3µs	1.3µs	8.3µs
L11	36.3µs	24.8µs	39.6µs	21.2µs	9.5µs
L8	55.5µs	41.7µs	48.7µs	32.2µs	17.7µs

Table 3.2: Summary of τ_{major} (in µs) parameter derived from the populations and k_{rot}.

the bundle and restricting mobility with the sites it most directly interacts with. At the same time it is likely disrupting the packing in the center of the bundle, increasing the size of the hydrophobic pocket.

The spectra for the neat, hydrated L5 and L11 are adequately fit by the parameters sets, but it is not necessarily the case that the arc length is the shorter length reported. These spectra display a high degree of anisotropic motion and are not necessarily optimally fit, which explains discrepancies seen in the trends. More data could have been collected to clarify the model, such as different types of spectra, or static spectra as various temperatures, but for the purposes of this study, these spectra qualitatively demonstrate the difference in mobility.

Finally, in the silica co-precipitated state, the spectra are most indicative of increased rotameric motion – evident from the decreased lifetimes reported in Table 3.2. The rate of this motion is significantly increased though the uneven distribution of populations remains. Additionally, there appears to be far less librational motion, while there is still rapid diffusion along an arc, the length of the restricted arc is much decreased. The arc motion in these samples is consistent with the diffusion seen by Vugmeyster *et al.* in protein hydrophobic core studies, while the neat and buffered states still experienced longer diffusive motions. While the rotameric exchange rates are larger than those reported by Vugmeyster *et al.*, it is possible that the structure of the hydrophobic core is different in this case, leaving a larger

pocket and allowing for increased exchange.

These parameters were also used to fit MAS data, shown in Figure 3.6. The simulated line shapes are in reasonable agreement with the experimental data. The sidebands are broader in the simulation, which leads to the possibility that there is a distribution of jump rates in the sample. Work by Hologne *et al.* showed that their data was best fit without a distribution due to the broad nature of their line shapes.[73] While the opposite does not necessarily hold, based on the fit it is reasonable to suggest that the discrepancies are largely due to a distribution of environments giving different rotameric jump rates. This could be modeled, but that is beyond the scope of what is discussed here.

To analyze the T_1IR data, it is not good practice to fit the partially relaxed line shapes, due to distortions from finite pulse widths leading to incomplete excitation that are not accounted for in the simulations. These distortions are largely averaged out in the anisotropy profile, which shows relaxation rates as a function of frequency. The parameter set was also used to generate T_1 anisotropy profiles, shown in Figure 3.7. For completeness, samples of the series used to generate the profiles are included in Figure 3.8, and prove to be a fairly good fit.

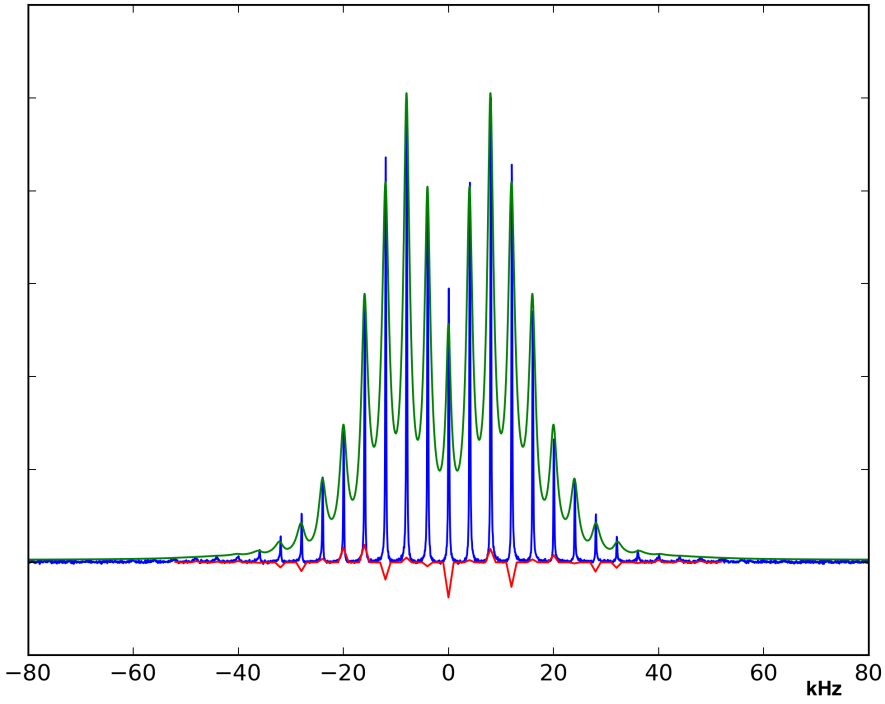

Figure 3.6a: Fitted LKα14 MAS Spectra: L5

(Blue: Experimental spectrum, Green: Simulated spectrum, Red: Difference in sideband intensities)

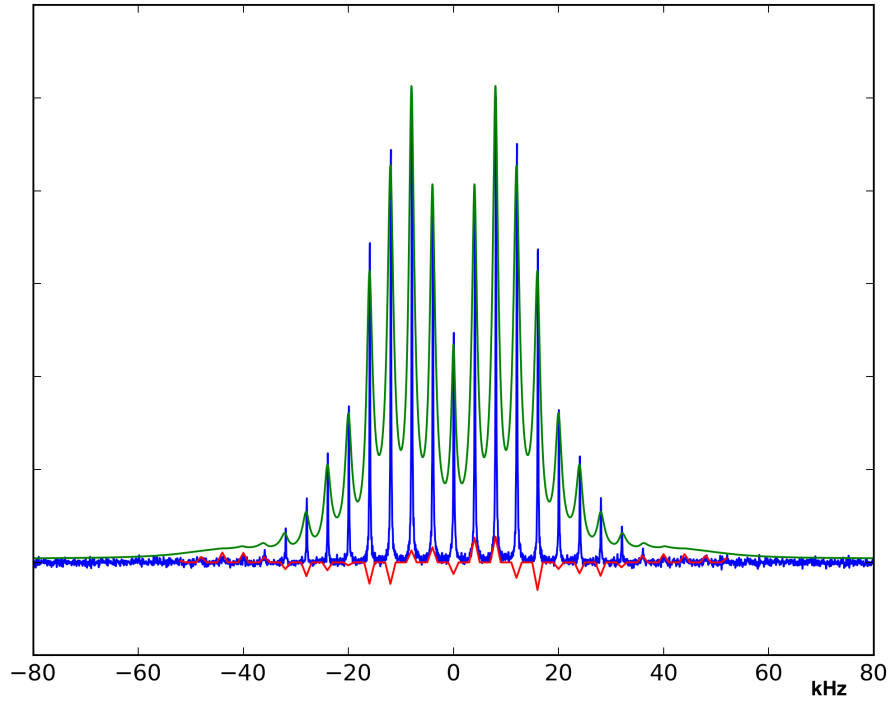

Figure 3.6b: *(continued)* L11

(Blue: Experimental spectrum, Green: Simulated spectrum, Red: Difference in sideband intensities)

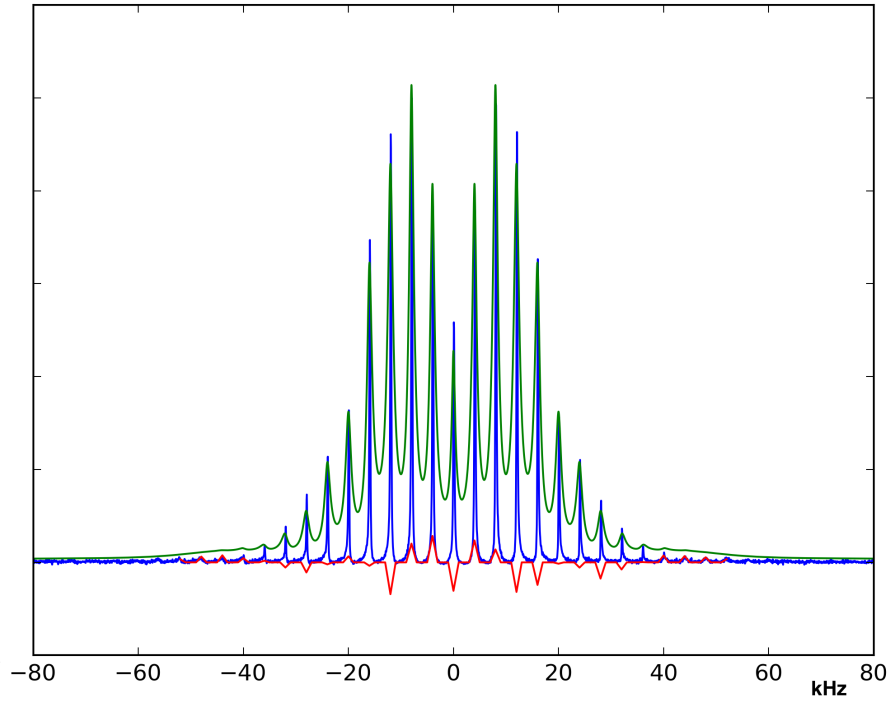

Figure 3.6c: *(continued)* L8

(Blue: Experimental spectrum, Green: Simulated spectrum, Red: Difference in sideband intensities)

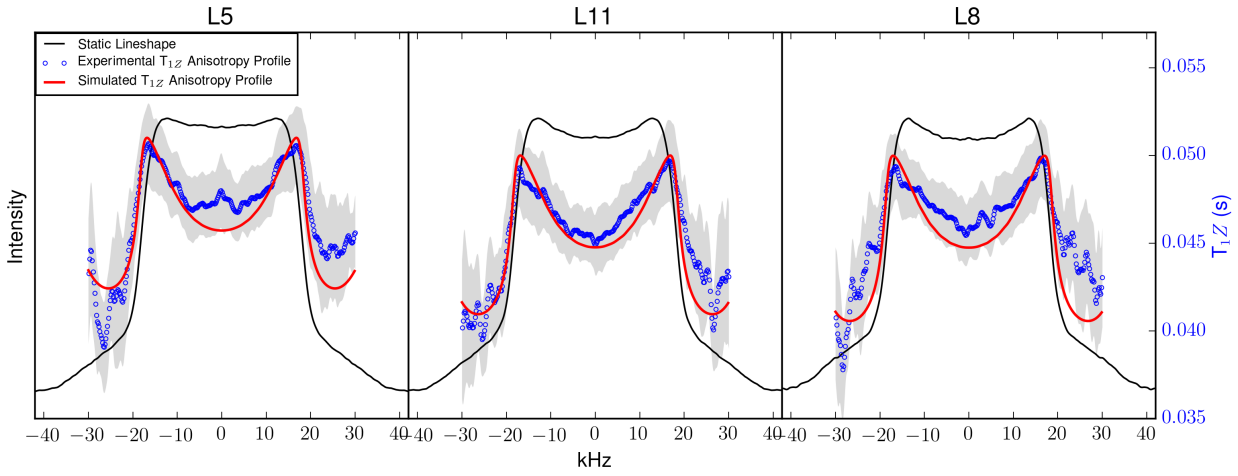

Figure 3.7: Fitted LKα14 T_{1Z} Anisotropy Profiles. *(Black Line: Static line shape, included for reference, Blue circles: Experimental Anisotropy, error shown by Grey overlay, Red Line: Simulated Anisotropy)*

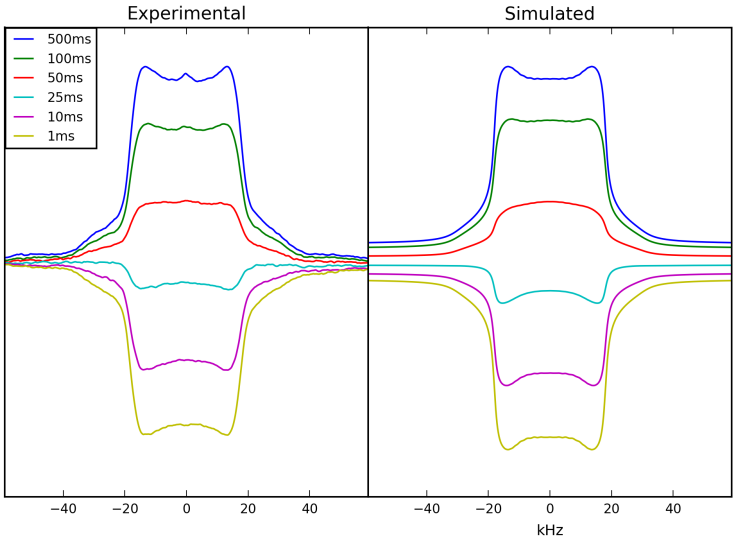

Figure 3.8a: LKα14 T1Z partially relaxed line shapes were used to generate the T_{1Z} Anisotropy Profiles, and are included here for reference. These are not fit directly to avoid complications of finite pulse width distortions.

L5

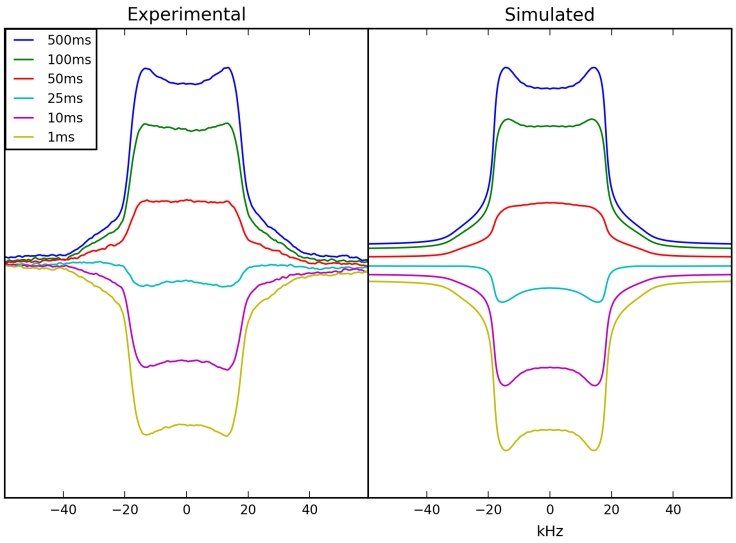

Figure 3.8b: *(continued)* L11

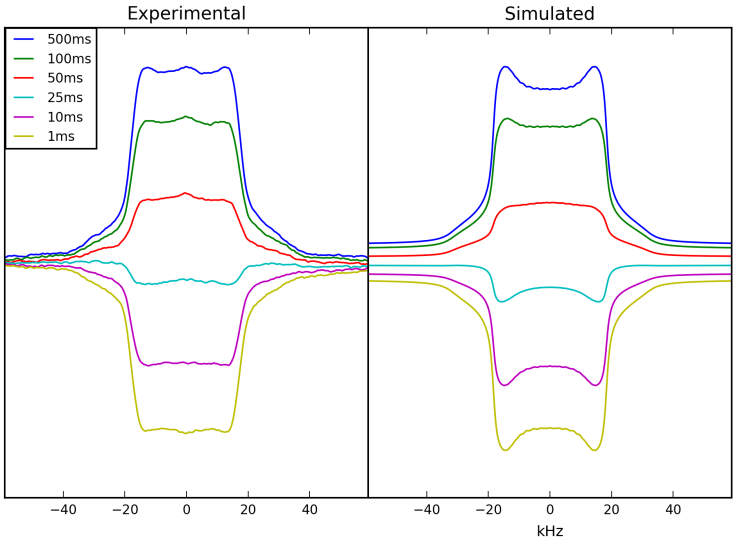

Figure 3.8c: *(continued)* L8

3.7 Conclusions

Static line shapes followed the expected trends of a tetrameric bundle in the neat and buffered states, with the degree of mobility decreasing with increased involvement in the hydrophobic core of the proposed tetrameric bundle.[48–50] The addition of the buffer increases the mobility of L8, while decreasing that of L5 and L11. The interactions of the lysine with the phosphate would introduce steric hindrance to the more exposed sites, and disruption of the packing would increase the size of the hydrophobic core region.

In the silica co-precipitated state, the trend was still present, though less apparent, and the spectra demonstrated features consistent with increased rotameric motion and decreased librational motion. The arc motion is more consistent with the diffusion seen by Vugmeyster *et al.* in protein hydrophobic core studies. The replacement of water with silica surrounding the tetrameric bundles could alleviate the hydrophobic pressure, loosening the packing in the hydrophobic core and allowing for rotameric exchange. Additionally, the MAS data suggests that there is a distribution of environments and rates present, the modeling of which is not attempted here and could be pursued in the future. Data collection at multiple temperatures would also give better insight into the motional modes present.

Based on this series of spectra, it is likely that the peptide remains in the tetrameric bundle. The leucine still appears to be in a hydrophobic core environment and there is no sign of disruption of this packing in the series of spectra presented. This means it is unlikely that the peptide packing rearranged from the preferred tetrameric bundling.

3.8 Supplemental: Comparing Models for Quantitative ^{2}H Line Shape Analysis

3.8.1 Final Arc Fit

Data and fits from the previous figures are reported here for reference. All three data types appear to be reasonably well fit with this model, despite the rates being an order of magnitude higher than those reported by Vugmeyster *et al.* for leucine dynamics in a hydrophobic core.

Site	$k_{arc}\,(/10^7 s^{-1})$	$k_{rot}\,(/10^4 s^{-1})$	Arc Length	w:1:1:1
L5	1.3	26.2	35°	12.1
L11	1.4	26.8	35°	14.3
L8	1.5	29.8	30°	14.8

Table 3.3: Arc Parameters for Silica Fits: Consolidated here for comparison with other models

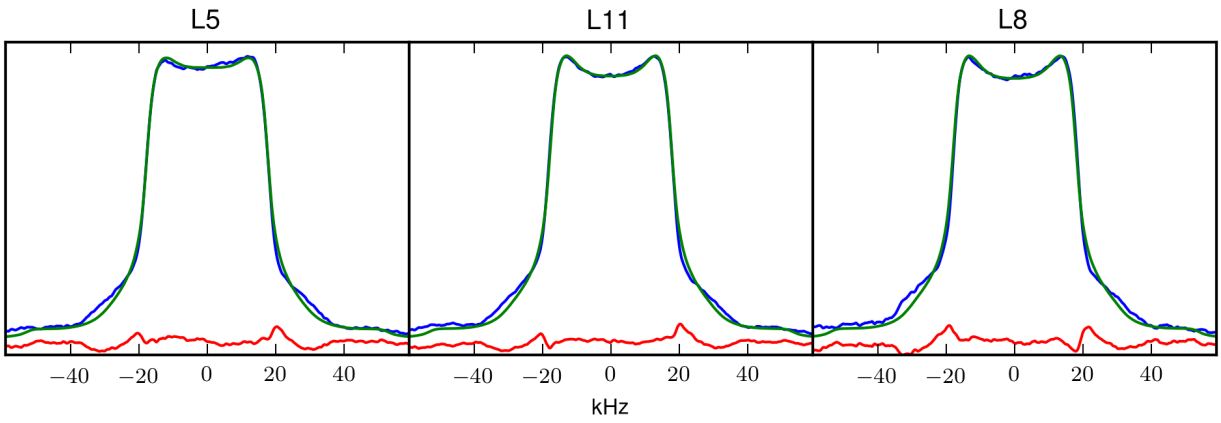

Figure 3.9: Arc QE Fits: Rescaled here from Figure 3.5 for reference.
(Blue: Experimental spectrum, Green: Simulated spectrum, Red: Difference)

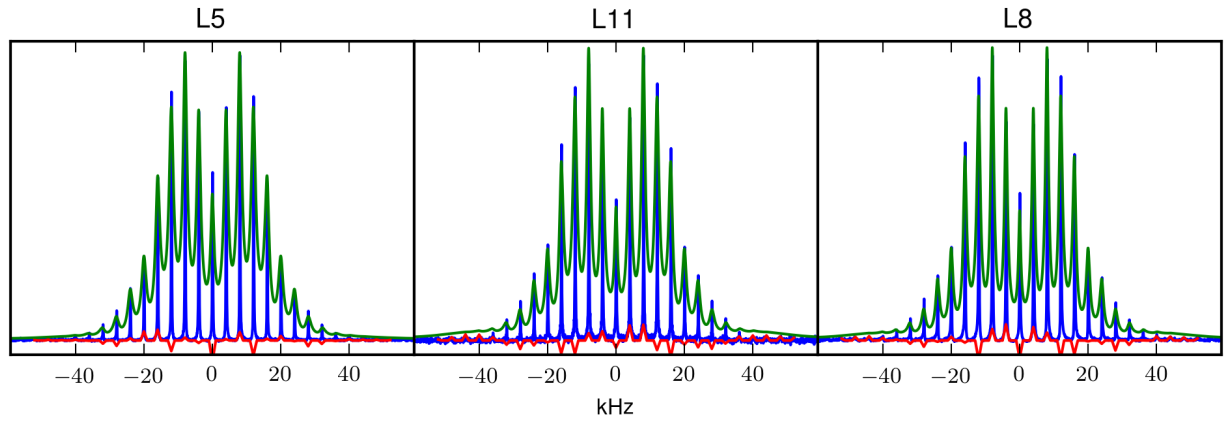

Figure 3.10: Arc MAS Fits: Rescaled here for easy reference and comparison to alternate models tried.

(Blue: Experimental spectrum, Green: Simulated spectrum, Red: Difference in sideband intensities)

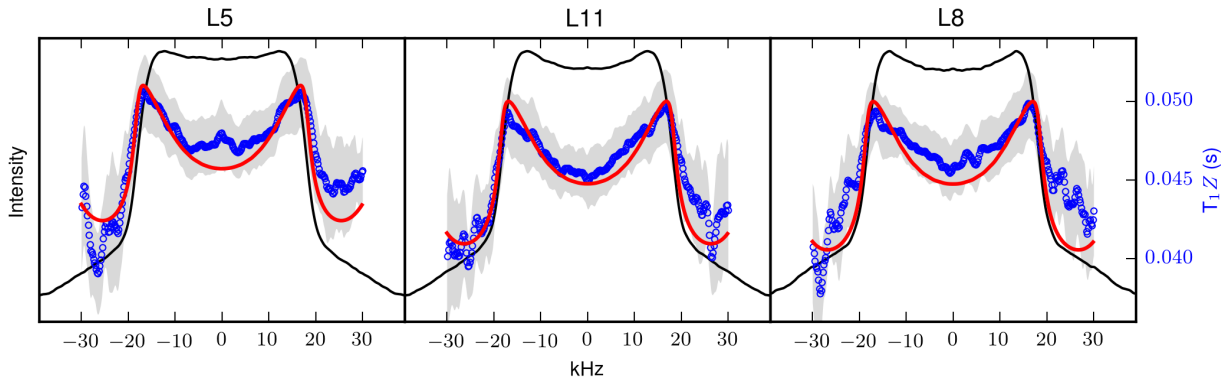

Figure 3.11: Arc T_1 Fits: Reproduced here for easy reference and comparison to alternate models tried.

(Black Line: Static line shape, included for reference, Blue circles: Experimental Anisotropy, error shown by Grey overlay, Red Line: Simulated Anisotropy)

3.8.2 Alternate Arc Fit

Presented here is an alternate parameter set, using the same 4-rotamer + variable length arc model that was used to fit the data. The rotamer exchange rates were constrained to be on the order of $10^4 s^{-1}$, to be closer to the values reported by Vugmeyster *et al.*. The parameters for this fit are presented in Table 3.4. Overall, fitting the QE spectra with a decreased k_{rot} lead to a model with an increased k_{arc}, and arc length, that is, faster librational movement along a longer trajectory. Additionally there is an overall increase in the w:1:1:1 ratio, indicating a prediction of increased steric hindrance relative to the first model.

The QE fits using this model, shown in Figure 3.12, appear to do a better job of fitting the shoulder region of the spectrum, and based on that alone may lead one to believe it is in fact a better fit. However, MAS spectra simulated from this model show significant side band broadening, shown in Figure 3.13, and the discrepancy between that and the experimental data is an indicator that it is not a good fit. Furthermore, the T_1 anisotropy profiles, shown in Figure 3.14, are not as close a fit as those shown in Figure 3.11.

Site	$k_{arc}\,(/10^7 s^{-1})$	$k_{rot}\,(/10^4 s^{-1})$	Arc Length	w:1:1:1
L5	5.3	6.9	50°	13.7
L11	2.7	7.2	50°	15.7
L8	3.4	5.9	45°	14.4

Table 3.4: Alternate Arc Parameters for Silica Fit: Slower rotameric exchange

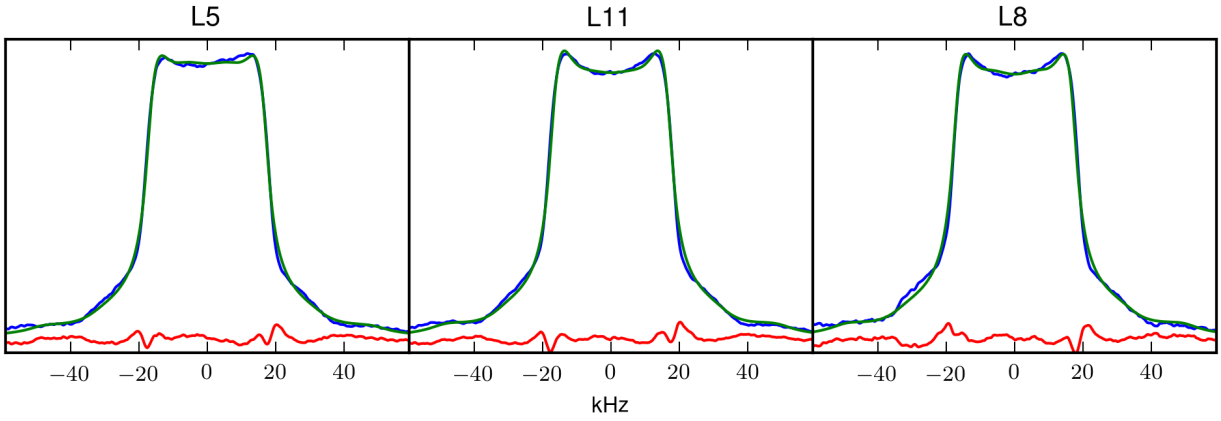

Figure 3.12: Alternate Arc QE Fits: A slower k_{rot} was used. Note the better fit in the shoulder region compared to Figure 3.9.

(Blue: Experimental spectrum, Green: Simulated spectrum, Red: Difference)

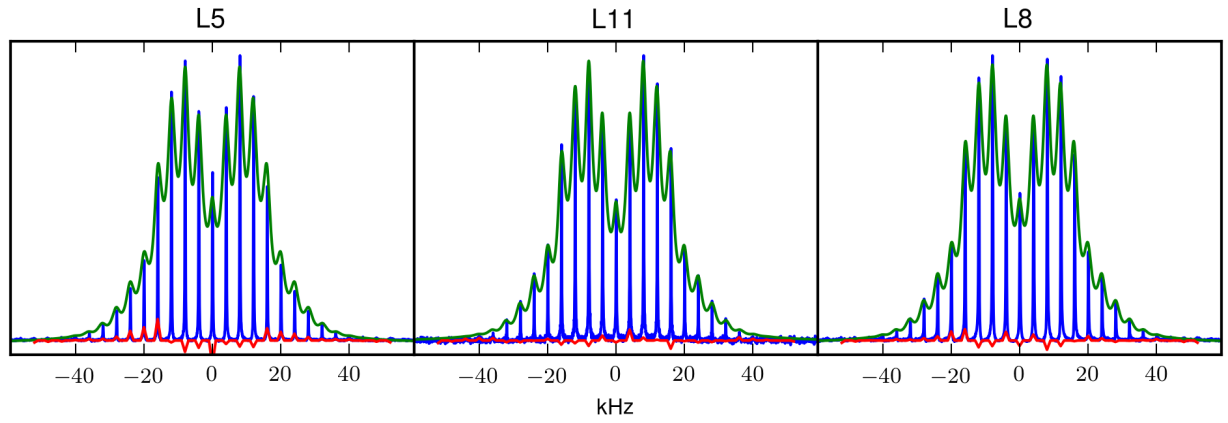

Figure 3.13: Alternate Arc MAS Fits: A slower k_{rot} was used. Note the wider line width compared to the simulated spectra in Figure 3.10.

(Blue: Experimental spectrum, Green: Simulated spectrum, Red: Difference in sideband intensities)

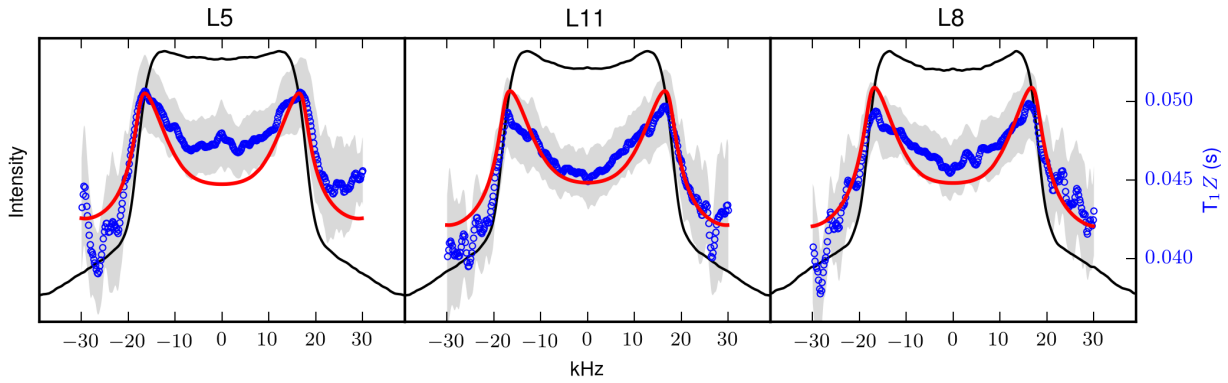

Figure 3.14: Alternate Arc T_1 Fits: A slower k_{rot} was used. Note the decreased quality of the fit compared to the simulated anisotropy profile in Figure 3.11.

(Black Line: Static line shape, included for reference, Blue circles: Experimental Anisotropy, error shown by Grey overlay, Red Line: Simulated Anisotropy)

3.8.3 Rotamer Library Derived Fit

Another approach is to fit the data with a model comprised of just rotameric jumps. While treating the nine rotational isomers as only four magnetically equivalent sites has proven adequate, the next step is to take full advantage of the computational power available, and pursue a line shape fit to all nine rotameric forms. Dunbrack backbone-dependent rotamer libraries give the relative probability of different rotameric forms, as well as the average value of the side chain torsion angles–χ_1 and χ_2–based on backbone torsion angles.[74] Therefore, using the backbone torsion angles determined by Zane *et al.* it is possible to get rotameric angles and probabilities. These torsion angles are converted into Euler angles, suitable for input into a modeling program. To get Ω_{PC} from a set of torsion angles, it is necessary

Rotamer Library			Methyl 1			Methyl 2			Deuteron		
χ_1	χ_2	Probability	α	β	γ	α	β	γ	α	β	γ
291.1	172.7	0.6045	271.2	6.9	340.1	59.7	34.3	167.3	177.9	165.8	347.5
271.1	298.9	0.0071	60.5	108.6	149.4	228.9	100.6	42.5	155.8	6.1	35.6
263.7	40.9	0.0210	311.8	124.1	48.1	44.5	89.1	175.6	28.9	66.2	100.5
74.3	165.1	0.0000	272.5	14.0	198.2	132.9	84.6	315.8	52.4	168.9	213.2
58.6	286.0	0.0000	66.1	97.7	7.5	9.4	162.5	11.9	359.8	50.1	261.2
70.0	86.4	0.0024	289.5	86.8	219.5	209.6	65.0	278.9	128.8	124.4	259.2
198.8	171.9	0.0203	271.4	7.6	72.6	67.3	77.5	316.9	257.4	121.2	278.4
193.5	283.1	0.0033	67.2	95.2	233.7	251.8	53.6	191.6	208.1	166.1	115.9
181.2	60.6	0.3413	299.7	109.0	118.5	251.6	124.1	69.7	198.4	88.0	330.8

Table 3.5: Sample torsion angles, in degrees, from the Dunbrack rotamer library, with corresponding Euler angles for each methyl group and the deuteron in d_7 Leu

to find the set of Euler angles corresponding to a rotation of $(0, 70.5^\circ, -\chi_2)$ followed by a rotation of $(0, 70.5^\circ, -\chi_1)$. Unlike the 4 site model, this model also requires explicit modeling of each methyl group separately; the Euler angles for the second methyl group are therefore obtained analogously, using χ_2+120° to define the relative orientation. Similarly, the minimal

contribution of the C_γ deuteron–appearing as a baseline increase with $< 5\%$ contribution, due to signal attenuation because of the longer relaxation time–is accounted for by adjusting χ_2 to $\chi_2 - 120^\circ$. Sample rotamer library data with corresponding rotation angles, is shown in Table 3.5. It is also worth mentioning that of the 9 sites, three of them are likely able to be eliminated from consideration, as the projected populations are $< 1\%$. The reason for this becomes evident when looking at the three dimensional structure, as the *gauche*(-) configuration of χ_1 directs the side chain back towards the helical backbone, which is a sterically unfavorable position.

Using torsion angles from the Dunbrack rotamer libraries, the spectra were simulated using just jumps between six of the nine possible rotameric conformations. The QCC was allowed to vary, as well at the populations of all six rotamers and three jump rates corresponding to changes in χ_1, χ_2 and both χ_1 and χ_2. The results are presented in Table 3.6. While in an ideal case, this model would have given us results that are more physically meaningful due to the accurate representation of all the rotameric contributions, in reality the results were less than ideal. It ultimately seemed that the complication of the model added too many parameters for the results to lead to meaningful physical conclusions.

Site	$k_1\,(s^{-1})$	$k_2\,(s^{-1})$	$k_{12}\,(s^{-1})$	QCC_{eff} (kHz)	p_1	p_2	p_3	p_4	p_5	p_6
L5	41.9	10.4	3.78×10^5	48.6	0.767	0.073	0.020	0.093	0.046	0.0001
L11	7.2	5.0	3.55×10^5	48.7	0.727	0.062	0.025	0.153	0.0331	10^{-8}
L8	10.8	8.3	4.12×10^5	48.8	0.730	0.044	0.031	0.165	0.030	10^{-8}

Table 3.6: Rotamer-Only Parameters for Silica Fit

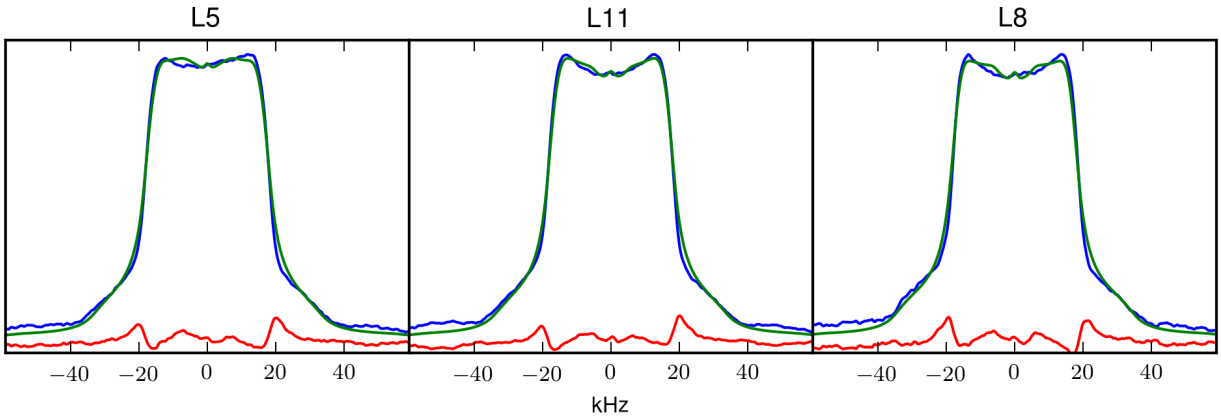

Figure 3.15a: Rotamer-Only QE Fits: The "horn" region is not as closely fit, and required a water peak in the center to account for some of the spectral intensity.

(Blue: Experimental spectrum, Green: Simulated spectrum, Red: Difference)

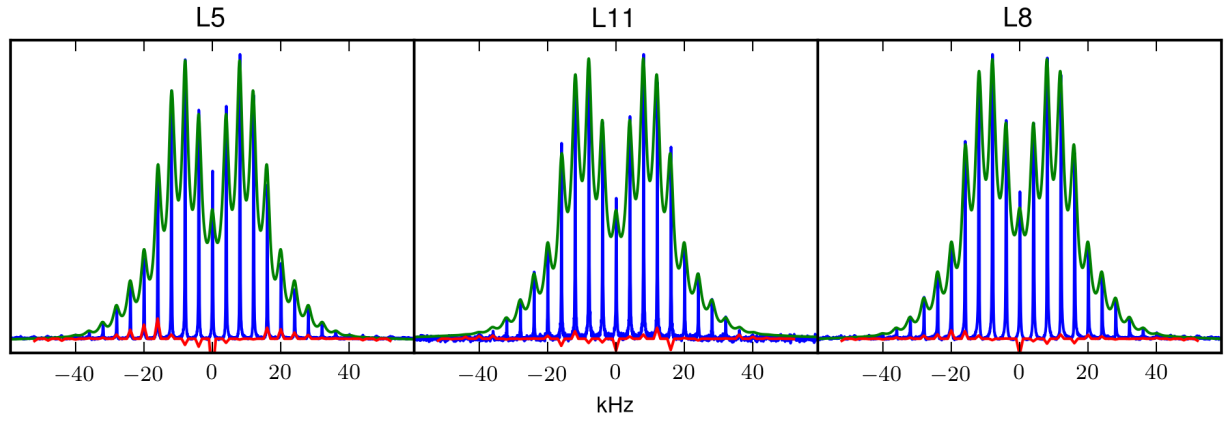

Figure 3.15b: Rotamer-Only MAS Fits: Note again, the wider line width compared to the simulated spectra in Figure 3.10.

(Blue: Experimental spectrum, Green: Simulated spectrum, Red: Difference in sideband intensities)

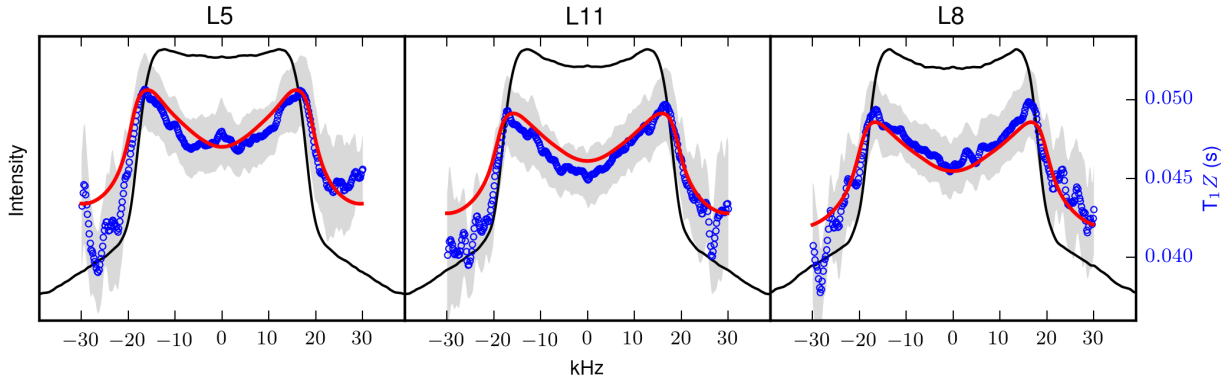

Figure 3.15c: Rotamer-Only T_1 Anisotropy Profile: The anisotropy profile is significantly different than that depicted for the other two models. The noise on the experimental data is not small enough to conclusively say which is the best fit.

(Black Line: Static line shape, included for reference, Blue circles: Experimental Anisotropy, error shown by Grey overlay, Red Line: Simulated Anisotropy)

Chapter 4

ISOLEUCINE DYNAMICS AND ^{2}H-^{13}C HETERONUCLEAR CORRELATION NMR

4.1 Introduction

4.1.1 An extension of leucine dynamics

Having demonstrated the efficacy of extracting motional information from ^{2}H ssNMR data for leucine side chains, it seems a logical follow up to apply it to other amino acids. Isoleucine is another hydrophobic amino acid with potentially interesting methyl group dynamics. However, while there is a wealth of leucine dynamics literature, there is a paucity of analogous isoleucine analysis. In a study of amino acid side chain motions through relaxation experiments, Oldfield *et al.*, states that due to its complicated structure, shown in Figure 4.1, isoleucine requires further study to properly model.[75] Follow up studies are few in number, and include a method of solution state χ_2 determination, using ^{13}C CPMG (Car-Purcell-Meiboom-Gill) relaxation dispersion–which has been used to analyze both leucine and isoleucine conformational exchange.[76,77]

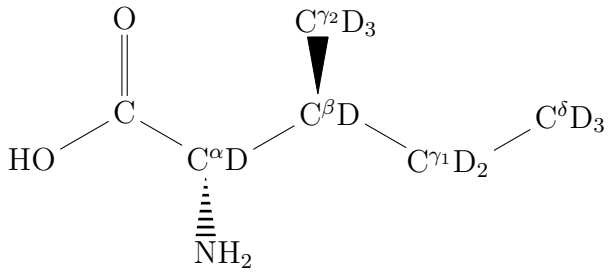

Figure 4.1: Structure of d_{10} isoleucine.

The structure of isoleucine, shown in Figure 4.1, is asymmetric, leading to two inequivalent methyl group environments. The inequivalent methyl groups complicate the line shape. While leucine can be purchase with $d_7 - isopropyl$, $d_3 - methyl$ and d_{10} labeling, isoleucine with ^{2}H labeling is available for purchase only in the perdeuterated form, meaning that all 10 hydrogen atoms are replaced with deuterium, as shown in Figure 4.1. Since selectively labeled material is not readily available, the motions along the side chain cannot be examined separately. The resulting line shape includes not only the contributions from the two non-equivalent methyl groups, but also broader line shapes corresponding to the deuterons at the α, β and γ positions.

4.1.2 Applications

If this analysis method proves successful, this technique could then be applied to isoleucine dynamics with the amino acid incorporated into a peptide sequence. A potential example is R5 (H-SSKKSGSYSGSKGSKRRIL-OH), another synthetic silaffin, which is capable of silica precipitation.[13,14,78] This is particularly interesting because the RRIL moiety has been shown to be important to silica morphology mediation.[14,78] The leucine is hard to label because in solid-phase peptide synthesis, the C-terminal amino acid is bound to a resin, and so is more difficult to isotopically label. Therefore, it would be advantageous to have a method for evaluating the dynamics of the isoleucine side chain instead.

4.1.3 Methods

Building upon the techniques for leucine dynamics modeling presented in Chapter 3, a similar analysis is done on isoleucine spectra by modeling an overall spectrum as the sum of each site's contribution. To further verify the veracity of this method it is desirable to have a method of separating out these contributions. The broader deuteron contributions can be reduced by decreasing the recycle delay, shown in Figure 4.2, but it is preferable to separate out these motions entirely. To this end, ^{2}H-^{13}C heteronuclear correlation (HETCOR) spectroscopy

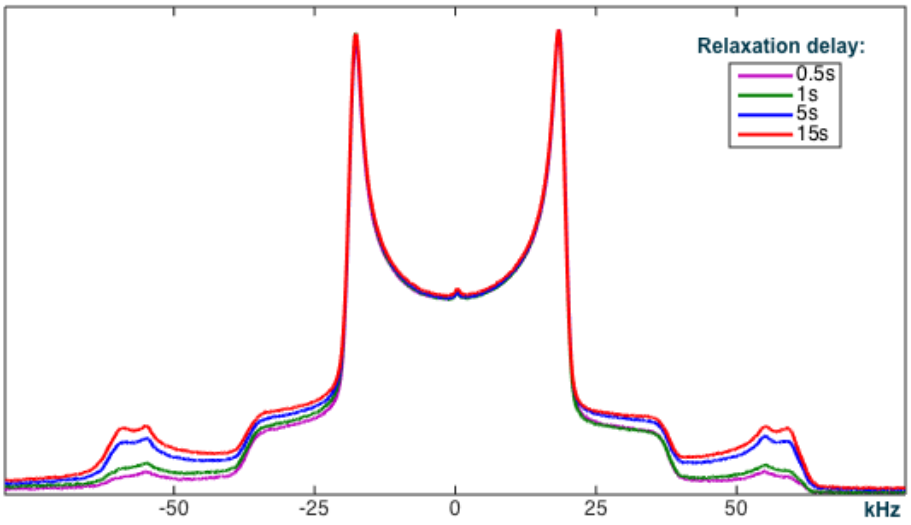

Figure 4.2: Isoleucine quadrupolar echo spectra acquired with various relaxation delays. Shortening the relaxation delay decreases the intensity of the wider peaks.

was implemented, using uniformly ^{2}H-, ^{13}C-, ^{15}N- labelled isoleucine, to separate out the deuterium signals based on their carbon connectivity.[79–82]

4.2 Methods

4.2.1 ^{2}H Quadrupolar Echo

All static quadrupolar echo experiments were performed at 11.74T field (76.77 MHz deuterium Larmor frequency) using a home-built, single-channel, static deuterium probe with a Bruker Avance III 500 MHz narrow-bore spectrometer and a $\frac{\pi}{2}$ pulse time of 2.9 μs. Quadrupolar echo experiments used eight-step phase cycling, with an echo delay of 40 μs, and a recycle delay of 0.4s. ^{2}H offset was set such that liquid D_2O is on resonance. Line shapes were processed by left-shifting to the echo maximum prior to Fourier transform, followed by 1 kHz line broadening and phase correction.

4.2.2 ^{2}H Magic Angle Spinning

MAS line shapes were acquired with the same magnetic field, but with a Bruker TriGamma probe. These experiments employed a single ^{2}H $\frac{\pi}{2}$ pulse width o 4.0 μs and were performed with spinning speeds of 5 kHz. 16 scans were collected with a 1s relaxation delay between scans. After left-shifting to the peak of the first echo, FIDs were Fourier transformed and phase-corrected without further processing.

4.2.3 ^{2}H-^{13}C Heteronuclear Correlation

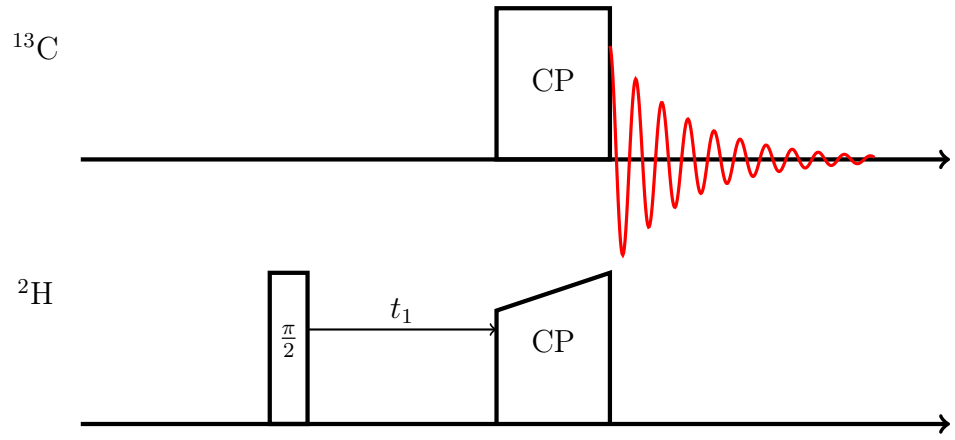

Figure 4.3: 2D ^{2}H-^{13}C HETCOR Pulse Program

Solid-state NMR spectra were collected on a Bruker Avance III 500 MHz, narrow-bore spectrometer equipped with a 3.2mm MAS probe operating in ^{1}H-^{13}C-^{2}H triple resonance mode. The 2D ^{2}H-^{13}C CP-MAS HETCOR pulse sequence is depicted in Figure 4.3. A deuterium $\frac{\pi}{2}$ pulse of 3.8μs was applied, then after t1 evolution, the magnetization was transferred to ^{13}C by cross-polarization with a contact time of 2000 μs, using an rf ramp on ^{2}H, and then ^{13}C signal was detected. ^{2}H offset was set such that liquid D_2O is on resonance. The recycle delay was 0.5 s.[80–82]

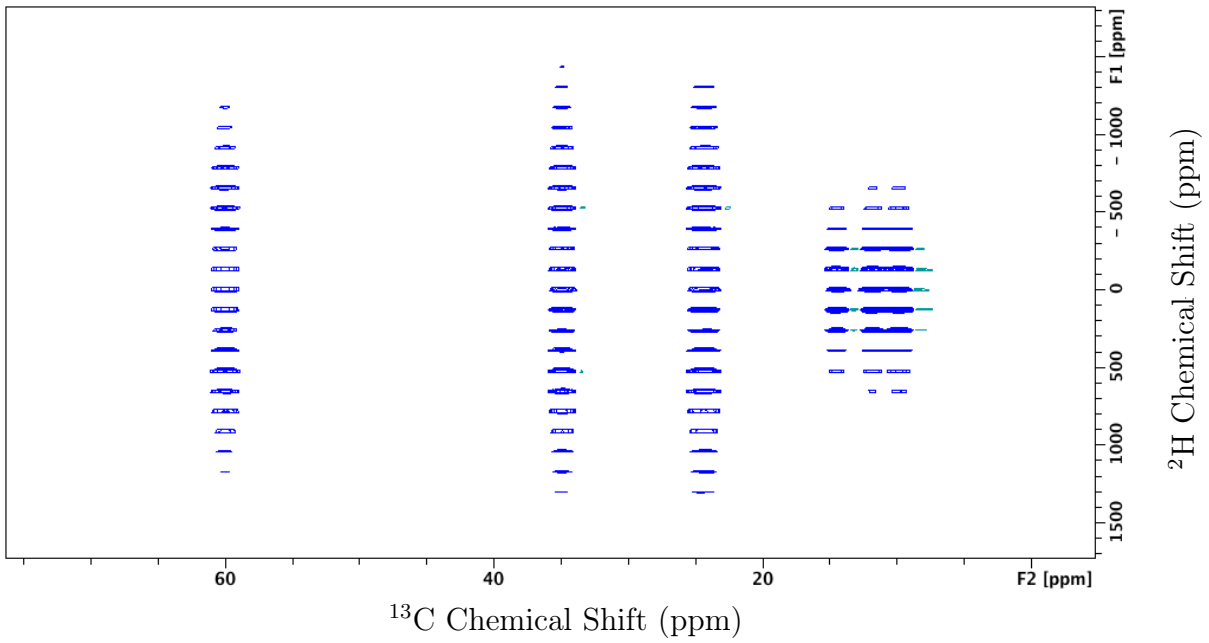

Figure 4.4: An overview of the 2D ^{2}H-^{13}C CP-MAS HETCOR. Spectral width was 50 kHz for ^{13}C and 500 kHz for ^{2}H, a total of 4096 t1 increments with 4 scans each were collected.

4.3 Results

The overall 2D HETCOR spectrum is shown in Figure 4.4, with peak assignments for the ^{13}C shifts given in Figure 4.5. Peaks assignments are based on literature work, which determined that the two different rotameric populations in monomeric isoleucine, $g^{+}t$ and tt,[83] lead to inequivalent environments for $C^{\gamma 2}H_3$ and two different chemical shifts in the ^{13}C spectrum.[84] Interestingly, the dominate forms reported by the Dynameomics rotamer library are $g^{+}t$ and $g^{-}t$, indicating a difference based on protein incorporation.[85]

4.3.1 Model

Taking inspiration from past work by Vugmeyster *et al.*, the data was fit using a simple arc motion, treated as a rotation of the $C_{\alpha}-C_{\beta}$ bond, causing the rest of the molecule to rapidly diffuse along a restricted arc with a length of 30°, jumping steps of 5° at a rate of $5 \times 10^{8} s^{-1}$.

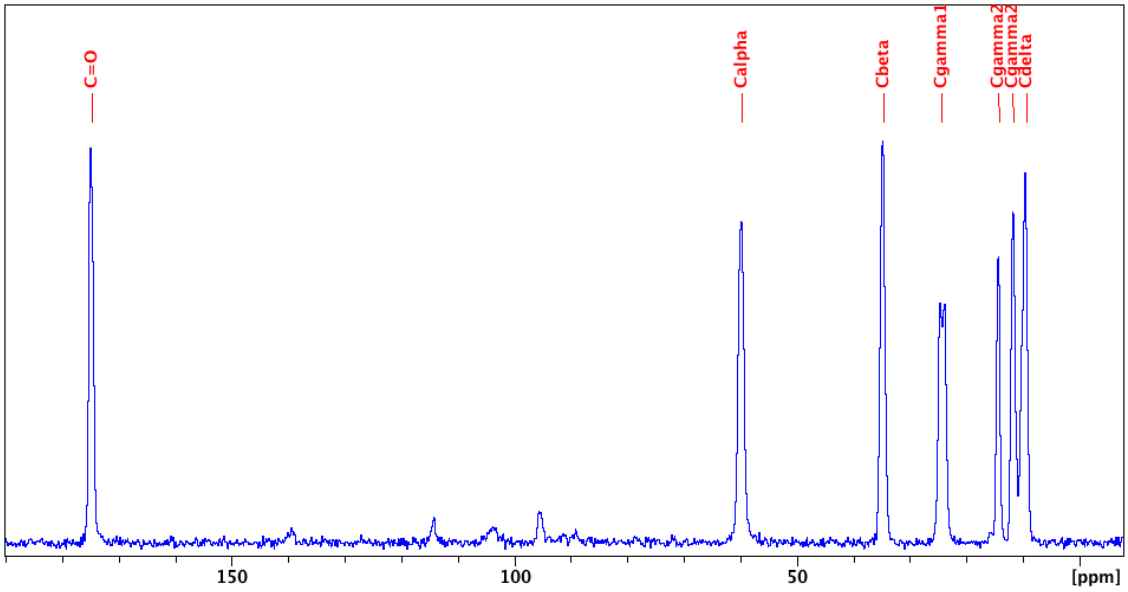

Figure 4.5: 1D ^{2}H-^{13}C CP-MAS spectrum of isoleucine. Peak assignments listed above correspond to the carbon sites as labeled in Figure 4.1.

Without inclusion of rotameric exchange, the dominate conformations can be assumed to generate the same ^{2}H line shapes. The variation in the major rotameric populations is in the χ_1 angle, and all are *trans* in χ_2. Since both the arc motion and χ_1 define the rotation around the $C_\alpha - C_\beta$ bond, these can be assumed to be the same without loss of generality. The QCC of the C_α-D, C_β-D and C_γ-D was assumed to be 160kHz, while the effective QCC of the methyl groups was set to 53 kHz.

The ^{2}H spectra are extracted from the 2D HETCOR, the overview of which is shown in 4.4. These are broken down into individual pieces in the MAS spectra, shown with the corresponding fits in 4.6. Overall the simulated spectra are in good agreement with the experimental slices. Since monomeric isoleucine was used, C_α is not anchored as firmly as it would be in a peptide, and since the mobility of this site is ignored there are more discrepancies in the line shape fitting. This issue would be eliminated upon incorporation into a peptide.

Overall fits for the MAS line shapes for two different spinning speeds are shown in Figure 4.7, and also appear to be in good agreement. The MAS spectra were simulated by adding together the individual contributions and assuming that the contributions of the broader components (C^α-^{2}H, C^β-^{2}H, and C^{γ_1}-$^2H_2$) were attenuated by a factor of 3 due to the longer relaxation time at these sites.

4.4 Conclusions and Future Work

The ability to separate out the individual contributions to the line shape using HETCOR is demonstrated and isoleucine dynamics have been fit in the monomeric state. This method could be applied to determine isoleucine dynamics with the amino acid incorporated into a peptide sequence. A potential example is R5 (H-SSKKSGSYSGSKGSKRRIL-OH), another silaffin, which is capable of silica precipitation.[13,14,78] Additional work could include relaxation measurements, and, following literature precedent,[80–82] relaxation measurements in conjunction with HETCOR.

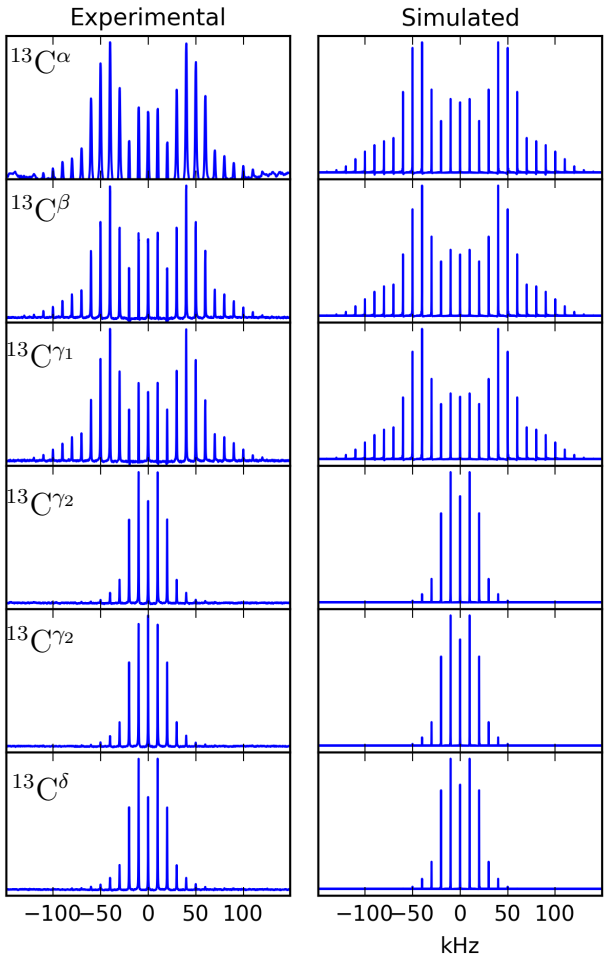

Figure 4.6: Isoleucine HETCOR Slices and Fits

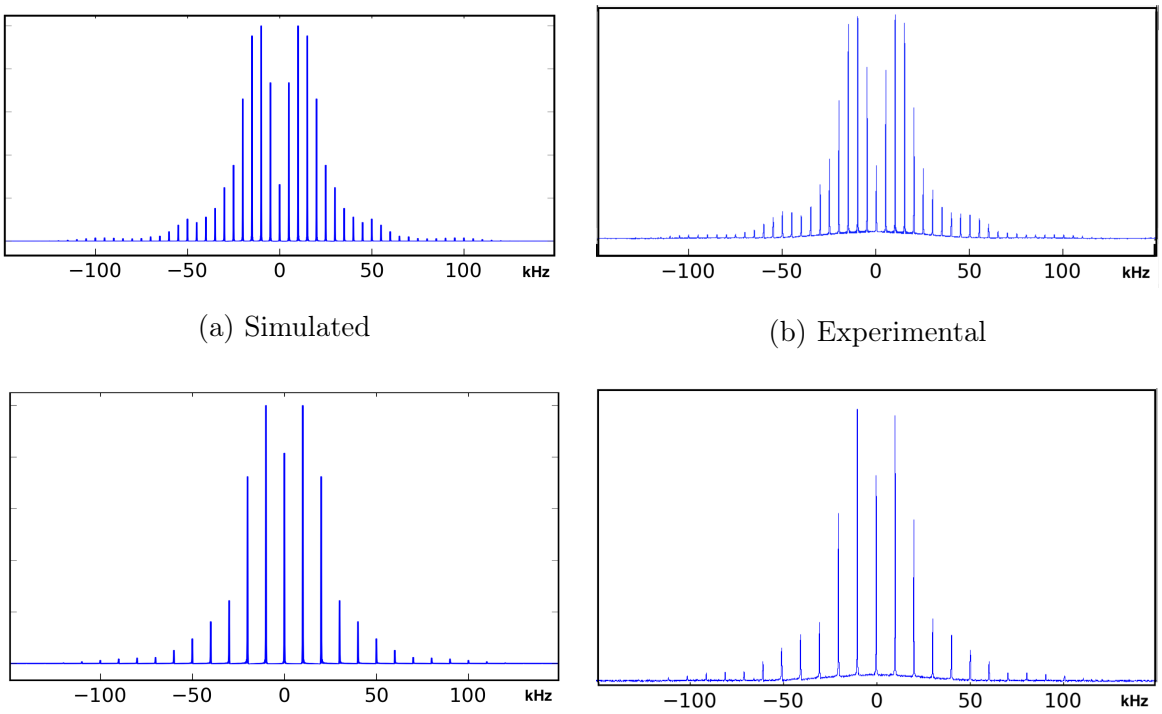

(a) Simulated

(b) Experimental

(c) Simulated

(d) Experimental

Figure 4.7: Experimental and Simulated MAS Line Shapes for Isoleucine at 5kHz and 10kHz spin rates.

Chapter 5

USING $^{13}C\{^{2}H\}$ REDOR TO EXPLORE THE INTERACTION BETWEEN LEUCINE AND DECANOIC ACID VESICLES

5.1 Introduction

Work presented in this chapter focuses on better understanding how biological building blocks may have come together to create life in a prebiotic environment. All work presented was done in collaboration with Dr. Roy A. Black and Professor Sarah L. Keller at the University of Washington. Richard Dawkins has famously stated that "biology is the study of complicated things that give the appearance of having been designed for a purpose."[86] The question then is how did prebiotic compounds such as amino acids and nucleobases aggregate in the absence of the complex protein systems of cells? Work by Black *et al.* showed that specific hydrophobic amino acids stabilize decanoic acid vesicles against salt-induced flocculation.[87] Specifically, work presented here examines the association of leucine with decanoic acid vesicles. This association may have induced early prebiotic peptide formation.

5.1.1 Decanoic Acid Vesicles

Early cell membranes were likely composed of simple fatty acids as opposed to the more complex phospholipids found in modern cells.[88–90] Fatty acids are composed of a small hydrophilic headgroup and a long hydrophobic akyl chain tail, as shown in Figure 5.1. In water, certain fatty acids self-assemble into vesicles as shown in Figure 5.2. Decanoic acid is the most commonly used fatty acid for modeling prebiotic systems because it is thought that shorter fatty acids were more prevalent due to their chemical simplicity, and decanoic acid is the fatty acid with the shortest alkyl chain that forms stable vesicles.[91] Additionally, decanoic acid has been found on meteorites, supporting its potential prebiotic presence.[92]

The vesicles formed by decanoic acid create a small hydrophobic sheet, as well as an inner pocket of aqueous solution. Both of these features may have led to the aggregation of prebiotic components, an essential first step in the formation of more complicated molecules. Roy Black *et al.* have shown that certain RNA bases and ribose bind to decanoic acid vesicles and stabilize the vesicles against salt-induced flocculation.[93] More recently, Black *et al.* showed that certain non-polar amino acids, including leucine and isoleucine, are also able to stabilize vesicles in high salt concentrations. In contrast, alanine and glycine, which are less hydrophobic, were shown to have little effect on the stability of the fatty acid vesicles.[87] To better understand this preferential stabilization in the presence of leucine, I employed solid-state NMR techniques to investigate whether leucine binds to the surface or is incorporated into the core of the bilayer.

5.1.2 $^{13}C\{^{2}H\}$ REDOR

Rotational-echo double-resonance (REDOR) NMR spectroscopy is a method for determining heteronuclear distances in solid samples. This technique is commonly implemented in the study of systems which are not easily characterized by crystallography. REDOR is routinely used to measure distances of up to 7 Å between ^{13}C and ^{15}N nuclei in peptide conformational studies. In a ^{13}C{X} REDOR experiment, the dipolar dephasing of ^{13}C spins by the other nucleus, X is monitored. Dipolar coupling is inversely proportional to the cube of the distances, so at longer distances there is a rapid increase in uncertainty. Here ^{13}C{^{2}H} REDOR is employed, in large part due to the availability of selectively deuterated decanoic acid.

The measurement of dephasing as a function of time was accomplished by recording pairs of spectra at different recoupling times, using the pulse sequence shown in Figure 5.3.[94–97] In both spectra, the signal is generated by cross polarization of magnetization from ^{1}H to ^{13}C, followed by a series of rotor-synchronized π pulses on the ^{13}C channel to refocus the magnetization. The S_0 is the spectrum recorded without recoupling to ^{2}H, while the S_1 is generated by adding a series of π pulses on the ^{2}H channel interleaved with the refocusing pulses on the ^{13}C channel. Note that in the case of ^{2}H as the dephasing nucleus, some have

opted to use a composite π pulse to ensure inversion of the full signal, however this is not necessary given a sufficiently hard short π pulse.[94–97]

From these spectra, the change in intensity, $\Delta S = \frac{S_0 - S_1}{S_0}$ is determined as a function of time. This curve is then fit to extract the distance information. Most frequently this data takes the form of a sigmoidal curve, but in the case of dephasing by ^{2}H, the T_1 relaxation time of the deuterium is short enough that this is not generally seen.[97] In an investigation of peptide insertion into the membrane, it was found that the data was well fit by an exponential of the form $A(1 - e^{-\gamma t})$, where A is the fraction of molecules with effective carbon-deuterium coupling $d = \frac{3\gamma}{2}$.[97] The distance, r, is then calculated as $\left[\frac{4642 Hz}{3\gamma/2}\right]^{\frac{1}{3}}$.

To verify that the pulse sequence would result in the desired dephasing, a sample of methionine-1-^{13}C-methyl-$^2H_3$ was used, as was done by Luthra *et al.*[98] The structure of this compound is shown in Figure 5.4. Since we do not need to quantify distance as they have done, and simply wanted to verify the relative degree of dephasing, the sample used was not recrystallized, and was simply lyophilized after dilution with unlabeled methionine so the sample contained just 10% labeled material to minimize intermolecular interactions. The clear dephasing is sufficient to confirm the method. The data, plotted in Figure 5.5, does appear to show exponential behavior, but the fitting according to the method employed by Weliky *et al.* yields a effective ^{13}C-^{2}H coupling of 135 Hz, and distance of 4.1 Å. This is shorter than the 5.98 Å one would expect based on the crystal structure.[98] The shorter distance could be cause by greater disorder in the methionine side chain compared to a neatly ordered crystal structure.

5.2 Methods

5.2.1 Materials

L-methionine (1-^{13}C; methyl-d_3) for control experiment was purchased from Cambridge Isotope Laboratories (Andover, MA). L-Leucine ($^{13}C_6$) and decanoic-10,10,10-d_3 acid were purchased from Cambridge Isotope Laboratories (Andover, MA). Decanoic-2,2-d_2 acid was pur-

chased from C/D/N Isotopes Inc. (Quebec, CA); deuterium depleted water from Sigma-Aldrich.

5.2.2 Sample Preparation

Sample preparation was performed by Roy Black; the protocol is reported here for reference. (Note: the masses used here refer to methyl-deuterated decanoic acid (MW 175 g/mol) and uniformly-$^{13}C_6$ labeled leucine (MW 137 g/mol) and these were adjusted to reflect the labeling scheme in use.) Decanoic acid (77.7 mg) was heated and vortexed in 1 M NaOH/deuterium-depleted water (0.524 mL). To this mixture, deuterium-depleted water (2.323 mL) was added and vortexed resulting in a 161 mM decanoic acid solution. Additional deuterium-depleted water (3.444 mL) was added and vortexed, diluting the solution to 72 mM. The solution was then titrated to pH 7.5 using HCl solutions made with deuterium depleted water (approximately 77 µL 6 M HCl, 59 µL 1 M HCl). 3mL of this solution was then added to ^{13}C leucine (4.1 mg) to make a vesicle sample that is 72 mM decanoic acid, and 10 mM leucine.

The sample was then lyophilized to a powder for NMR studies.

5.2.3 $^{13}C\{^2H\}$ REDOR

Experiments were done with a 11.74 T Bruker Avance III 500 MHz, narrow-bore spectrometer using a Bruker TriGamma probe tuned for ^{1}H-^{13}C-^{2}H triple resonance. Pulse program used is depicted in Figure 5.3. Samples were spun at 10kHz MAS frequency, S0 and S1 were collected for dephasing times of 0.8, 3.2, 5.6, 8.0 and 10.4 ms and required 1024, 2048, 2048, 2048 and 4096 scans, respectively. The contact time used in the CP was 1.5 ms, during this time the ^{1}H power was ramped from 70% to 100%. Field strengths were: 83 kHz ^{1}H $\frac{\pi}{2}$ pulse, 56 kHz ^{13}C π pulses, and 66 kHz ^{2}H π pulses. During dephasing and decoupling 100 kHz SPINAL-64 decoupling was applied on the ^{1}H channel.[99] Data was processed with 20 Hz Gaussian line broadening and baseline correction. Chemical shift referencing was done externally using adamantane. The methylene ^{13}C shift was set to 38.5 ppm.

5.3 Results

To examine the relative location of leucine in the bilayer, selectively labelled decanoic acid was used. Specifically, for the $^{13}C\{^{2}H\}$ REDOR, the dephasing of ^{13}CO in leucine was recorded for two different samples of decanoic acid, shown in Figure 5.6. Decanoic-2,2-d_2 acid and decanoic-10,10,10-d_3 acid were selected to clearly distinguish between association of leucine near the head group and leucine in the center of the bilayer, respectively.

Figures 5.8 and 5.9 show the carbonyl region of the REDOR S_0 and S_1, for decanoic-10,10,10-d_3 acid and decanoic-2,2-d_2 acid respectively, with 0.8 ms, 3 .2 ms, 5.6 ms, 8.0 ms and 10.4 ms dipolar recoupling periods. There are two peaks for the leucine ^{13}CO, at 177.6 and 176.4 ppm, as reported in the literature.[100] These could potentially reflect two different crystal structure of leucine. Before considering the behavior of the leucine further, a comment on the other contribution to the spectra. The peak at 182 ppm is from the natural abundance ^{13}CO in the decanoic acid. This assignment is reinforced by the rapid dephasing of the peak with the decanoic-2,2-d_2 acid sample, as the carbonyl adjacent to the CD_2 group. Note that not all of the decanoic acid will be incorporated into the vesicles, and this second population is reflected by the presence of a second peak at 184 ppm.

Now, focusing on just the signal from the leucine ^{13}CO, presented in Figures 5.11 and 5.10 for the 3.2 ms, 5.6 ms, 8.0 ms and 10.4 ms dipolar recoupling periods. The leucine ^{13}CO signal for both samples is broad, reflecting the contributions of the two leucine populations, as reported in the literature. The decanoic-10,10,10-d_3 acid does not seem to be dephasing the signal at all, indicating that the leucine is not embedded in the middle of the bilayer. The decanoic-2,2-d_2 acid sample does give dephasing of the leucine ^{13}CO, which is consistent with leucine interacting primarily with the head group. However, the broad leucine peak does not uniformly dephase. It appears that the two peaks represent leucine molecules in two different environments, one where the leucine is interacting with the bilayer and one where it is not. The peak at 177 ppm corresponds to leucine interacting with the bilayer. Now comparing the S_0 spectra for the two samples, shown in Figure 5.12, the contribution

of the peak at 177 ppm is not as significant in the S_0 in the decanoic-10,10,10-d_3 acid sample when compared with the decanoic-2,2-d_2 acid sample. The increased peak intensity in the decanoic-2,2-d_2 acid sample can be attributed to an increase in the T_2 relaxation time of the leucine ^{13}CO when the methylene near the head group is deuterated. The strong dipolar coupling of the protons on the decanoic acid to the leucine ^{13}CO gives an apparent decrease in the T_2, which further supports the hypothesis that the leucine associates near the surface of the bilayer.

5.4 Conclusions

In summary, the $^{13}C\{^2H\}$ REDOR dephasing indicates that leucine associates with the polar head group of the decanoic acid and is not present in the hydrophobic tail region. Moreover, the interaction is strong enough between the protons near the head group and the carbonyl of the leucine that deuteration of the decanoic acid leads to an increase in the T_2 of the leucine carbonyl.

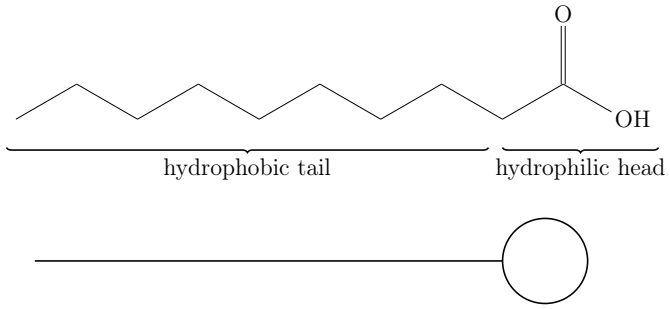

Figure 5.1: Chemical structure of decanoic acid with schematic ball-and-stick model for reference. Decanoic has a small carboxylate hydrophilic headgroup (ball in ball-and-stick model) and a ten-carbon saturated hydrophobic tail (stick in ball-and-stick model).

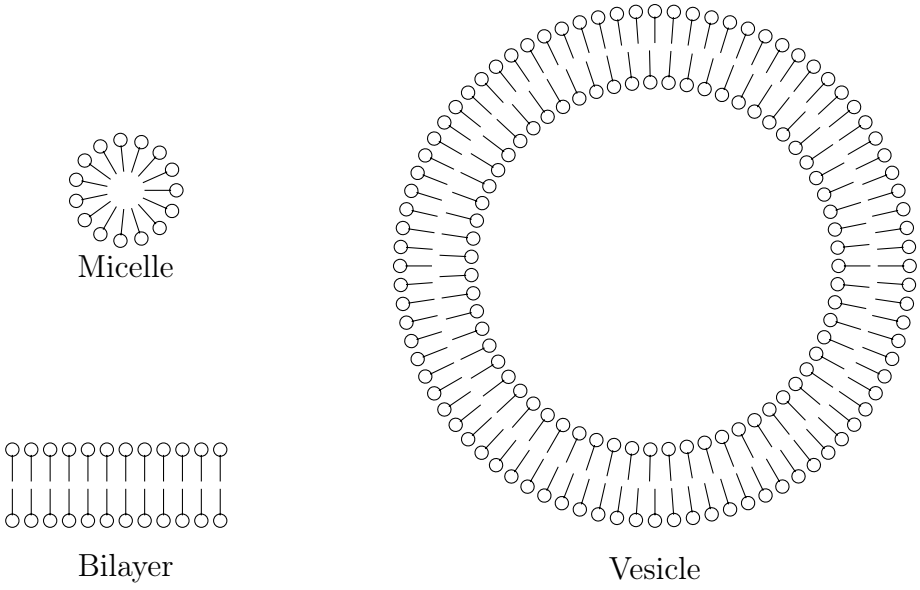

Figure 5.2: Fatty acids self-assemble in aqueous solutions to form micelles and vesicles. Micelles have a single layer of fatty acids, while vesicles have two layers of fatty acids, called a bilayer.

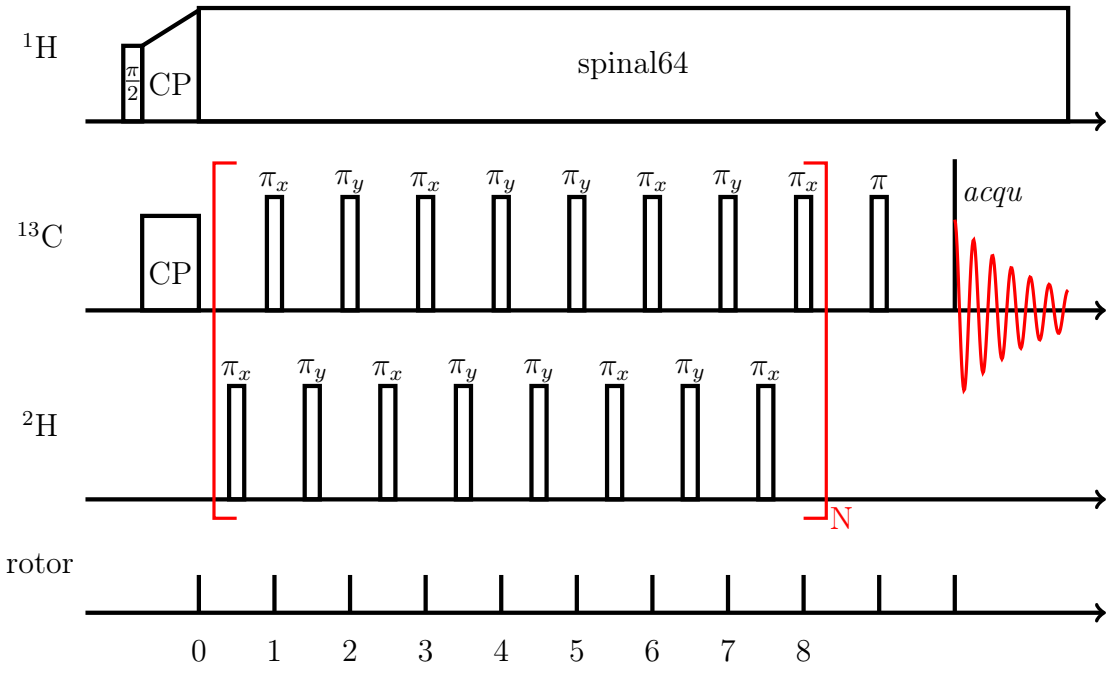

Figure 5.3: ^{13}C{^{2}H} REDOR Pulse Program: The ^{13}C and ^{2}H π pulses during the recoupling period are phase cycled according to the xy-8 scheme to minimize off-resonance effects. The CP and final π pulse on the ^{13}C channel are phase cycled as: $xxyy\ \bar{x}\bar{x}\bar{y}\bar{y}\ \bar{x}\bar{x}\bar{y}\bar{y}\ xxyy$. The ^{1}H $\frac{\pi}{2}$ pulse phases cycles as $y\bar{y}$, and the CP done with phase x. Receiver is phase cycled as: $x\bar{x}y\bar{y}\ \bar{x}x\bar{y}y\ \bar{x}x\bar{y}y\ x\bar{x}y\bar{y}$.

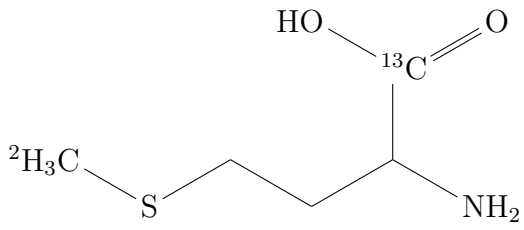

Figure 5.4: Chemical structure of ^{13}C/^{2}H labeled methionine used in the REDOR control.

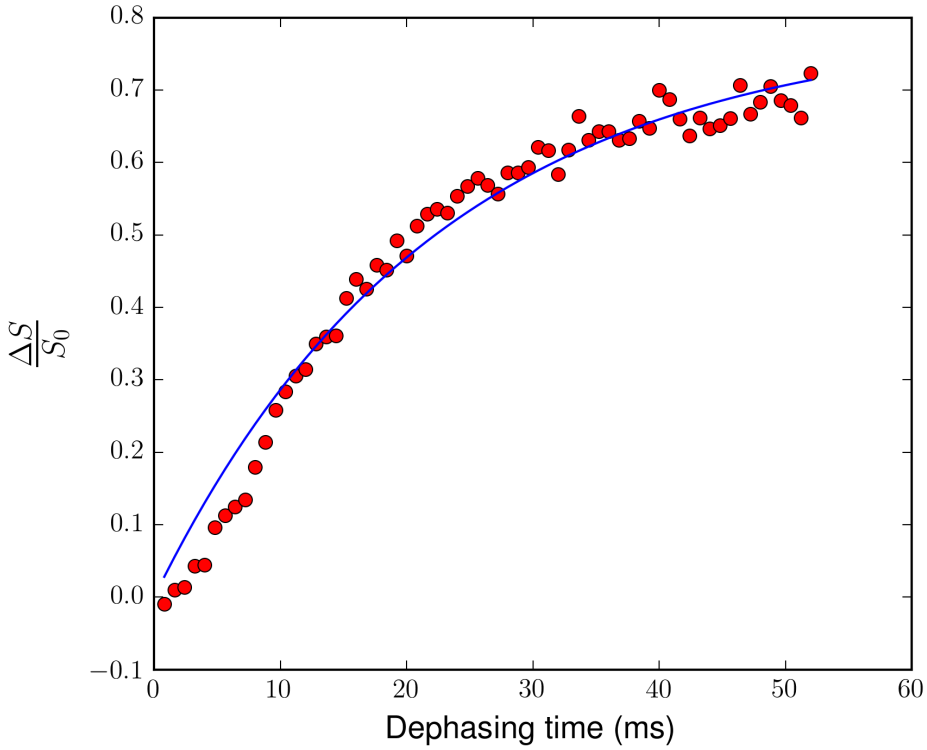

Figure 5.5: ^{13}C{^{2}H} REDOR dephasing curve for methionine. The blue overlay corresponds to a best fit of $A(1 - e^{-\gamma t})$, with A = 0.7896, γ=45.04Hz. Using the method of Weliky *et al.*, where $r = [\frac{4642Hz}{3\gamma/2}]^{\frac{1}{3}}$, this corresponds to a distance of 4.1Å.

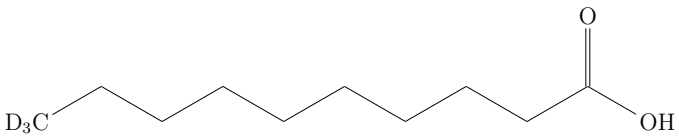

decanoic-10,10,10-d_3 acid

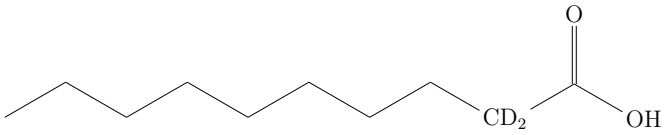

decanoic-2,2-d_2 acid

Figure 5.6: Chemical structures of the two labeled decanoic acid samples used for the $^{13}C\{^{2}H\}$ REDOR experiments.

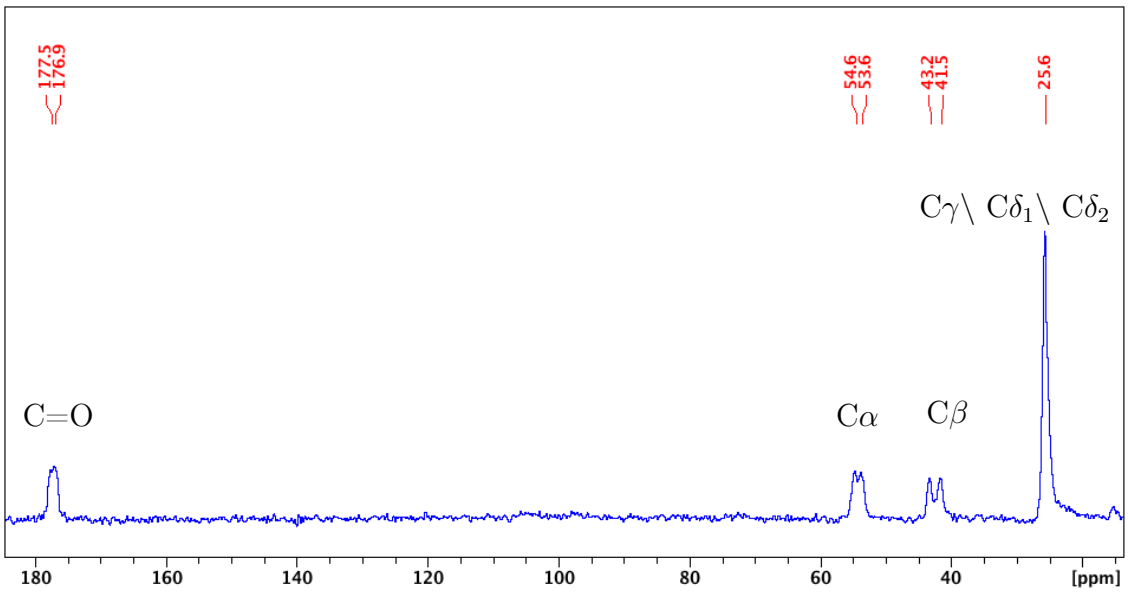

Figure 5.7: Full ^{13}C CP-MAS spectrum for uniformly-$^{13}C_6$ labeled leucine.

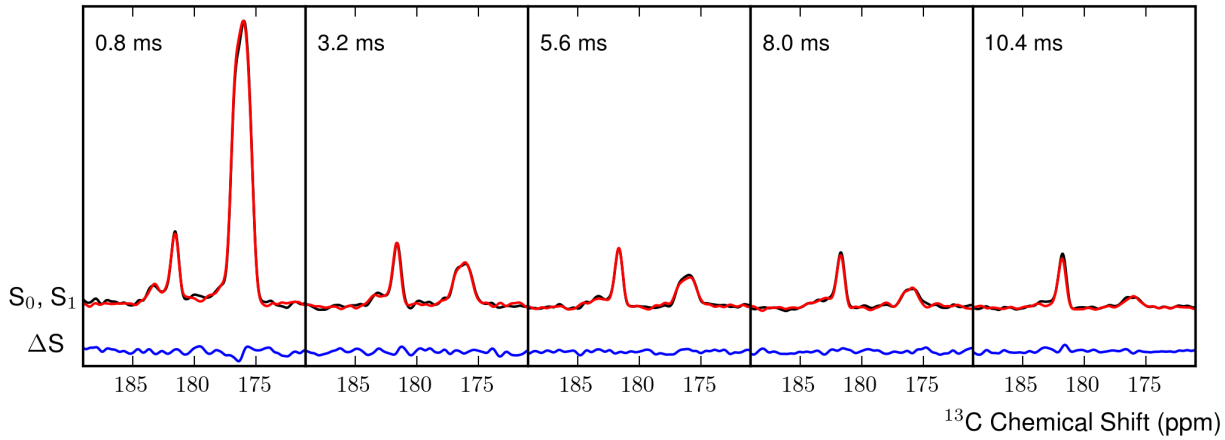

Figure 5.8: Dephasing by Decanoic-10,10,10-d_3 acid: At 5 dephasing times, shown are the S_0 in black, overlaid with the S_1 in red, S_0-S_1 is show in blue, with a vertical offset for clarity. Tracking the leucine carbonyl peaks when dephasing with the decanoic-10,10,10-d_3 acid.

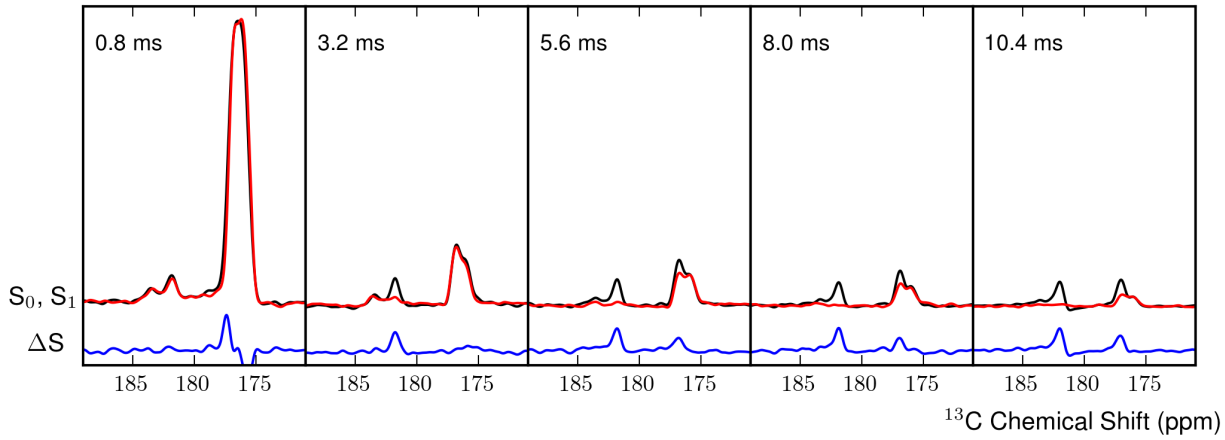

Figure 5.9: Dephasing by Decanoic-2,2-d_2 acid: At 5 dephasing times, shown are the S_0 in black, overlaid with the S_1 in red, S_0-S_1 is show in blue, with a vertical offset for clarity. Tracking the leucine carbonyl peaks when dephasing with the decanoic-2,2-d_2 acid .

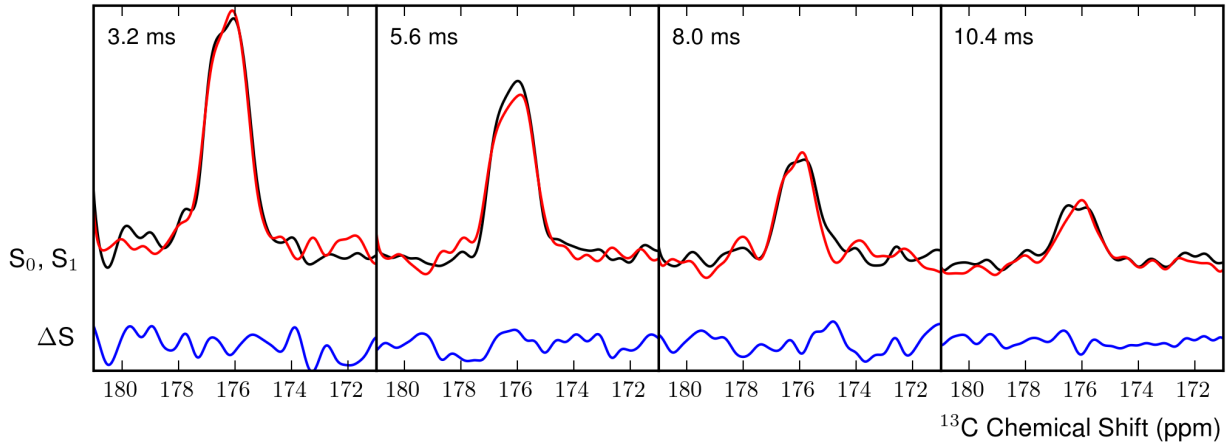

Figure 5.10: Dephasing by Decanoic-10,10,10-d_3 acid, Zoomed: At the last 4 dephasing times, shown are the S_0 in black, overlaid with the S_1 in red, S_0-S_1 is show in blue, with a vertical offset for clarity. Note that there is no change and the difference of the spectra is largely noise when dephasing with the decanoic-10,10,10-d_3 acid.

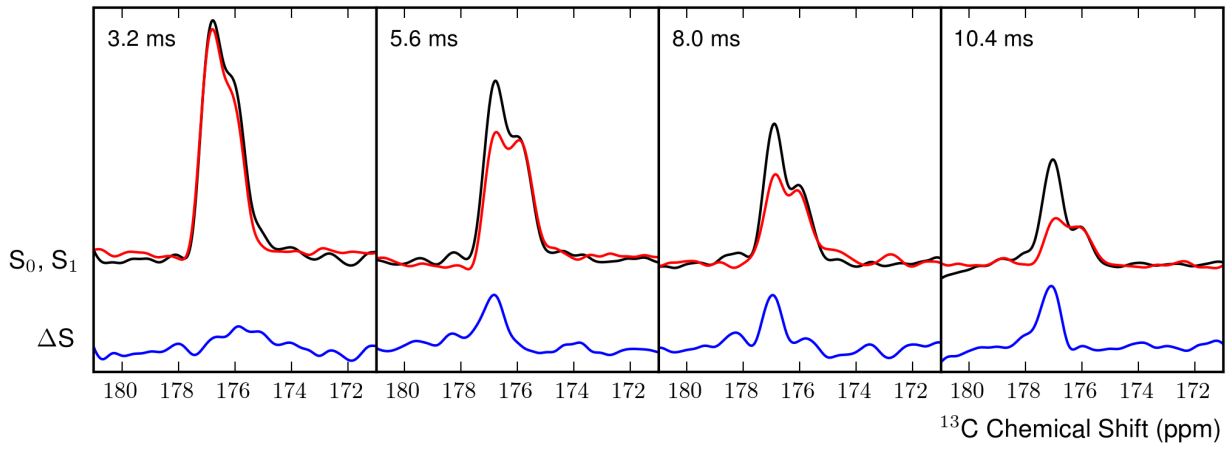

Figure 5.11: Dephasing by Decanoic-2,2-d_2 acid, Zoomed: At the last 4 dephasing times, shown are the S_0 in black, overlaid with the S_1 in red, S_0-S_1 is show in blue, with a vertical offset for clarity. Note the growing difference shown when dephasing with the decanoic-2,2-d_2 acid .

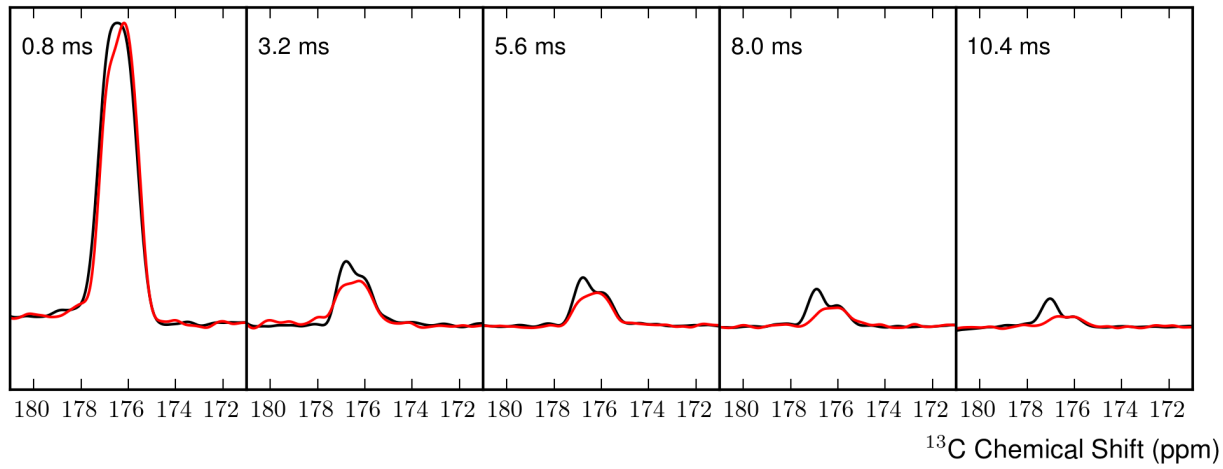

Figure 5.12: REDOR S_0 Comparison: S_0 for sample with decanoic-2,2-d_2 acid in black, and S_0 for sample with decanoic-10,10,10-d_3 acid in red. Note that peak at 177 ppm is relaxing faster in the sample with decanoic-10,10,10-d_3.

5.5 Supplemental: Static ^2H ssNMR

As previously discussed in Chapters 2 and 3, the analysis and careful fitting of ^{2}H NMR line shapes of leucine methyl groups can be used to learn about the local dynamics of amino acid side chains. In lipid systems, ^{2}H NMR line shape analysis is generally a little more straightforward.[51,101–103] Frequently, the alkyl chains of phospholipids are perdeuterated, resulting in spectra that are the convolution of many overlapping powder patterns. The width of the powder pattern is inversely related to the degree of mobility – that is, the more mobile a site is, the narrower the Pake doublet observed.[104,105] In many cases, it is possible to resolve the horns of each Pake doublet and mobilities can be determined based on the assumption that the broadest contributions are from deuterons nearest the head group (the least mobile) and the narrowest are those closest to the end of the tail (the most mobile).[104,105] Even if individual contributions are not resolvable, the system can be investigated by observing changes in the overall peak manifold under various conditions, i.e. different lipid compositions or cholesterol concentrations.

Lipid bilayers are sensitive to the introduction of material to the head group region of the bilayer. Even the addition of a small molecule, such as ethanol, is sufficient to interfere with the packing of the head groups.[103] Interestingly, this changes not only the mobility of the deuterons near the head group, but also those farther down the alkyl chain, indicating a shift in packing. Material incorporated exclusively in the hydrophobic tail region of the material results in no change in the dynamics in the tails.[103] This results from the fact that the alkyl chains are very mobile at the ends and easily repack around small chemicals. Leucine could pack in decanoic acid in a similar fashion, with the polar amine and carboxylic acid groups associating with the carboxylic acid groups of the decanoic acid, and the hydrophobic side chain in the hydrophobic interior of the fatty acid bilayer. A potential obstacle with this system is that fatty acid vesicles do not possess the same head group structure as phospholipids, and are not thought to pack as tightly at the polar interface. This means that leucine could be incorporated without as much disruption to the packing, and that

changes in the line shape can be minimal.

5.5.1 Methods

Sample Preparation

Sample preparation was performed as for the REDOR samples. Hydration of the samples for the static ^{2}H NMR was performed using hydration chambers with saturated salt solutions in deuterium depleted water to control the degree of hydration.

Static ^{2}H NMR

Deuterium line shapes were acquired at a 9.4T field (61.38 MHz deuterium Larmor frequency) using a Varian T3MAS probe and a homebuilt spectrometer. Quadrupolar echo $\left(\left(\frac{\pi}{2}\right)_x - \tau_1 - \left(\frac{\pi}{2}\right)_y - \tau_2 - acqu\right)$ experiments used eight-step phase cycling to suppress unwanted coherence pathways,[30,31] with a $\frac{\pi}{2}$ pulse time of 3.3µs , an echo delay of 40µs, and a recycle delay of 0.35s. Line shapes were processed by left-shifting to the echo maximum prior to Fourier transform, followed by 1 kHz line broadening, zero-filling from 4096 to 8192 points, and phase correction.

5.5.2 Results

Deuterium line shapes were collected for four different samples of decanoic acid vesicles made using uniformly deuterated d_{19}-decanoic acid. The four samples were: decanoic acid vesicles with leucine added, then three controls. The first was the decanoic acid vesicles at pH 7.54 without leucine. Glycine does not stabilize the vesicles, so this sample was run to see if the induced changes in the line shape were uniquely due to a stabilizing interaction of leucine, or if changes were present for both samples. The last control was a solution raised to a pH of 12, where vesicle formation does not occur.

Initially, data was collected for samples in the solution conditions, in which vesicles are known to form. However, the sample was too mobile in solution, and resulted in spectra dom-

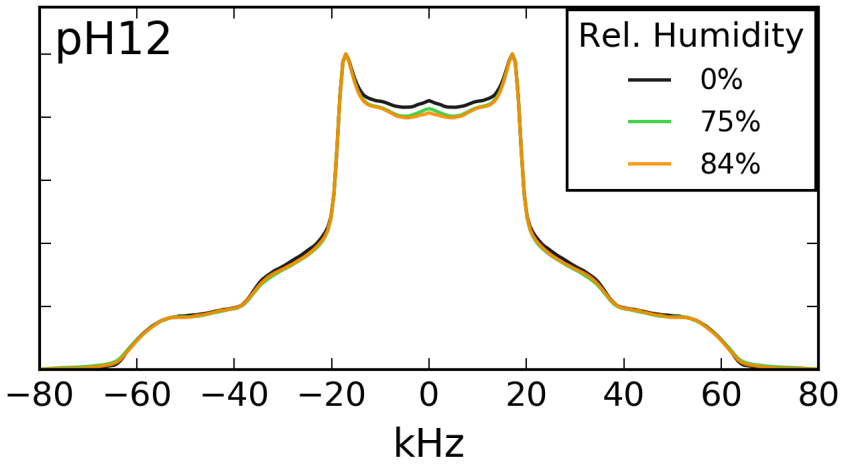

Figure 5.13: Deuterium line shapes for decanoic acid lyophilized from a solution at pH 12, where vesicles are known not to form.

inated by an isotropically averaged peak. To circumvent this, the samples were lyophilized. Samples were then examined at three different levels of hydration, both to better match experimental conditions and since increased levels of hydration are known to better distinguish degrees of mobility. It is assumed that the structure of the decanoic acid is not significantly altered by lyophilization. This is supported by the dramatic difference in the spectra for the pH 12 sample, shown in Figure 5.13, where the vesicles are known not to form. In contrast to the series of spectra shown in Figure 5.14, the high pH sample's spectrum is dominated by a broad Pake doublet, indicating a very different environment of the akyl chains.

Figure 5.14 shows the amino acid-free control, glycine and leucine spectra grouped by hydration level. Aside from differences in the isotropic water peak in the center of the spectrum, there is not much of a dramatic difference between the three sets of spectra. At the highest level of hydration, it appears that the decanoic acid with leucine added has a slightly broader spectrum still, but it is not a large change.

Organizing the spectra by amino acid added allows tracking of how hydration altered the mobility in each sample. In Figure 5.15, all three sets of spectra show an increase of central

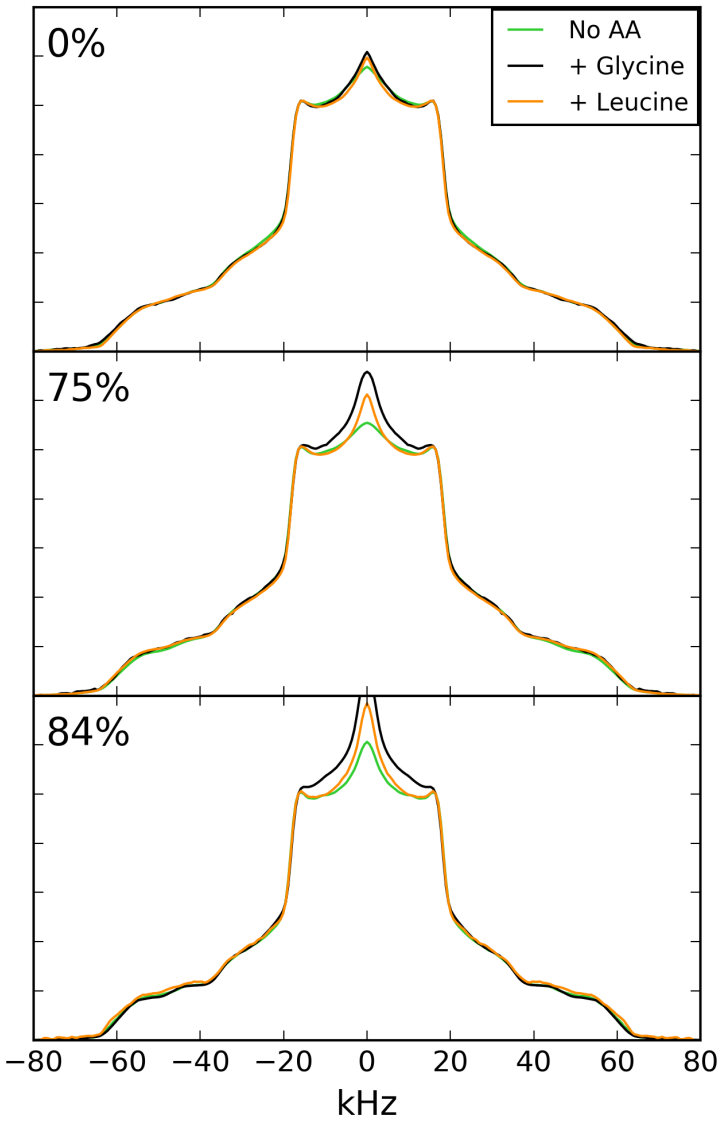

Figure 5.14: Deuterium line shapes of $d_{19}-$decanoic acid with no amino acid, leucine and glycine added; organized by hydration level. Percent hydration refers to the relative humidity of the hydration chamber used for sample hydration. All samples were titrated to a pH of 7.55.

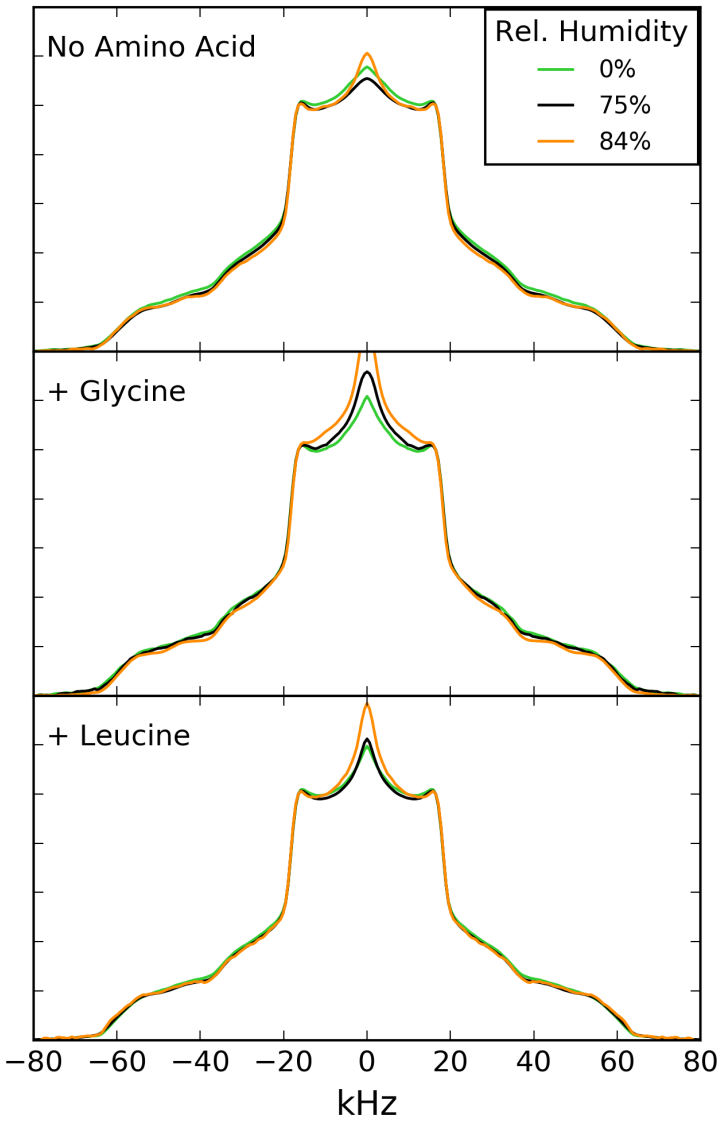

Figure 5.15: Deuterium line shapes organized by sample.

intensity with increased hydration, but this is simply contribution from residual HDO in the deuterium depleted water used in the hydration process. Examining the shoulder regions of these spectra, hydration seems to slightly narrow the line shape for the amino acid-free and glycine added control samples, while no change is observed for the leucine sample. This trend is by no means conclusive, due to the minor nature of the line shape changes. The lack of a significant difference means that no association is shown from this data. As previously stated, this does not bar the possibility of an associative effect since the fatty acid packing is looser and more easily interrupted than phospholipids, which is why the REDOR technique was employed.

BIBLIOGRAPHY

[1] N Kröger, R Deutzmann, and M Sumper. Polycationic peptides from diatom biosilica that direct silica nanosphere formation. *Science*, 286(5442):1129–1132, Nov 1999.

[2] N Kröger, R Deutzmann, C Bergsdorf, and M Sumper. Species-specific polyamines from diatoms control silica morphology. *Proc Natl Acad Sci U S A*, 97(26):14133–14138, Dec 2000.

[3] Pascal Lopez, Clementine Gautier, Jacques Livage, and Thibaud Coradin. Mimicking Biogenic Silica Nanostructures Formation. *Current Nanoscience*, 1(1):73–83, Jan 2005.

[4] Francisco Rodríguez, Diana D Glawe, Rajesh R Naik, Kevin P Hallinan, and Morley O Stone. Study of the chemical and physical influences upon in vitro peptide-mediated silica formation. *Biomacromolecules*, 5(2):261–265, Mar-Apr 2004.

[5] Marc R. Knecht and David W. Wright. Functional analysis of the biomimetic silica precipitating activity of the R5 peptide from Cylindrotheca fusiformis. *Chem. Commun.*, pages 3038–3039, 2003.

[6] David J. Belton, Siddharth V. Patwardhan, and Carole C. Perry. Spermine, spermidine and their analogues generate tailored silicas. *J. Mater. Chem.*, 15:4629–4638, 2005.

[7] Nils Kröger, Sonja Lorenz, Eike Brunner, and Manfred Sumper. Self-assembly of highly phosphorylated silaffins and their function in biosilica morphogenesis. *Science*, 298(5593):584–586, Oct 2002.

[8] Manfred Sumper, Sonja Lorenz, and Eike Brunner. Biomimetic control of size in the polyamine-directed formation of silica nanospheres. *Angewandte Chemie International Edition*, 42(42):5192–5195, 2003.

[9] Manfred Sumper and Nils Kröger. Silica formation in diatoms: the function of long-chain polyamines and silaffins. *J. Mater. Chem.*, 14:2059–2065, 2004.

[10] Igor Pamirsky and Kirill Golokhvast. Silaffins of Diatoms: From Applied Biotechnology to Biomedicine. *Marine Drugs*, 11(9):3155–3167, Aug 2013.

[11] Ariel C. Zane, Christian Michelet, Adrienne Roehrich, Prashant S. Emani, and Gary P. Drobny. Silica Morphogenesis by Lysine-Leucine Peptides with Hydrophobic Periodicity. *Langmuir*, 30(24):7152–7161, Jun 2014.

[12] Ariel C. Zane. *Solid State NMR Characterization of Biosilicification Peptides*. PhD thesis, University of Washington, 2013.

[13] Adrienne Roehrich and Gary Drobny. Solid-State NMR Studies of Biomineralization Peptides and Proteins. *Accounts of Chemical Research*, 46(9):2136–2144, Sep 2013.

[14] Carolin C. Lechner and Christian F. W. Becker. A sequence-function analysis of the silica precipitating silaffin R5 peptide. *Journal of Peptide Science*, 20(2):152–158, 2014.

[15] W. F. DeGrado and J. D. Lear. Induction of Peptide Conformation at Apolar Water Interfaces. 1. A Study with Model Peptides of Defined Hydrophobic Periodicity. *Journal of the American Chemical Society*, 107(25):7684–7689, 1985.

[16] W F DeGrado, Z R Wasserman, and J D Lear. Protein Design, A Minimalist Approach. *Science*, 243(4891):622–628, Feb 1989.

[17] P. V. Bower, E. A. Louie, J. R. Long, P. S. Stayton, and G. P. Drobny. Solid-State NMR Structural Studies of Peptides Immobilized on Gold Nanoparticles. *Langmuir*, 21(7):3002–3007, 2005. PMID: 15779977.

[18] Nicholas F. Breen, Tobias Weidner, Kun Li, David G. Castner, and Gary P. Drobny. A Solid-State Deuterium NMR and Sum-Frequency Generation Study of the Side-Chain Dynamics of Peptides Adsorbed onto Surfaces. *Journal of the American Chemical Society*, 131(40):14148–14149, 2009.

[19] Nicholas F. Breen, Kun Li, Gregory L. Olsen, and Gary P. Drobny. Deuterium Magic Angle Spinning NMR Used To Study the Dynamics of Peptides Adsorbed onto Polystyrene and Functionalized Polystyrene Surfaces. *The Journal of Physical Chemistry B*, 115(30):9452–9460, 2011. PMID: 21650191.

[20] Joanna R. Long, Nathan Oyler, Gary P. Drobny, and Patrick S. Stayton. Assembly of α-helical Peptide Coatings on Hydrophobic Surfaces. *Journal of the American Chemical Society*, 124(22):6297–6303, 2002. PMID: 12033857.

[21] Tobias Weidner, Nicholas F. Breen, Kun Li, Gary P. Drobny, and David G. Castner. Sum frequency generation and solid-state NMR study of the structure, orientation, and dynamics of polystyrene-adsorbed peptides. *Proceedings of the National Academy of Sciences*, 107(30):13288–13293, 2010.

[22] Ozzy Mermut, Diana C. Phillips, Roger L. York, Keith R. McCrea, Robert S. Ward, and Gabor A. Somorjai. In Situ Adsorption Studies of a 14-Amino Acid Leucine-Lysine Peptide onto Hydrophobic Polystyrene and Hydrophilic Silica Surfaces Using Quartz Crystal Microbalance, Atomic Force Microscopy, and Sum Frequency Generation Vibrational Spectroscopy. *Journal of the American Chemical Society*, 128(11):3598–3607, 2006. PMID: 16536533.

[23] Diana C. Phillips, Roger L. York, Ozzy Mermut, Keith R. McCrea, Robert S. Ward, and Gabor A. Somorjai. Side Chain, Chain Length, and Sequence Effects on Amphiphilic Peptide Adsorption at Hydrophobic and Hydrophilic Surfaces Studied by Sum-Frequency Generation Vibrational Spectroscopy and Quartz Crystal Microbalance. *The Journal of Physical Chemistry C*, 111(1):255–261, 2007.

[24] Roger L. York, William K. Browne, Phillip L. Geissler, and Gabor A. Somorjai. Peptides Adsorbed on Hydrophobic Surfaces—A Sum Frequency Generation Vibrational Spectroscopy and Modeling Study. *Israel Journal of Chemistry*, 47(1):51–58, 2007.

[25] Eric F Pettersen, Thomas D Goddard, Conrad C Huang, Gregory S Couch, Daniel M Greenblatt, Elaine C Meng, and Thomas E Ferrin. UCSF Chimera–a visualization system for exploratory research and analysis. *J Comput Chem*, 25(13):1605–1612, Oct 2004.

[26] Yang Shen and Ad Bax. Protein backbone and sidechain torsion angles predicted from NMR chemical shifts using artificial neural networks. *Journal of Biomolecular NMR*, 56(3):227–241, 2013.

[27] Joe E. Baio, Ariel Zane, Vance Jaeger, Adrienne M. Roehrich, Helmut Lutz, Jim Pfaendtner, Gary P. Drobny, and Tobias Weidner. Diatom Mimics: Directing the Formation of Biosilica Nanoparticles by Controlled Folding of Lysine-Leucine Peptides. *Journal of the American Chemical Society*, 136(43):15134–15137, 2014. PMID: 25285787.

[28] Todd M. Alam and Gary P. Drobny. Solid-state NMR studies of DNA structure and dynamics. *Chemical Reviews*, 91(7):1545–1590, 1991.

[29] J. H. Davis. *Deuterium nuclear magnetic resonance spectroscopy in partially ordered systems*, chapter 3. Elsevier, 1991.

[30] Melinda J. Duer, editor. *Solid-State NMR Spectroscopy: principles and applications*. Blackwell Science Ltd, 2002.

[31] Robert Tycko, editor. *Nuclear Magnetic Resonance Probes of Molecular Dynamics*. Kluwer Academic Publishers, 1994.

[32] H. W Spiess and H Sillescu. Solid echoes in the slow-motion region. *Journal of Magnetic Resonance (1969)*, 42(3):381–389, Mar 1981.

[33] Jørgen H. Kristensen, Henrik Bildsøe, Hans J. Jakobsen, and Niels Chr. Nielsen. Theory and simulations of molecular dynamics in ^{2}H MAS NMR. *Journal of Magnetic Resonance*, 100(2):437 – 443, 1992.

[34] Robert L. Vold and Gina L. Hoatson. Effects of jump dynamics on solid state nuclear magnetic resonance line shapes and spin relaxation times. *Journal of Magnetic Resonance*, 198(1):57 – 72, 2009.

[35] R. J. Wittebort, E. T. Olejniczak, and R. G. Griffin. Analysis of deuterium nuclear magnetic resonance line shapes in anisotropic media. *The Journal of Chemical Physics*, 86(10):5411–5420, 1987.

[36] M.J. Duer and M.H. Levitt. Time-domain calculation of chemical exchange effects in the NMR spectra of rotating solids. *Solid State Nuclear Magnetic Resonance*, 1(4):211–215, Nov 1992.

[37] Dr. Phillip M. Feldman. Eight Advantages of Python Over Matlab, `http://phillipmfeldman.org/Python/Advantages_of_Python_Over_Matlab.html`.

[38] Hoyt Koepke. 10 Reasons Python Rocks for Research (And a Few Reasons it Doesn't), `http://www.stat.washington.edu/~hoytak/blog/whypython.html`.

[39] Asher Schmidt, Steven O. Smith, Daniel P. Raleigh, James E. Roberts, Robert G. Griffin, and Shimon Vega. Chemical exchange effects in the NMR spectra of rotating solids. *The Journal of Chemical Physics*, 85(8):4248, 1986.

[40] O Weintraub and S Vega. Dynamic ^{2}H nuclear magnetic resonance of rotating solids. *Solid State Nuclear Magnetic Resonance*, 4(6):341–351, Aug 1995.

[41] J H Kristensen, G L Hoatson, and Robert L Vold. Effects of restricted rotational diffusion on ^{2}H magic angle spinning nuclear magnetic resonance spectra. *The Journal of Chemical Physics*, 110(9):4533, 1999.

[42] Michael J. Thrippleton, Marica Cutajar, and Stephen Wimperis. Magic angle spinning (MAS) NMR linewidths in the presence of solid-state dynamics. *Chemical Physics Letters*, 452(4-6):233–238, Feb 2008.

[43] Kun Li. *Use Deuterium Solid State NMR Simulations to Study Dynamics of Peptides Adsorbed onto Inorganic Surfaces*. PhD thesis, University of Washington, 2012.

[44] Vera B. Cheng, Henry H. Suzukawa, and Max Wolfsberg. Investigations of a nonrandom numerical method for multidimensional integration. *The Journal of Chemical Physics*, 59(8):3992–3999, 1973.

[45] Harold Conroy. Molecular Schrödinger Equation. VIII. A New Method for the Evaluation of Multidimensional Integrals. *The Journal of Chemical Physics*, 47(12):5307–5318, 1967.

[46] S. K. Zaremba. Good lattice points, discrepancy, and numerical integration. *Annali di Matematica Pura ed Applicata*, 73(1):293–317, Dec 1966.

[47] Malcolm Levitt. Orientations for Powder Averaging, `http://www.southampton.ac.uk/~mhl/resources/Orientations/index.html`.

[48] Wei Liu, Evan Crocker, Stefan N Constantinescu, and Steven O Smith. Helix packing and orientation in the transmembrane dimer of gp55-P of the spleen focus forming virus. *Biophys J*, 89(2):1194–1202, Aug 2005.

[49] Kathleen P. Howard, Wei Liu, Evan Crocker, Vikas Nanda, James Lear, William F. Degrado, and Steven O. Smith. Rotational orientation of monomers within a designed homo-oligomer transmembrane helical bundle. *Protein Science*, 14(4):1019–1024, 2005.

[50] Weiwen Ying, Scott E. Irvine, Richard A. Beekman, David J. Siminovitch, and Steven O. Smith. Deuterium NMR Reveals Helix Packing Interactions in Phospholamban. *Journal of the American Chemical Society*, 122(45):11125–11128, 2000.

[51] Joanna R. Long, Frank D. Mills, Omjoy K. Ganesh, Vijay C. Antharam, and R. Suzanne Farver. Partitioning, dynamics, and orientation of lung surfactant peptide {KL4} in phospholipid bilayers. *Biochimica et Biophysica Acta (BBA) - Biomembranes*, 1798(2):216 – 222, 2010. Membrane Protein Dynamics by NMR: Correlation of Structure and Function.

[52] Eva Meirovitch, Zhichun Liang, and Jack H Freed. Protein dynamics in the solid state from ^{2}H NMR line shape analysis: a consistent perspective. *J Phys Chem B*, 119(7):2857–2868, Feb 2015.

[53] Eva Meirovitch, Zhichun Liang, and Jack H Freed. Protein Dynamics in the Solid State from ^{2}H NMR Line Shape Analysis. II. MOMD Applied to C–D and C–CD_3 Probes. *The Journal of Physical Chemistry B*, 119(44):14022–14032, 2015.

[54] L W Jelinski, C E Sullivan, L S Batchelder, and D A Torchia. Deuterium nuclear magnetic resonance of specifically labeled native collagen. investigation of protein molecular dynamics using the quadrupolar echo technique. *Biophys J*, 32(1):515–529, Oct 1980.

[55] L S Batchelder, C E Sullivan, L W Jelinski, and D A Torchia. Characterization of leucine side-chain reorientation in collagen-fibrils by solid-state ^{2}H NMR. *Proceedings of the National Academy of Sciences*, 79(2):386–389, 1982.

[56] Liliya Vugmeyster, Dmitry Ostrovsky, Joseph J. Ford, Sarah D. Burton, Andrew S. Lipton, Gina L. Hoatson, and Robert L. Vold. Probing the Dynamics of a Protein Hydrophobic Core by Deuteron Solid-State Nuclear Magnetic Resonance Spectroscopy. *Journal of the American Chemical Society*, 131(38):13651–13658, 2009.

[57] Liliya Vugmeyster, Dmitry Ostrovsky, Mark Moses, Joseph J. Ford, Andrew S. Lipton, Gina L. Hoatson, and Robert L. Vold. Comparative Dynamics of Leucine Methyl Groups in FMOC-Leucine and in a Protein Hydrophobic Core Probed by Solid-State Deuteron Nuclear Magnetic Resonance over 7-324 K Temperature Range. *The Journal of Physical Chemistry B*, 114(48):15799–15807, 2010.

[58] Liliya Vugmeyster, Dmitry Ostrovsky, Joseph J. Ford, and Andrew S. Lipton. Freezing of Dynamics of a Methyl Group in a Protein Hydrophobic Core at Cryogenic Temperatures by Deuteron NMR Spectroscopy. *Journal of the American Chemical Society*, 132(12):4038–4039, 2010.

[59] Liliya Vugmeyster, Dmitry Ostrovsky, Anastasia Khadjinova, Jeremy Ellden, Gina L. Hoatson, and Robert L. Vold. Slow Motions in the Hydrophobic Core of Chicken Villin Headpiece Subdomain and Their Contributions to Configurational Entropy and Heat Capacity from Solid-State Deuteron NMR Measurements. *Biochemistry*, 50(49):10637–10646, 2011.

[60] Liliya Vugmeyster, Dmitry Ostrovsky, Kirsten Penland, Gina L. Hoatson, and Robert L. Vold. Glassy Dynamics of Protein Methyl Groups Revealed by Deuteron NMR. *The Journal of Physical Chemistry B*, 117(4):1051–1061, 2013.

[61] Liliya Vugmeyster, Tien Do, Dmitry Ostrovsky, and Riqianq Fu. Effect of subdomain interactions on methyl group dynamics in the hydrophobic core of villin headpiece protein. *Protein Sci*, 23(2):145–156, Feb 2014.

[62] Shadi Abu-Baker, Jun-Xia Lu, Shidong Chu, Clarke C Brinn, Christopher A Makaroff, and Gary A Lorigan. Side chain and backbone dynamics of phospholamban in phospholipid bilayers utilizing ^{2}H and ^{15}N solid-state NMR spectroscopy. *Biochemistry*, 46(42):11695–11706, 2007.

[63] Shidong Chu, Aaron T. Coey, and Gary A. Lorigan. Solid-state ^{2}H and ^{15}N {NMR} studies of side-chain and backbone dynamics of phospholamban in lipid bilayers: Investigation of the {N27A} mutation. *Biochimica et Biophysica Acta (BBA) - Biomembranes*, 1798(2):210 – 215, 2010. Membrane Protein Dynamics by NMR: Correlation of Structure and Function.

[64] Ethan S. Karp, Elvis K. Tiburu, Shadi Abu-Baker, and Gary A. Lorigan. The structural properties of the transmembrane segment of the integral membrane protein phospholamban utilizing ^{13}C CPMAS, ^{2}H, and {REDOR} solid-state {NMR} spectroscopy. *Biochimica et Biophysica Acta (BBA) - Biomembranes*, 1758(6):772 – 780, 2006.

[65] Elvis K Tiburu, Ethan S Karp, Paresh C Dave, Krishnan Damodaran, and Gary A Lorigan. Investigating the dynamic properties of the transmembrane segment of phospholamban incorporated into phospholipid bilayers utilizing ^{2}H and ^{15}N solid-state NMR spectroscopy. *Biochemistry*, 43(44):13899–13909, 2004.

[66] Abil E. Aliev and Kenneth D. M. Harris. ^{2}H NMR lineshape analysis using automated fitting procedures based on local and quasi-global optimization techniques. *Magnetic Resonance in Chemistry*, 36(11):855–868, 1998.

[67] Kun Li, Prashant S. Emani, Jason Ash, Michael Groves, and Gary P. Drobny. A Study of Phenylalanine Side-Chain Dynamics in Surface-Adsorbed Peptides Using Solid-State Deuterium NMR and Rotamer Library Statistics. *Journal of the American Chemical Society*, 136(32):11402–11411, 2014. PMID: 25054469.

[68] Emile Aarts, Jan Korst, and Wil Michiels. Simulated Annealing. In *Search Methodologies*, number 1999, pages 187–210. Springer US, Boston, MA, 2005.

[69] L. Ingber. Simulated annealing: Practice versus theory. *Mathematical and Computer Modelling*, 18(11):29–57, Dec 1993.

[70] Gunter Dueck and Tobias Scheuer. Threshold accepting: A general purpose optimization algorithm appearing superior to simulated annealing. *Journal of Computational Physics*, 90(1):161–175, Sep 1990.

[71] Tejas P Patalia and G R Kulkarni. Comparative Analysis of Threshold Acceptance Algorithm, Simulated Annealing Algorithm and Genetic Algorithm for Function Optimization. *Global Journal of researches in Engineering Numerical Methods*, 12(1):23–27, 2012.

[72] Kathleen Wood, François-Xavier Gallat, Renee Otten, Auke J. van Heel, Mathilde Lethier, Lambert van Eijck, Martine Moulin, Michael Haertlein, Martin Weik, and

Frans A. A. Mulder. Protein surface and core dynamics show concerted hydration-dependent activation. *Angewandte Chemie International Edition*, 52(2):665–668, 2013.

[73] Maggy Hologne and Jérôme Hirschinger. Molecular dynamics as studied by static-powder and magic-angle spinning ^{2}H NMR. *Solid State Nuclear Magnetic Resonance*, 26(1):1–10, Aug 2004.

[74] Maxim V. Shapovalov and Jr. Dunbrack, Roland L. A smoothed backbone-dependent rotamer library for proteins derived from adaptive kernel density estimates and regressions. *Structure*, 19(6):844–858, June 2011.

[75] M A Keniry, A Kintanar, R L Smith, H S Gutowsky, and E Oldfield. Nuclear magnetic resonance studies of amino acids and proteins. deuterium nuclear magnetic resonance relaxation of deuteriomethyl-labeled amino acids in crystals and in halobacterium halobium and escherichia coli cell membranes. *Biochemistry*, 23(2):288–298, Jan 1984.

[76] D. Flemming Hansen, Philipp Neudecker, Pramodh Vallurupalli, Frans A. A. Mulder, and Lewis E. Kay. Determination of Leu Side-Chain Conformations in Excited Protein States by NMR Relaxation Dispersion. *Journal of the American Chemical Society*, 132(1):42–43, 2010. PMID: 20000605.

[77] D. Flemming Hansen, Philipp Neudecker, and Lewis E. Kay. Determination of Isoleucine Side-Chain Conformations in Ground and Excited States of Proteins from Chemical Shifts. *Journal of the American Chemical Society*, 132(22):7589–7591, 2010. PMID: 20465253.

[78] Carolin C Lechner and Christian F W Becker. Modified silaffin R5 peptides enable encapsulation and release of cargo molecules from biomimetic silica particles. *Bioorg Med Chem*, 21(12):3533–3541, Jun 2013.

[79] Céline Auger, Anne Lesage, Stefano Caldarelli, Paul Hodgkinson, and Lyndon Emsley. Deuterium-Carbon NMR Correlation Spectroscopy in Oriented Materials. *Journal of the American Chemical Society*, 119(49):12000–12001, Dec 1997.

[80] Xiangyan Shi, Jeffery L Yarger, and Gregory P Holland. Elucidating proline dynamics in spider dragline silk fibre using ^{2}H-^{13}C HETCOR MAS NMR. *Chemical communications (Cambridge, England)*, pages 13–16, 2014.

[81] Xiangyan Shi, Gregory P. Holland, and Jeffery L. Yarger. Molecular Dynamics of Spider Dragline Silk Fiber Investigated by ^{2}H MAS NMR. *Biomacromolecules*, 16(3):852–859, 2015.

[82] Xiangyan Shi, Jeffery L. Yarger, and Gregory P. Holland. ^{2}H–^{13}C HETCOR MAS NMR for indirect detection of ^{2}H quadrupole patterns and spin–lattice relaxation rates. *Journal of Magnetic Resonance*, 226:1–12, Jan 2013.

[83] K. Torii and Y. Iitaka. The crystal structure of L-isoleucine. *Acta Crystallographica Section B Structural Crystallography and Crystal Chemistry*, 27(11):2237–2246, 1971.

[84] A. Lesage, C. Auger, S. Caldarelli, and L. Emsley. Determination of through-bond carbon-carbon connectivities in solid-state NMR using the INADEQUATE experiment. *Journal of the American Chemical Society*, 119(33):7867–7868, 1997.

[85] Alexander D Scouras and Valerie Daggett. The dynameomics rotamer library: Amino acid side chain conformations and dynamics from comprehensive molecular dynamics simulations in water. *Protein Science : A Publication of the Protein Society*, 20(2):341–352, 02 2011.

[86] R. Dawkins. *The Blind Watchmaker*, page 1. Number 1986. W.W. Norton and Company, New York, USA, 1986.

[87] Moshe Gordon, Roy A. Black, Matthew C. Blosser, and Sarah L. Keller. Amino acids and peptides stabilize fatty acid membranes against salt-induced flocculation. *Biophysical Journal*, 108(2):542a, 2016/04/12.

[88] W R Hargreaves, S J Mulvihill, and D W Deamer. Synthesis of phospholipids and membranes in prebiotic conditions. *Nature*, 266(5597):78–80, Mar 1977.

[89] A D Bangham. Membrane models with phospholipids. *Prog Biophys Mol Biol*, 18:29–95, 1968.

[90] Pierre-Alain Monnard and David W. Deamer. Membrane self-assembly processes: Steps toward the first cellular life. *The Anatomical Record*, 268(3):196–207, 2002.

[91] Kenichi Morigaki, Peter Walde, Misni Misran, and Brian H Robinson. Thermodynamic and kinetic stability. Properties of micelles and vesicles formed by the decanoic acid/decanoate system. *Colloids and Surfaces A: Physicochemical and Engineering Aspects*, 213(1):37 – 44, 2003.

[92] Hiroshi Naraoka, Akira Shimoyama, and Kaoru Harada. Molecular Distribution of Monocarboxylic Acids in Asuka Carbonaceous Chondrites from Antarctica. *Origins of life and evolution of the biosphere*, 29(2):187–201, March 1999.

[93] Roy A. Black, Matthew C. Blosser, Benjamin L. Stottrup, Ravi Tavakley, David W. Deamer, and Sarah L. Keller. Nucleobases bind to and stabilize aggregates of a prebiotic amphiphile, providing a viable mechanism for the emergence of protocells. *Proceedings of the National Academy of Sciences*, 110(33):13272–13276, 2013.

[94] Dick Sandström, Mei Hong, and Klaus Schmidt-Rohr. Identification and mobility of deuterated residues in peptides and proteins by ^{2}H-^{1}3C solid-state NMR. *Chemical Physics Letters*, 300(1-2):213–220, Jan 1999.

[95] Terry Gullion, Raghuvansh Kishore, and Tetsuo Asakura. Determining Dihedral Angles and Local Structure in Silk Peptide by ^{13}C - ^{2}H REDOR. *Journal of the American Chemical Society*, 125(25):7510–7511, Jun 2003.

[96] Lihui Jia, Shuang Liang, Kelly Sackett, Li Xie, Ujjayini Ghosh, and David P. Weliky. REDOR solid-state NMR as a probe of the membrane locations of membrane-associated peptides and proteins. *Journal of Magnetic Resonance*, 253:154–165, Apr 2015.

[97] Li Xie, Ujjayini Ghosh, Scott D. Schmick, and David P. Weliky. Residue-specific membrane location of peptides and proteins using specifically and extensively deuterated lipids and ^{13}C–^{2}H rotational-echo double-resonance solid-state NMR. *Journal of Biomolecular NMR*, 55(1):11–17, Jan 2013.

[98] Suman A. Luthra, Marcel Utz, Eric M. Gorman, Michael J. Pikal, Eric J. Munson, and Joseph W. Lubach. Carbon–Deuterium Rotational-Echo Double-Resonance NMR Spectroscopy of Lyophilized Aspartame Formulations. *Journal of Pharmaceutical Sciences*, 101(1):283–290, January 2012.

[99] Thomas Bräuniger, Philip Wormald, and Paul Hodgkinson. *Improved Proton Decoupling in NMR Spectroscopy of Crystalline Solids Using the Spinal-64 Sequence*, pages 69–74. Springer Vienna, Vienna, 2003.

[100] P.S. Belton, A.M. Gil, and S.F. Tanner. On the ^{13}C spectra of leucine. *Solid State Nuclear Magnetic Resonance*, 1(2):67–71, Jun 1992.

[101] Eleri Hughes, Jonathan C. Clayton, and David a. Middleton. Probing the Oligomeric State of Phospholamban Variants in Phospholipid Bilayers from Solid-State NMR Measurements of Rotational Diffusion Rates. *Biochemistry*, 44(10):4055–4066, Mar 2005.

[102] Byungsu Kwon, Alan J. Waring, and Mei Hong. A ^{2}H Solid-State NMR Study of Lipid Clustering by Cationic Antimicrobial and Cell-Penetrating Peptides in Model Bacterial Membranes. *Biophysical Journal*, 105(10):2333–2342, Nov 2013.

[103] Judith A. Barry and Klaus Gawrisch. Direct NMR Evidence for Ethanol Binding to the Lipid-Water Interface of Phospholipid Bilayers. *Biochemistry*, 33(26):8082–8088, Jul 1994.

[104] J.H. Davis, K.R. Jeffrey, M. Bloom, M.I. Valic, and T.P. Higgs. Quadrupolar echo deuteron magnetic resonance spectroscopy in ordered hydrocarbon chains. *Chemical Physics Letters*, 42(2):390 – 394, 1976.

[105] M Lafleur, B Fine, E Sternin, P R Cullis, and M Bloom. Smoothed orientational order profile of lipid bilayers by ^{2}H-nuclear magnetic resonance. *Biophysical Journal*, 56(5):1037–1041, 11 1989.

[106] Liliya Vugmeyster, Dmitry Ostrovsky, Toni Villafranca, Janelle Sharp, Wei Xu, Andrew S Lipton, Gina L Hoatson, and Robert L Vold. Dynamics of Hydrophobic Core Phenylalanine Residues Probed by Solid-State Deuteron NMR. *J Phys Chem B*, 119(47):14892–14904, Nov 2015.

[107] S L Miller and H C Urey. Organic compound synthesis on the primitive earth. *Science*, 130(3370):245–251, Jul 1959.

[108] Naomi H.M. Hogg, Paul J.T. Boulton, Vadim E. Zorin, Robin K. Harris, and Paul Hodgkinson. Use of rotary echoes in magic-angle spinning NMR for the quantitative study of molecular dynamics. *Chemical Physics Letters*, 475(1-3):58–63, Jun 2009.

[109] Asher Schmidt and Shimon Vega. NMR line shape analysis for two-site exchange in rotating solids. *The Journal of Chemical Physics*, 87(12):6895, 1987.

Appendix A

WHERE TO FIND THE FILES

A.1 Setup

If you have minimal coding experience or are moving to Python from MATLAB, the easiest way to install and get start is to download a program like Spyder, available here: `https://github.com/spyder-ide/spyder`. Spyder is the Scientific PYthon Development EnviRonment, and it can be a good way to get started. I ultimately prefer to install Python separately, I feel that it runs more smoothly. If you're interested in that, continue reading.

A.1.1 Installing Python on a Mac

- Install XCode from `https://developer.apple.com/xcode/`
- In the Terminal, run the following line:

```
$ xcode -select --install
```

- install Homebrew using:

```
1 /usr/bin/ruby -e "$(curl -fsSL https://raw.githubusercontent.com/Homebrew/install/
    master/install)"

  brew install python3
  pip3 install ipython
  pip3 install numpy
  pip3 install scipy
  pip3 install nose
  pip3 install matplotlib
```

A.1.2 Package, (version used)

- Python (3.4.3)
- iPython (4.1.2)
- numpy (1.11.0)
- scipy (0.17.0)
- nose (1.3.7)
- matplotlib (1.5.1)

To edit files, you can use any text editor. I prefer to use TextWrangler. It is free through the App Store, and will do syntax highlighting, that is, it will change the color of key words in the coding language you are using, as well as change colors of comments to distinguish them from the code itself.

A.1.3 First Steps

You should now have a working version of Python installed! If you downloaded Spyder, launch the interface and go to town!

If you want to mess around with the basics of python in the Terminal, you can launch a session by typing:

```
$ ipython
```

If you want to run a script you have written (see next section for examples), navigate to that file in the Terminal. (Using the `cd` command to change directories) For example, if your script is called `file.py` in `Folder`:

```
$ cd Folder
$ ipython file.py
```

If ssh-ing into a Linux system, jobs can be submitted as above. To avoid stopping jobs upon logout, jobs can be submitted as follows:

```
$ nohup ipython file.py &
$ exit
```

Any printed text output will be stored in a file called `nohup.out`.

A.2 Basic Input Files

A.2.1 Quadrupolar Echo Input

`Dropbox\HEFCode\paramQE.py`

```
"""
import modules, functions from other files
"""
import numpy as np              #python package for arrays
import matplotlib.pyplot as plt #for plotting data
from oneSiteMatrix import chi2euler, chi2eulerMethyl        #only needed in special cases
from simQE import runSim as run #import runSim method from the appropriate simulator

"""
paramfileQE
2 site jump with Explicit Methyl Rotation, 6k tiles
"""

"""
Basic Parameters
"""
param={}                        #Initialize a dictionary for holding relevant parameters
param['dwell']=.8                #dwell time in micro seconds (10^-6)
param['taudelay']=40.           #delay between pi pulses in microseconds
param['ntiles']=6000            #number of tiles used to integrate powder pattern
param['nfidpts']=512*2            #number of FID points to calculate

"""
Set of special flags for handling of special cases
"""
param['chionly?']=False
param['all_contributions'] = True
param['chimethyl?']=False
```

```
param['chi?']= True

"""
Site definitions
"""
"""
param['cq']: QCC in kHz
param['anglemats']: Orientation frames in the form: [[frame1],[frame2],...], with [frame] = [[angle1],[angle2],...]. angles are Euler angles as described in Chapter 2, in degrees. Note that for a single site you still need all the brackets, [[frame]]=[[[angle]]]
param['ratemats']: Site connectivity and rates for each frame, in the form [[k1,Connectivity],...]. Preset connectivities are described in Appendix B, see oneRateMatrix
param['sitepops']: Populations for each site, note that if you have a repeating list you can do as follows: [1.,]*6
"""
state = [10.8, 8.3, 411958.0398583684, 48.8, 156.3, 66.37173042089874, 4.0, 2.778452529613264, 15.0, 2.7584315260835806, 8.80509919854084e-07]

param['cq_delta']=state[3]
param['cq_gamma']=state[4]
param['%gamma']=.15
param['eta']=0.
param['chiangles'] = [[-68.9, -88.9, -96.3, -161.2, -166.5, -178.8],[172.7, -61.1, 40.9, 171.9, -76.9, 60.6]]

param['anglemats']=[chi2euler(param['chiangles'],param['all_contributions'])]
param['ratemats']=[[(state[0], state[1], state[2]), 'Chi6']]

param['sitepops']=[state[5],state[7],state[8],state[9],state[10],state[6]]

"""
Parameters for processing the FID before FT
"""
param['llb']=1          #Lorentzian line broadening in kHz
param['glb']=0          #Gaussian line broadening in kHz
param['zerofill']=5     #zero filling: total number of spectral points = nFID*2**zf

param = run(param)      #runs the simulation, for details see Appendix B

"""
Manipulation of data, for example plotting the spectrum
"""
```

```
freq_axis = param['freq_axis']
gSpec, mSpec = param['specg'].real, param['specm'].real

plt.xlim(-60,60)
plt.plot(freq_axis,gSpec-np.amin(gSpec))
plt.plot(freq_axis,mSpec-np.amin(mSpec))
plt.show()

plt.xlim(-60,60)
plt.plot(freq_axis,gSpec+mSpec-np.amin(gSpec+mSpec))
plt.show()
```

Dropbox\HEFCode\paramQE.py

```
"""
import modules, functions from other files
"""
import numpy as np              #python package for arrays
import matplotlib.pyplot as plt #for plotting data
from oneSiteMatrix import chi2euler, chi2eulerMethyl        #only needed in special cases
from simQE import runSim as run #import runSim method from the appropriate simulator

"""
paramfileQE
2 site jump with Explicit Methyl Rotation, 6k tiles
"""

"""
Basic Parameters
"""
param={}                        #Initialize a dictionary for holding relevant parameters
param['dwell']=.8                #dwell time in micro seconds (10^-6)
param['taudelay']=40.           #delay between pi pulses in microseconds
param['ntiles']=6000            #number of tiles used to integrate powder pattern
param['nfidpts']=512*2            #number of FID points to calculate

"""
Set of special flags for handling of special cases
"""
param['chionly?']=False
param['all_contributions'] = True
param['chimethyl?']=False
param['chi?']= True
```

```
30
31 """
32 Site definitions
33 """
34 """
35 param['cq']: QCC in kHz
36 param['anglemats']: Orientation frames in the form: [[frame1],[frame2],...], with [frame] =
       [[angle1],[angle2],...]. angles are Euler angles as described in Chapter 2, in degrees.
        Note that for a single site you still need all the brackets, [[frame]]=[[[angle]]]
37 param['ratemats']: Site connectivity and rates for each frame, in the form [[k1,Connectivity
       ],...].  Preset connectivities are described in Appendix B, see oneRateMatrix
38 param['sitepops']: Populations for each site, note that if you have a repeating list you can
        do as follows: [1.,]*6
39 """
40 state = [10.8, 8.3, 411958.0398583684, 48.8, 156.3, 66.37173042089874, 4.0,
       2.778452529613264, 15.0, 2.7584315260835806, 8.80509919854084e-07]
41
42 param['cq_delta']=state[3]
43 param['cq_gamma']=state[4]
44 param['%gamma']=.15
45 param['eta']=0.
46 param['chiangles'] = [[-68.9, -88.9, -96.3, -161.2, -166.5, -178.8],[172.7, -61.1, 40.9,
       171.9, -76.9, 60.6]]
47
48 param['anglemats']=[chi2euler(param['chiangles'],param['all_contributions'])]
49 param['ratemats']=[[(state[0], state[1], state[2]), 'Chi6']]
50
51 param['sitepops']=[state[5],state[7],state[8],state[9],state[10],state[6]]
52
53 """
54 Parameters for processing the FID before FT
55 """
56 param['llb']=1          #Lorentzian line broadening in kHz
57 param['glb']=0          #Gaussian line broadening in kHz
58 param['zerofill']=5     #zero filling: total number of spectral points = nFID*2**zf
59
60 param = run(param)      #runs the simulation, for details see Appendix B
61
62 """
63 Manipulation of data, for example plotting the spectrum
64 """
65 freq_axis = param['freq_axis']
```

```
gSpec, mSpec = param['specg'].real, param['specm'].real

plt.xlim(-60,60)
plt.plot(freq_axis,gSpec-np.amin(gSpec))
plt.plot(freq_axis,mSpec-np.amin(mSpec))
plt.show()

plt.xlim(-60,60)
plt.plot(freq_axis,gSpec+mSpec-np.amin(gSpec+mSpec))
plt.show()
```

A.2.2 Magic Angle Spinning Input

Dropbox\HEFCode\paramMAS.py

```
import numpy as np
import matplotlib.pyplot as plt     #for plotting data
from simMAS import runSim as run    #import runSim method from the appropriate simulator

"""
paramfileMAS
3x6 site jump with 6000 tiles
"""

"""
Basic Parameters
"""
param={}        #Initialize a dictionary for holding relevant parameters
param['ntiles']=6000  #number of tiles used to integrate powder pattern
param['nfidpts']=512  #number of FID points to calculate

"""
MAS Specific Parameters
"""
param['spinrate']=4000      #spinning speed in Hz
param['rotfrac']=64       #number of points calculated per rotor period
#param['leftshift']=0   #note, this is now zero because not a QE
param['dwell']=1/(param['spinrate']*param['rotfrac'])   #dwell is calculated from above

"""
Set of special flags for handling of special cases
"""
```

```
param['chionly?']=False
param['chimethyl?']=False
param['chi?']= False

"""
Site definitions
"""
param['cq']=152.
d=5       #using variables to slightly offset angles
e=1.4
param['anglemats']=[[[0,68,0],[0,68,120],[0,68,240]],[[0,90,0],[0,90-d,60+e],[0,90-d,120-e],[0,90,180],[0,90+d,240+e],[0,90+d,300-e]]]
param['ratemats']=[[5*10**10,'All'],[1.5*10**8,'Circle']]
param['sitepops']=[1.,]*18

"""
Parameters for processing the FID before FT
"""
param['llb']=0      #Lorentzian line broadening in kHz
param['glb']=0      #Gaussian line broadening in kHz
param['zerofill']=1   #zero filling: total number of spectral points = nFID*2**zf

param = run(param)      #returns param['FID'], param['spec'], param['freq_axis']

"""
Manipulation of data, for example plotting the spectrum
"""
plt.xlim(-80,80)
plt.plot(param['freq_axis'],param['spec']/np.amax(param['spec'].real))
plt.show()      #plt.savefig('mastest.png', dpi = 300, bbox_inches='tight')  #swap to have it saved instead
```

A.2.3 T1IR Input

Dropbox\HEFCode\paramT1.py

```
import numpy as np
from simT1IR import runSim as run   #import runSim method from the appropriate simulator
import matplotlib.pyplot as plt     #for plotting data
from scipy.optimize import minimize, curve_fit   #for fitting t1

"""
```

```
7  paramfileT1
8  2 site jump with Explicit Methyl Rotation, 2k tiles
9  """
10
11 """
12 Basic Parameters
13 """
14 param={}                          #Initialize a dictionary for holding relevant parameters
15 param['dwell']=2.                 #dwell time in micro seconds (10^-6)
16 param['taudelay']=30.             #delay between pi pulses in microseconds
17 param['ntiles']=6000              #number of tiles used to integrate powder pattern
18 param['nfidpts']=256              #number of FID points to calculate
19
20 """
21 Relaxation Specific Parameters
22 """
23 param['w0']=76.753      #this is the strength of the 500MHz
24 param['taulist']=[.001,.01,.02,.03,.05,.1,.2,.4]   #in seconds
25
26 """
27 Set of special flags for handling of special cases
28 """
29 param['chionly?']=False
30 param['chimethyl?']=False
31 param['chi?']= False
32
33 """
34 Site definitions
35 """
36 param['cq']=160.
37 param['anglemats']=[[[0,71,0],[0,71,120],[0,71,240]],[[0,53,0],[0,53,180]]]
38 param['ratemats']=[[5*10**9,'Circle'],[2000,'All']]
39 param['sitepops']=[1.,]*6
40
41 """
42 Parameters for processing the FID before FT
43 """
44 param['llb']=0          #Lorentzian line broadening in kHz
45 param['glb']=0          #Gaussian line broadening in kHz
46 param['zerofill']=5     #zero filling: total number of spectral points = nFID*2**zf
47
48 param = run(param)
```

```
49
50 """
51 Manipulation of data, for example plotting the spectrum
52 """
53 freq_axis = param['freq_axis']
54 Spec = param['spec']
55 taus = param['taulist']
56 ntau = len(taus)
57
58 """plotting the series of partially relaxed spectra"""
59 for fid in range(ntau):
60     plt.plot(freq_axis,Spec[fid])
61 plt.xlim(-100,100)
62 plt.show()#plt.savefig('t1_benchmarking.png', dpi = 300, bbox_inches='tight')
63
64 """t1 anisotropy"""
65 rangekHz = 30  # range of spectrum to fit
66
67 deltafreq=freq_axis[45]-freq_axis[44]
68 maxpt = int(rangekHz//deltafreq)
69 center = int(param['zfpts']//2)
70
71 """some points - especially good for experimental data which is noisy"""
72 #numb = 109     #number of points to fit on range
73 #pts = np.fix(np.linspace(-maxpt,maxpt,num=numb)).astype(int)+center
74
75 """to include all the points"""
76 numb = maxpt*2+1
77 pts = np.fix(np.linspace(-maxpt,maxpt,num=numb)).astype(int)+center
78
79 t1 = np.zeros(numb)
80 t1e = np.zeros(numb)
81
82 def func(x,a,b,c):
83     return a - 2*b*np.exp(-np.array(x)/c)
84
85 for ii,jj in enumerate(pts):
86     popt, pcov = curve_fit(func,taus,Spec[:,jj],p0=(Spec[0,jj],Spec[0,jj],.05))
87     t1[ii] = popt[2]
88     t1e[ii] = np.sqrt(np.diag(pcov))[2]
89
90 """plotting example of how to overlay plots with two different y axes"""
```

```
fig, ax1 = plt.subplots()
for fid in range(ntau):
    ax1.plot(freq_axis,Spec[fid])
    ax1.set_ylabel('int', color='b')
    ax1.set_xlim(-100,100)
    for tl in ax1.get_yticklabels():
        tl.set_color('b')
ax2 = ax1.twinx()
#ax2.plot(freq_axis[pts.astype(int)],t1, 'r.-')   #looks better for some points only
ax2.plot(freq_axis[pts.astype(int)],t1, 'r')
ax2.set_ylabel('T1Z', color='r')
ax2.set_xlim(-80,80)

"""example of import of "pickled" data"""
"""ax2.set_ylim(.035,.055)
for tl in ax2.get_yticklabels():
    tl.set_color('r')

t1data = pickle.load( open("t1data.p", "rb" ) )
site = 'L5'
key = 'd7'+site
t1exp = t1data[key + "anisotropy"]
t1expe =  t1data[key + "error"]
xexp = t1data['xa']
ax2.plot(xexp,t1exp, 'b.-')
ax2.fill_between(xexp, t1exp-t1expe, t1exp+t1expe, alpha=.15, edgecolor='k', facecolor='k',
    linewidth=0)"""
plt.show()#plt.savefig('t1_'+'test2.png', dpi = 300, bbox_inches='tight')
```

Appendix B

CODE

B.1 Simulators

B.1.1 Quadrupolar Echo

Dropbox\HEFCode\simQE.py

```
import numpy as np
import math
import time
from scipy.linalg import expm
from oneRateMatrix import defineRateMatrix
from zcwtiling import tiles as zcw
from wignerangles import wigner
from oneSiteMatrix import defineSiteAngles

"""
simQE
"""

def expm2(A):
    r = np.zeros_like(A)
    for ii in range(A.shape[0]):
        r[ii] = expm(A[ii])
    return r

def adjustParam(param):
    param['nframes'],param['nsites'],param['oneanglematrix']=defineSiteAngles(param)
    if param['chi?']:
        cq=np.full(param['nsites']*2,param['cq_delta'])
        cq = np.concatenate((cq,np.full(param['nsites'],param['cq_gamma'])))

        deut = 2*param['%gamma']/(1-param['%gamma'])
        pops = [x for x in param['sitepops']]
        popd = [x*deut for x in pops]
```

```
29          pops += pops + popd
30      elif type(param['cq']) is 'list' and len(param['cq']) == param['nsites']:
31          cq=param['cq']
32          pops=param['sitepops']
33      else:
34          cq=np.full(param['nsites'],param['cq'])
35          pops=param['sitepops']
36
37
38      param['cq_sim']=cq*2*math.pi*1000*3/4
39
40      poptotal = sum(pops)
41      if poptotal!=1:
42          pops=[x/poptotal for x in pops]
43      param['pop_sim']=pops
44      param['oneratematrix']=defineRateMatrix(param)
45      return param
46
47  def sim(param):
48      if len(param['pop_sim']) == 1:
49          dwell = param['dwell']*10**-6
50          delay = param['taudelay']*10**-6
51          npts = param['nfidpts']
52          cq = param['cq_sim']
53
54          FID=np.zeros((npts,),dtype=np.cfloat)
55          tiles,ntiles = param['tiles'],param['ntiles']
56          anglemat = param['oneanglematrix']
57
58          weights = tiles[:,3]
59
60          freq = np.asarray(wigner(anglemat,tiles[:,0:3])).reshape(ntiles)*cq
61          propA=1j*freq.real
62
63          zero=np.exp(-1j*freq*delay)
64          dwelt=np.exp(1j*freq*dwell)
65          FID[0]=zero.dot(weights)
66          for tt in range(1,npts-1):
67              zero = dwelt*zero
68              FID[tt]=zero.dot(weights)
69          return FID.real
70
```

```
71      dwell = param['dwell']*10**-6
72      delay = param['taudelay']*10**-6
73      npts = param['nfidpts']
74      cq = param['cq_sim']
75      kmat = param['oneratematrix']
76
77      pops = param['pop_sim']
78      m0 = np.asarray(pops)**0.5
79      nsites = len(pops)
80
81      FID=np.zeros((npts,),dtype=np.cfloat)
82      tiles,ntiles = param['tiles'],param['ntiles']
83      anglemat = param['oneanglematrix']
84      weights = tiles[:,3]
85
86      freq = np.asarray(wigner(anglemat,tiles[:,0:3])).reshape(ntiles,nsites)
87      freqmat = np.array([np.diag(x*cq) for x in freq])
88      propA=1j*freqmat+kmat
89
90      if not (param['chi?'] and param['all_contributions']):
91          zero=expm2(np.conj(propA)*delay).dot(m0)
92          dwelt=expm2(propA*dwell)
93          for tt in range(npts-1):
94              FID[tt]=zero.dot(m0).dot(weights)
95              zero = np.squeeze(np.matmul(dwelt,zero[...,None])) #np.einsum('ijk,ik->ij',dwelt
    ,zero)
96      else:
97          nrotamers=int(nsites/3)
98          FIDm=np.zeros((npts,),dtype=np.cfloat)
99          FIDg=np.zeros((npts,),dtype=np.cfloat)
100         for ll in range(3):
101             if ll is 2:
102                 FID = FIDg
103             else:
104                 FID = FIDm
105             st=ll*nrotamers
106             en=(ll+1)*nrotamers
107             zero=expm2(np.conj(propA[:,st:en,st:en])*delay).dot(m0[st:en])
108             dwelt=expm2(propA[:,st:en,st:en]*dwell)
109             for tt in range(1,npts-1):
110                 FID[tt]+=zero.dot(m0[st:en]).dot(weights)
111                 zero = np.einsum('ijk,ik->ij',dwelt,zero)
```

```
112         return FIDm.real, FIDg.real
113     return FID.real
114 
115 def runSim(param):
116     #param={'nfidpts','ntiles','dwell','taudelay'}
117     param['tiles'], param['ntiles']=zcw(param['ntiles'])
118 
119     param = adjustParam(param)
120     if not (param['chi?'] and param['all_contributions']):
121         start = time.perf_counter()
122         param['FID'] = FID = sim(param)
123         print(time.perf_counter()-start)
124 
125         tt = param['dwell']*10**-6*np.arange(param['nfidpts'])
126         ls = param['leftshift']=int(param['taudelay']/param['dwell'])
127         param['zfpts']=param['nfidpts']*2**param['zerofill'] #zero filling by multiples of
    2, ie pts*2^zf
128 
129         gb = math.copysign(((math.pi*1000*param['glb']/(2))**2)/math.log(2),1000*param['glb'
    ])
130         lb=1000*param['llb']*math.pi
131         tt = param['dwell']*10**-6*np.arange(param['nfidpts'])
132         apod = np.exp(-lb*tt-gb*tt*tt)   #apodization function
133 
134         param['spec'] = Spec=np.fft.fftshift(np.fft.fft((FID*apod).real[ls:], n = param['
    zfpts']))
135         param['freq_axis'] = freq_axis=np.fft.fftshift(np.fft.fftfreq(param['zfpts'], d=
    param['dwell']*10**-3))
136     else:
137         start = time.perf_counter()
138         param['FIDm'],param['FIDg'] = FIDm, FIDg = sim(param)
139         print(time.perf_counter()-start)
140 
141         tt = param['dwell']*10**-6*np.arange(param['nfidpts'])
142         ls = param['leftshift']=int(param['taudelay']/param['dwell'])
143         param['zfpts']=param['nfidpts']*2**param['zerofill'] #zero filling by multiples of
    2, ie pts*2^zf
144 
145         gb = math.copysign(((math.pi*1000*param['glb']/(2))**2)/math.log(2),1000*param['glb'
    ])
146         lb=1000*param['llb']*math.pi
147         tt = param['dwell']*10**-6*np.arange(param['nfidpts'])
```

```
148         apod = np.exp(-lb*tt-gb*tt*tt)   #apodization function
149 
150         param['specm'] =np.fft.fftshift(np.fft.fft((FIDm*apod).real[ls:], n = param['zfpts'
    ]))
151         param['specg'] =np.fft.fftshift(np.fft.fft((FIDg*apod).real[ls:], n = param['zfpts'
    ]))
152         param['spec'] =param['specm']+param['specg']
153         param['freq_axis'] = freq_axis=np.fft.fftshift(np.fft.fftfreq(param['zfpts'], d=
    param['dwell']*10**-3))
154 
155     return param
```

B.1.2 Magic Angle Spinning

Dropbox\HEFCode\simMAS.py

```
1  import numpy as np
2  import math
3  import time
4  from scipy.linalg import expm
5  from oneRateMatrix import defineRateMatrix
6  from zcwtiling import tiles3 as zcw
7  from wignerangles import wignerFull as wigner, wignermas
8  from oneSiteMatrix import defineSiteAngles
9  """
10 simMAS
11 """
12 
13 def expm2(A):
14     r = np.zeros_like(A)
15     for ii in range(A.shape[0]):
16         r[ii] = expm(A[ii])
17     return r
18 
19 def adjustParam(param):
20     param['nframes'],param['nsites'],param['oneanglematrix']=defineSiteAngles(param)
21     if param['chi?']:
22         cq=np.full(param['nsites']*2,param['cq_delta'])
23         cq = np.concatenate((cq,np.full(param['nsites'],param['cq_gamma'])))
24 
25         deut = 2*param['%gamma']/(1-param['%gamma'])
26         pops = [x for x in param['sitepops']]
```

```
27          popd = [x*deut for x in pops]
28          pops += pops + popd
29
30      else:
31          cq=np.full(param['nsites'],param['cq'])
32          pops=param['sitepops']
33
34      param['cq_sim']=cq*1000*2*math.pi*3/4
35
36      poptotal = sum(pops)
37      if poptotal!=1:
38          pops=[x/poptotal for x in pops]
39      param['pop_sim']=pops
40      param['oneratematrix']=defineRateMatrix(param)
41      param['weights'] = param['tiles'][:,3]
42      return param
43
44  def sim(param):
45
46      tiles,ntiles = param['tiles'],param['ntiles'] #= zcw(param['ntiles'])
47      dwell = param['dwell']#*10**-6
48      npts = param['nfidpts']
49      cq = param['cq_sim']
50      pops = param['pop_sim']
51
52      npr = param['rotfrac']
53      nsites = len(pops)
54      m0 = np.asarray(pops)**0.5
55      m0.shape = (nsites,)
56      kmat = param['oneratematrix']
57      wts = param['weights']
58
59      site, spinning = wignermas(param['oneanglematrix'],param['rotfrac'])
60      if not (param['chi?'] and param['all_contributions']):
61          FID=np.zeros((npts,),dtype=np.cfloat)
62          for nn in range(0,ntiles):
63              mult = spinning.dot(wigner(tiles[nn,0:3])).dot(site.T)*cq
64              freqs = np.array([np.diag(x) for x in mult]).real
65              L = expm2((1j*freqs+kmat)*dwell)
66              Lt=np.zeros((npts+npr,nsites),dtype=np.cfloat)
67              temp = np.eye(nsites,dtype=np.cfloat)
68              for tt in np.arange(npr):
```

```
69                  Lt[tt]=temp.dot(m0)
70                  temp = L[tt].dot(temp)
71              factor = temp
72              for tt in range(int(math.log(npts,2)-math.log(npr,2))):
73                  Lt[2**tt*npr:2*2**tt*npr] = np.squeeze(np.matmul(factor,Lt[:2**tt*npr,:,None
    ]))
74                  factor = factor.dot(factor)
75              FID += Lt[:npts].dot(m0)*tiles[nn,3]
76      else:
77          FIDm=np.zeros((npts,),dtype=np.cfloat)
78          FIDd=np.zeros((npts,),dtype=np.cfloat)
79          nrotamers=int(nsites/3)
80          for nn in range(0,ntiles):
81              for ll in range(2):
82                  if ll == 1:
83                      FID = FIDd
84                      ll = 2
85                  else:
86                      FID = FIDm
87                  st=ll*nrotamers
88                  en=(ll+1)*nrotamers
89                  mult = site[st:en,:].dot(wigner(tiles[nn,0:3])).dot(spinning.T).T*cq[st:en]
90                  freqs = np.array([np.diag(x) for x in mult])
91                  R2 = 2*math.pi/(npts*dwell)
92                  L = expm2((1j*freqs+kmat- R2*np.eye(kmat.shape[0]))*dwell)
93                  Lt=np.zeros((npts+npr,nrotamers),dtype=np.cfloat)
94                  Lt[0] = np.eye(nrotamers,dtype=np.cfloat).dot(m0[st:en])
95                  for tt in index:
96                      Lt[tt]=L[tt-1].dot(Lt[tt-1])
97                  factor = Lt[npr]/Lt[0]
98                  for tt in range(npr+1,npts+npr):
99                      Lt[tt]=Lt[tt-npr]*factor
100                 FID += Lt[:npts].dot(m0[st:en])*tiles[nn,3]
101             return [x.real*2 for x in FIDm], [x.real for x in FIDd] #[x.real for x in FID],[
    x.imag for x in FID]
102     return FID #[x.real for x in FID],[x.imag for x in FID]
103
104
105 def runSim(param):
106     start = time.time()
107     param['tiles'], param['ntiles']=zcw(param['ntiles'])
108     param['dwell']=1/(param['spinrate']*param['rotfrac'])
```

```
109     param = adjustParam(param)
110     if not (param['chi?'] and param['all_contributions']):
111         param['FID'] = FID = sim(param)
112         print('time = ' + repr(time.time()-start))
113 
114         param['zfpts']=param['nfidpts']*2**param['zerofill'] #zero filling by multiples of
        2, ie pts*2^zf
115         FID = FID*np.exp(-param['llb']*math.pi*np.arange(FID.shape[0])*param['dwell'])
116         param['spec']=np.fft.fftshift(np.fft.fft((FID.real), n = param['zfpts']))
117         param['freq_axis']=np.fft.fftshift(np.fft.fftfreq(param['zfpts'], d=param['dwell'
        ]*10**3))
118     else:
119         param['FIDm'],param['FIDg'] = FIDm, FIDg = sim(param)
120         print('time = ' + repr(time.time()-start))
121         param['zfpts']=param['nfidpts']*2**param['zerofill'] #zero filling by multiples of
        2, ie pts*2^zf
122         FIDm = FIDm*np.exp(-param['llb']*math.pi*np.arange(FIDm.shape[0])*param['dwell'])
123         FIDg = FIDg*np.exp(-param['llb']*math.pi*np.arange(FIDg.shape[0])*param['dwell'])
124         param['specm'] =np.fft.fftshift(np.fft.fft(FIDm.real, n = param['zfpts']))
125         param['specg'] =np.fft.fftshift(np.fft.fft(FIDg.real, n = param['zfpts']))
126         param['spec'] =param['specm']+param['specg']
127         param['freq_axis']=np.fft.fftshift(np.fft.fftfreq(param['zfpts'], d=param['dwell'
        ]*10**3))
128     return param
```

B.1.3 T1 Inversion Recovery

Dropbox\HEFCode\simT1IR.py

```
1  import numpy as np
2  import math
3  import time
4  from scipy.linalg import expm
5  from scipy.sparse.linalg import eigsh
6  from oneRateMatrix import defineRateMatrix
7  from zcwtiling import tiles as zcw
8  from wignerangles import wigner, wignert1, tilesj
9  import pickle
10 from oneSiteMatrix import defineSiteAngles
11 """
12 simT1R
13 """
```

```
14
15 def expm2(A):
16     r = np.zeros_like(A)
17     for ii in range(A.shape[0]):
18         r[ii] = expm(A[ii])
19     return r
20
21 def adjustParam(param):
22     param['nframes'],param['nsites'],param['oneanglematrix']=defineSiteAngles(param)
23     if param['chimethyl?']:
24         cq=np.full(param['nsites']*7,param['cq_gamma'])
25         deut = 6*param['%gamma']/(1-param['%gamma'])
26         pops = np.repeat(np.array(param['sitepops']),3).tolist()
27         popd = (np.array(param['sitepops'])*deut).tolist()
28         pops += pops + popd
29     elif param['chi?']:
30         cq=np.full(param['nsites']*2,param['cq_delta'])
31         cq = np.concatenate((cq,np.full(param['nsites'],param['cq_gamma'])))
32         deut = 2*param['%gamma']/(1-param['%gamma'])
33         pops = [x for x in param['sitepops']]
34         popd = [x*deut for x in pops]
35         pops += pops + popd
36     else:
37         cq=np.full(param['nsites'],param['cq'])
38         pops=param['sitepops']
39
40     param['cq_sim']=cq*2*math.pi*1000*3/4
41
42     poptotal = sum(pops)
43     if poptotal!=1:
44         pops=[x/poptotal for x in pops]
45     param['pop_sim']=pops
46     param['oneratematrix']=defineRateMatrix(param)
47     return param
48
49 def getT1(cq, kmat, anglemat, w1, taus, m0, tiles, ntiles):
50     kval_all, vec_all = np.linalg.eigh(kmat)
51     sigvals = np.where(abs(kval_all)>10**-5)
52     kval = kval_all[sigvals]
53     vec = np.squeeze(vec_all[:,sigvals])
54
55     lam = -kval
```

```
56      rat1 = lam/(lam**2+w1**2)
57      rat2 = lam/(lam**2+4*w1**2)
58      PR2K = (wignert1(anglemat)*m0*cq*4/3*math.sqrt(3/8)).T
59      J1=np.zeros(ntiles,dtype=np.cfloat)
60      J2=np.zeros(ntiles,dtype=np.cfloat)
61      d4, d5 = tilesj(tiles)
62      tva = vec[:,None,:]*np.conj(PR2K[:,:,None])
63      tvap = vec[:,None,:]*PR2K[:,:,None]
64      temp = np.einsum('iav,jbv->abv', tva, tvap)
65      J1 =np.einsum('at,at->t',temp.dot(rat1).dot(d4),np.conj(d4)) #np.conj(d4[a,:])*d4[ap
        ,:]*(temp.dot(rat1))
66      J2 = np.einsum('at,at->t',temp.dot(rat2).dot(d5),np.conj(d5)) #np.conj(d5[a,:])*d5[ap
        ,:]*(temp.dot(rat2))
67      return (1-2*np.exp(-taus[:,None]*(J1+4*J2).real))
68
69  def sim(param):
70      dwell = param['dwell']*10**-6
71      delay = param['taudelay']*10**-6
72      npts = param['nfidpts']
73      cq = param['cq_sim']
74      kmat = param['oneratematrix']
75
76      pops = param['pop_sim']
77      w1 = 2*math.pi*10**6*param['w0']
78      taus=np.array(param['taulist'])
79      ntau=len(param['taulist'])
80      m0 = np.asarray(pops)**0.5
81
82      FID=np.zeros((ntau,npts),dtype=np.cfloat)
83      tiles,ntiles = param['tiles'],param['ntiles']
84      anglemat = param['oneanglematrix']
85
86      nsites = len(pops)
87      m0 = np.asarray(pops)**0.5
88      weights = tiles[:,3]
89
90      if not param['chimethyl?']:
91          tauw = getT1(cq, kmat, anglemat, w1, taus, m0, tiles, ntiles)
92          freq = np.asarray(wigner(anglemat,tiles[:,0:3])).reshape(ntiles,nsites)
93          freqmat = np.array([np.diag(x*cq) for x in freq])
94          R2 = 2*math.pi/(npts*dwell)
95          propA = 1j*freqmat+kmat - R2*np.eye(kmat.shape[0])
```

```
96
97          dwelt=expm2(propA*dwell)
98          zero=expm2(np.conj(propA)*delay).dot(m0)
99          for tt in range(npts-1):
100             FID[:,tt]=(zero.dot(m0)*tauw).dot(weights)
101             zero = np.squeeze(np.matmul(dwelt,zero[...,None]))#np.einsum('ijk,ik->ij',dwelt,
    zero)
102         return FID.real
103     else:
104         for ii in range(3):
105             if ii == 0:
106                 st = 0
107                 en = 3*6
108                 nsites = 18
109             elif ii == 1:
110                 st = 3*6
111                 en = 6*6
112                 nsites = 18
113             else:
114                 st = 6*6
115                 en = 7*6
116                 nsites = 6
117
118             tauw = getT1(cq[st:en], kmat[st:en,st:en], anglemat[st:en], w1, taus, m0[st:en],
     tiles, ntiles)
119             freq = np.asarray(wigner(anglemat[st:en],tiles[:,0:3])).reshape(ntiles,nsites)
120             freqmat = np.array([np.diag(x*cq[st:en]) for x in freq])
121             R2 = 2*math.pi/(npts*dwell)
122             propA = 1j*freqmat+kmat[st:en,st:en] - R2*np.eye(kmat[st:en,st:en].shape[0])
123
124             dwelt=expm2(propA*dwell)
125             zero=expm2(np.conj(propA)*delay).dot(m0[st:en])
126             for tt in range(npts-1):
127                 FID[:,tt]+=(zero.dot(m0[st:en])*tauw).dot(weights)
128                 zero = np.squeeze(np.matmul(dwelt,zero[...,None]))#np.einsum('ijk,ik->ij',
    dwelt,zero)
129         return FID.real
130
131 def runSim(param):
132     param['tiles'], param['ntiles']=zcw(param['ntiles'])
133     param = adjustParam(param)
134     start = time.perf_counter()
```

```
135     param['FID'] = FID = sim(param)
136     print('time  ' + repr(time.perf_counter()-start))
137     xaxis=[n*param['dwell'] for n in range(0,param['nfidpts'])]
138 
139     param['leftshift']=int(param['taudelay']//param['dwell'])
140     param['specw']=1/param['dwell']*10**3
141     param['zfpts']=param['nfidpts']*2**param['zerofill'] #zero filling by multiples of 2, ie
         pts*2^zf
142     ls=param['leftshift']
143 
144     print('time  ' + repr(time.perf_counter()-start))
145     lb=1000*param['llb']*math.pi
146     apod = np.exp(-lb*param['dwell']*10**-6*np.arange(param['nfidpts']))     #apodization
        function
147 
148     taus=param['taulist']
149     ntau=len(taus)
150     param['spec'] = Spec = np.zeros((ntau,param['zfpts']))
151     param['freq_axis']=np.fft.fftshift(np.fft.fftfreq(param['zfpts'], d=param['dwell'
        ]*10**-3))
152     for fid in range(len(param['taulist'])):
153         param['spec'][fid] = Spec[fid]=np.fft.fftshift(np.fft.fft((FID[fid]*apod).real[ls:],
         n = param['zfpts']))
154     return param
```

B.2 Matrix Helper Routines

B.2.1 Rate Matrix

Dropbox\HEFCode\oneRateMatrix.py

```
1  import numpy as np
2  import math
3  """
4  oneRateMatrix
5  """
6 
7  def makeRateMatrix(rateinfo):
8      nsites=rateinfo[2]
9      if nsites==1:
10         return np.array([[0]])
11     elif nsites==2:
```

```
12          return np.array([[-1,1],[1,-1]])*rateinfo[0]
13      else:
14          if rateinfo[1]=='All':
15              k=rateinfo[0]
16              offdiag=np.ones((nsites,nsites))-np.eye(nsites)
17              return k*(offdiag-np.diag(offdiag.sum(1)))
18
19          elif rateinfo[1]=='Circle':
20              k=rateinfo[0]
21              offdiag=np.eye(nsites,k=1)+np.eye(nsites,k=-1)
22              offdiag[0,-1]=1
23              offdiag[-1,0]=1
24              return k*(offdiag-np.diag(offdiag.sum(1)))
25
26          elif rateinfo[1]=='Chain':
27              k=rateinfo[0]
28              offdiag=np.eye(nsites,k=1)+np.eye(nsites,k=-1)
29              return k*(offdiag-np.diag(offdiag.sum(1)))
30
31          elif rateinfo[1]=='Chi9':
32              k1,k2,k12=rateinfo[0]
33              nodiagonal=np.ones((3,3))-np.eye(3)
34              diag=nodiagonal*k2
35              offdiag=k1*np.eye(3)+k12*nodiagonal
36              alloffdiag=np.vstack((np.hstack((diag,offdiag,offdiag)),
37                          np.hstack((offdiag,diag,offdiag)),
38                          np.hstack((offdiag,offdiag,diag))))
39              return alloffdiag-np.diag(alloffdiag.sum(1))
40
41          elif rateinfo[1]=='Chi6':
42              k1,k2,k12=rateinfo[0]
43              nodiagonal=np.ones((3,3))-np.eye(3)
44              diag=nodiagonal*k2
45              offdiag=k1*np.eye(3)+k12*nodiagonal
46              alloffdiag=np.vstack((np.hstack((diag,offdiag)),
47                          np.hstack((offdiag,diag))))
48              return alloffdiag-np.diag(alloffdiag.sum(1))
49          elif rateinfo[1]=='Chi6Methyl':
50              k1,k2,k12,km=rateinfo[0]
51
52              offdiag=np.ones((3,3))-np.eye(3)
53              kmethyl = km*(offdiag-np.diag(offdiag.sum(1)))
```

```
54
55              nodiagonal=np.ones((3,3))-np.eye(3)
56              diag=nodiagonal*k2
57              offdiag=k1*np.eye(3)+k12*nodiagonal
58              alloffdiag=np.vstack((np.hstack((diag,offdiag)),
59                                    np.hstack((offdiag,diag))))
60              kchis = alloffdiag-np.diag(alloffdiag.sum(1))
61              kboth = mergeRates(kchis,kmethyl)
62              filler1=np.zeros_like(kboth)
63              filler2=np.zeros((kboth.shape[1],kchis.shape[1]))
64              return np.vstack(((np.hstack((kboth,filler1,filler2))),
65                       (np.hstack((filler1,kboth,filler2))),
66                       (np.hstack((filler2.T,filler2.T,kchis)))))
67          elif rateinfo[1]=='Pairs':
68              k=rateinfo[0]
69              diag=np.array([[-1,1],[1,-1]])
70              block = np.array([[-1,1],[1,-1]])
71              return k*diag
72          else:
73              print('invalid rate option')
74              return
75
76  def mergeRates(oldone,addrate):
77      sizek1=oldone.shape[1]
78      sizek2=addrate.shape[0]
79      newsize=sizek1*sizek2
80      newmat=np.zeros((newsize,newsize))
81      for ii in range(0,sizek2):
82          for jj in range(0,sizek2):
83              for kk in range(0,sizek1):
84                  newmat[kk*sizek2+ii,kk*sizek2+jj]=addrate[ii,jj]
85      for ii in range(0,sizek1):
86          for jj in range(0,sizek1):
87              for kk in range(0,sizek2):
88                  newmat[ii*sizek2+kk,jj*sizek2+kk]+=oldone[ii,jj]
89      return newmat
90
91  def defineRates(ratedata):
92      ratematrices = [makeRateMatrix(x) for x in ratedata]
93      onerate=ratematrices[0]
94      for n in range(1,len(ratematrices)):
95          onerate=mergeRates(onerate, ratematrices[n])
```

```
96      return onerate
97
98  def allContributions(onerate):
99      filler=np.zeros_like(onerate)
100     return np.vstack(((np.hstack((onerate,filler,filler))),
101                       (np.hstack((filler,onerate,filler))),
102                       (np.hstack((filler,filler,onerate)))))
103
104 def defineRateMatrix(param):
105     pops = param['pop_sim']
106     for nf in range(0,param['nframes']):
107         param['ratemats'][nf].append(len(param['anglemats'][nf]))
108     onerate=defineRates(param['ratemats'])
109     if param['chi?'] and not param['chimethyl?']:
110         if param['all_contributions']:
111             onerate=allContributions(onerate)
112     nsites=len(pops)
113     oneratematrix=np.zeros((nsites,nsites))
114     for x in range(0,nsites):
115         for y in range(0,nsites):
116             if y != x:
117                 oneratematrix[x,x]-=2*pops[y]*onerate[x,y]/(pops[x]+pops[y])
118                 oneratematrix[x,y]=2*onerate[x,y]*math.sqrt(pops[x]*pops[y])/(pops[x]+pops[y
    ])
119     return oneratematrix
```

B.2.2 Site Matrix

Dropbox\HEFCode\oneSiteMatrix.py

```
1  import math
2  import copy
3  import numpy as np
4  """
5  oneSiteMatrix
6  """
7
8  def defineSiteAngles(param):
9      anglemats=copy.deepcopy(param['anglemats'])
10     """Convert degree inputs into single frame, radian values"""
11     nframes=len(anglemats)
12     oneanglematrix=np.array([])
```

```
13      if nframes==1:
14          oneangle=anglemats[0]
15          deg=np.array(oneangle)
16          oneanglematrix=np.array([math.radians(z) for z in deg.flat]).reshape(np.shape(deg))
17          nsites=oneanglematrix.shape[0]
18          if param['chimethyl?']:
19              nsites *= 7**-1
20          elif param['chi?']:
21              nsites *= 3**-1
22          return nframes, nsites, oneanglematrix
23      elif nframes>1:
24          for nf in range(0,nframes):
25              nsites=len(anglemats[nf])
26              for ns in range(0,nsites):
27                  deg=anglemats[nf][ns]
28                  anglemats[nf][ns]=[math.radians(z) for z in deg]
29
30          tempframe=anglemats[0]
31          for nf in range(1,nframes):
32              addframe=anglemats[nf]
33              nsites2=len(addframe)
34              nsites1=len(tempframe)
35
36              for n1 in range(0,nsites1):
37                  nn=n1*nsites2
38                  site1=tempframe[nn]
39                  tempframe[nn]=mergeangle(site1,addframe[0])
40                  for n2 in range(1,nsites2):
41                      site2=addframe[n2]
42                      newsite=mergeangle(site1,site2)
43                      tempframe.insert(nn+n2,newsite)
44          oneanglematrix=np.array(tempframe)
45          nsites=oneanglematrix.shape[0]
46          if param['chimethyl?']:
47              nsites *= 7**-1
48          elif param['chi?']:
49              nsites *= 3**-1
50          return nframes, nsites, oneanglematrix
51
52  def mergeFrames(old,new):
53      nsites2=new.shape[0]
54      nsites1=old.shape[0]
```

```
55      merged=np.zeros((nsites1*nsites2,nsites1*nsites2))
56      for n1 in range(0,nsites1):
57          nn=n1*nsites2
58          merged[nn]=mergeangle(old[n1],new[0])
59          for n2 in range(1,nsites2):
60              merged[nn+n2]=mergeangle(old[n1],new[n2])
61      return merged
62
63  def angle2matrix(angle,axis):
64      """For a rotation by 'angle' (in radians) around an axis ('y' or 'z'), gives the matrix
        representation"""
65      cos=math.cos(angle)
66      sin=math.sin(angle)
67      if axis is 'z':
68          m = np.array([[cos,-sin,0],[sin,cos,0],[0,0,1]])
69      elif axis is 'y':
70          m = np.array([[cos,0,sin],[0,1,0],[-sin,0,cos]])
71      else:
72          print('This does not compute')
73          m = np.identity(3)
74      return m
75
76  def euler2matrix(angles):
77      """For a set of Euler angles, given by the Rose convention (z-y-z), generate an array
        with the composite rotation. """
78      alpha=angle2matrix(angles[0],'z')
79      beta=angle2matrix(angles[1],'y')
80      gamma=angle2matrix(angles[2],'z')
81
82      m=np.dot(alpha,np.dot(beta, gamma))
83      return m
84
85  def mergeangle(a1,a2):
86      """Given two sets of Euler angles, a1 and a2, describing sequential transformations (R1
        followed by R2, or R2*R1), return the equivalent single transformation."""
87      rot1=euler2matrix(a1)
88      rot2=euler2matrix(a2)
89      rot=np.dot(rot1,rot2)
90
91      cb=rot[2,2]
92      if (1-math.fabs(cb))<=0.00001: #if beta is ~0, it messes up the math. set gamma = 0,
        define alpha as single rotation around z axis
```

```
93          beta=0
94          gamma=0
95          alpha=math.atan2(-rot[0,1],rot[1,1])
96      else:
97          beta=math.acos(rot[2,2])
98          if beta<0:
99              beta+=math.pi*2
100
101         alpha=math.atan2(rot[1,2],rot[0,2])
102         if alpha<0:
103             alpha+=math.pi*2
104
105         gamma=math.atan2(rot[2,1],-rot[2,0])
106         if gamma<0:
107             gamma+=math.pi*2
108     euler=[alpha,beta,gamma]
109     return (euler)
110
111 def chi2euler(chi,allsites):
112     angle_m1 = []
113     angle_m2 = []
114     angle_d = []
115     for nn in range(0,len(chi[0])):
116         chi1=[math.radians(x) for x in [0, 70.5, -chi[0][nn]]]
117         chi2_m1=[math.radians(x) for x in [0, 70.5, -chi[1][nn]]]
118         chi2_m2=[math.radians(x) for x in [0, 70.5, -chi[1][nn]-120]]
119         chi2_d=[math.radians(x) for x in [0, 70.5, -chi[1][nn]+120]]
120         angle_m1.append([math.degrees(x) for x in mergeangle(chi2_m1,chi1)])
121         angle_m2.append([math.degrees(x) for x in mergeangle(chi2_m2,chi1)])
122         angle_d.append([math.degrees(x) for x in mergeangle(chi2_d,chi1)])
123     if allsites:
124         return angle_m1 + angle_m2 + angle_d
125     else:
126         return angle_m1
127
128 def chi2eulerMethyl(chi,allsites):
129     angle_m1 = []
130     angle_m2 = []
131     angle_d = []
132     md1 = [math.radians(x) for x in [0, 70.5, -60]]
133     md2 = [math.radians(x) for x in [0, 70.5, 60]]
134     md3 = [math.radians(x) for x in [0, 70.5, 180]]
```

```
135     for nn in range(0,len(chi[0])):
136         chi1=[math.radians(x) for x in [0, 70.5, -chi[0][nn]]]
137         chi2_m1=[math.radians(x) for x in [0, 70.5, -chi[1][nn]]]
138         chi2_m2=[math.radians(x) for x in [0, 70.5, -chi[1][nn]-120]]
139         chi2_d=[math.radians(x) for x in [0, 70.5, -chi[1][nn]+120]]
140         m1=mergeangle(chi2_m1,chi1)
141         m2=mergeangle(chi2_m2,chi1)
142 
143         angle_m1.append([math.degrees(x) for x in mergeangle(md1,m1)])
144         angle_m1.append([math.degrees(x) for x in mergeangle(md2,m1)])
145         angle_m1.append([math.degrees(x) for x in mergeangle(md3,m1)])
146         angle_m2.append([math.degrees(x) for x in mergeangle(md1,m2)])
147         angle_m2.append([math.degrees(x) for x in mergeangle(md2,m2)])
148         angle_m2.append([math.degrees(x) for x in mergeangle(md3,m2)])
149         angle_d.append([math.degrees(x) for x in mergeangle(chi2_d,chi1)])
150     if allsites:
151         return angle_m1 + angle_m2 + angle_d
152     else:
153         return angle_m1
```

B.2.3 Wigner Angles

Dropbox\HEFCode\wignerangles.py

```
1  import math
2  import numpy as np
3  """
4  wignerangles
5  #============================================================================
6  #   D = wigner(alpha,beta,gamma)
7  #   Calculates Wigner rotation matrix elements D2_mn
8  #
9  #   D  2  1  0 -1 -2
10 #   2  a  b  c  d  e
11 #   1 -b  f  g  h  d
12 #   0  c -g  k  g  c
13 #  -1 -d  h -g  f  b
14 #  -2  e -d  c -b  a
15 #============================================================================
16 """
17 
18 def wignerFull(angle):
```

```
19      """ Complete Wigner D matrix """
20      alpha = angle[0]
21      beta  = angle[1]
22      gamma = angle[2]
23
24      cb=math.cos(beta)
25      sb=math.sin(beta)
26
27      a=(1+cb)**2/4
28      b=-(1+cb)/2*sb
29      c=math.sqrt(6)/4*sb*sb
30      d=-(1-cb)/2*sb
31      e=(1-cb)**2/4
32      f=(1+cb)*(2*cb-1)/2
33      g=-math.sqrt(3/2)*sb*cb
34      h=(1-cb)*(2*cb+1)/2
35      k=(3/2*cb*cb-1/2)
36
37      temp=np.array([[a,b,c,d,e],[-b,f,g,h,d],[c,-g,k,g,c],[-d,h,-g,f,b],[e,-d,c,-b,a]])
38      D=np.empty((5,5),dtype=np.cfloat)
39
40      for m in range(-2,3):
41          D[2+m,:]=math.e**(1j*m*alpha)*temp[2+m,:]
42      for n in range(-2,3):
43          D[:,2+n]=D[:,2+n]*math.e**(1j*n*gamma)
44
45      return D
46
47  def wigner(sites,tiles):
48      """For every tile orientation, for every site, makes a list of the orientation-dependent
         frequencies \omega_i assuming \eta = 0, that is a symmetric quadrupolar moment"""
49      ntiles = tiles.shape[0]
50      nsites = sites.shape[0]
51
52      betaT = tiles[:,1]
53      cbT1 = np.cos(betaT)
54      sbT1 = np.sin(betaT)
55      alphaT = np.repeat(tiles[:,0],(nsites,)*ntiles)
56      cbT = np.repeat(cbT1,(nsites,)*ntiles)
57      sbT = np.repeat(sbT1,(nsites,)*ntiles)
58
59      betaS = sites[:,1]
```

```
60      cbS1 = np.cos(betaS)
61      sbS1 = np.sin(betaS)
62      gammaS = np.tile(sites[:,2],ntiles)
63      cbS = np.tile(cbS1,ntiles)
64      sbS = np.tile(sbS1,ntiles)
65
66      x = alphaT + gammaS
67      D = 3/4*sbS**2*sbT**2*np.cos(2*x)-3*sbS*cbS*sbT*cbT*np.cos(x)+(3/2*cbT**2-1/2)*(3/2*cbS
        **2-1/2)
68      return D
69
70  def wignermas(sitea,npr):
71      """ Wigner D values for sites and spinning steps """
72      betas = sitea[:,1]
73      gammas = sitea[:,2]
74      cs = math.sqrt(3/8)*np.sin(betas)**2
75      gs = -math.sqrt(3/2)*np.sin(betas)*np.cos(betas)
76      ks = 1/2*(3*np.cos(betas)**2-1)
77      site = np.array([cs,gs,ks,-gs,cs]).T*np.exp(1j*gammas[:,np.newaxis]*np.linspace(2, -2,
        5))
78
79      betam = math.acos(1/math.sqrt(3.))
80      cm = math.sqrt(6)/4*math.sin(betam)**2
81      gm = -math.sqrt(3/2)*math.sin(betam)*math.cos(betam)
82      km = 1/2*(3*math.cos(betam)**2-1)
83      alpham = np.linspace(0,2*math.pi,num=npr+1)#np.linspace(0,2*math.pi,num=npr+1)#np.append
        (np.linspace(0,math.pi,num=npr/2+1),np.linspace(math.pi,0,num=npr/2+1)[1:])#])linspace(
        math.pi,)2*math.pi/npr*(np.arange(0,npr+1))
84      #alpham += alpham[1]/2
85      spinning = np.exp(1j*alpham[:,np.newaxis]*np.linspace(2, -2, 5))*np.array([cm, -gm,km,
        gm,cm])
86      return site,spinning
87
88  def wignert1(sites):
89      """Wigner D values for site orientations needed to calculate the spectral densities, J
        """
90      betaS = sites[:,1]
91      cb = np.cos(betaS)
92      sb = np.sin(betaS)
93      g = sites[:,2]
94      n = np.linspace(-2,2,5)
95      nn = np.exp(1j*np.outer(g,n))
```

```
96      D = np.array([math.sqrt(6)/4*sb*sb,math.sqrt(3/2)*sb*cb,(3/2*cb*cb-1/2),-math.sqrt(3/2)*
        sb*cb,math.sqrt(6)/4*sb*sb]) * nn.T
97
98      sites[1,1] *= -1
99      sites[1,2] = 0
100     betaS = sites[:,1]
101     cb = np.cos(betaS)
102     sb = np.sin(betaS)
103
104     g = sites[:,2]
105     n = np.linspace(-2,2,5)
106     nn = np.exp(1j*np.outer(g,n))
107     D2 = np.array([math.sqrt(6)/4*sb*sb,math.sqrt(3/2)*sb*cb,(3/2*cb*cb-1/2),-math.sqrt(3/2)
        *sb*cb,math.sqrt(6)/4*sb*sb]) * nn.T
108     return D2
109
110 def tilesj(tiles):
111     """Wigner D values for the crystal orientations as required to calculated the spectral
        densities , J"""
112     alpha = tiles[:,0]
113     beta = tiles[:,1]
114     gamma = tiles[:,2]
115
116     n = np.arange(-2,3)
117     nn = np.exp(1j*np.outer(alpha,n))
118     ag4 = np.exp(1j*-1*gamma)*nn.T
119     ag5 = np.exp(1j*-2*gamma)*nn.T
120
121     cb=np.cos(beta)
122     sb=np.sin(beta)
123
124     a=(1+cb)**2/4
125     b=-(1+cb)/2*sb
126     c=math.sqrt(6)/4*sb*sb
127     d=-(1-cb)/2*sb
128     e=(1-cb)**2/4
129     f=(1+cb)*(2*cb-1)/2
130     g=-math.sqrt(3/2)*sb*cb
131     h=(1-cb)*(2*cb+1)/2
132     k=(3/2*cb*cb-1/2)
133
134     b4 = np.array([d,h,g,f,-b])
```

```
    b5 = np.array([e,d,c,b,a])
    d4=b4*ag4
    d5=b5*ag5
    return d4,d5
```

B.3 Tiling

Dropbox\HEFCode\zcwtiling.py

```
import math
import numpy as np
import pickle
"""
zcwtiling
number of tiles ---> tile matrix, actual number of tiles
"""

def ntiles(n):
    """returns fibonnacci number >= n"""
    a, b = 0, 1
    while a+b < n:
        a, b = b, a+b
    return a,a+b

def tiles(n):
    """ returns set of two site ZCW angles , and number of angles """
    m,n=ntiles(n)
    tilemat = np.zeros((n,4))
    tilemat[:,0] = np.fmod(np.arange(n,dtype=np.float)*m,n)*2*math.pi/n
    tilemat[:,1] = (np.arange(n,dtype=np.float)+1/2)*math.pi/n
    tilemat[:,3] = np.sin(tilemat[:,1])
    return tilemat, n

def tiles3(n):
    """returns set of three site ZCW angles, and number of angles, from pre-saved files"""
    tilesx = pickle.load( open("zcw3.p", "rb" ) )
    if n <= 200:
        n = 200
    elif n<= 300:
        n = 300
    elif n <= 538:
        n = 538
```

```
34      elif n<=1154:
35          n = 1154
36      elif n<= 3722:
37          n = 3722
38      elif n <= 6044:
39          n = 6044
40      return tilesx[n], n
```